Astronomy Reports, Vol. 49, No. 7, 2005, pp. 501–509. Translated from Astronomicheskiĭ Zhurnal, Vol. 82, No. 7, 2005, pp. 563–572.

The Stellar Structure of Irregular Galaxies. Face-on Galaxies

N. A. Tikhonov

Special Astrophysical Observatory, pos. Nizhniĭ Arkhyz, Russia

Received January 29, 2004; in final form, February 17, 2005

Abstract—Stellar photometry of nearby irregular galaxies of the Local Group is used to identify and study the young and old stellar populations of these galaxies. An analysis of the spatial distributions of stars of different ages in face-on galaxies shows that the young stellar populations in irregular galaxies are concentrated toward the center, and form local inhomogeneities in star-forming regions, while the old stellar populations—red giants—form extended structures around the irregular galaxies. The sizes of these structures exceed the visible sizes of the galaxies at the $25^m/\mathrm{arcsec}^2$ isophote by a factor of two to three. The surface density of the red giants decreases exponentially from the center toward the edge, similar to the disk components in spiral galaxies. © *2005 Pleiades Publishing, Inc.*

1. INTRODUCTION

Dwarf irregular galaxies are the most numerous of all observed galaxies. Their absolute luminosities lie in the interval from $M_B = -9^m$ to $M_B = -18^m$. Such galaxies usually have higher hydrogen contents than other types of dwarf galaxies, and are sometimes host to very intense star-forming processes. A very energetic burst of star formation may promote a galaxy to the class of blue compact dwarf galaxies. Many bright irregular galaxies exhibit signs of weak spiral arms, which are especially prominent in the distribution of neutral hydrogen, as is the case, e.g., in HoII [1] and IC 10 [2].

In this paper, we do not study normal spiral galaxies, which have higher masses and rotational velocities than irregular galaxies, although the dividing line between irregular and spiral galaxies is fairly arbitrary.

In his classification [3], Hubble introduced the class of irregular galaxies as a sort of a "wastebasket" for all the objects that could not be classed as spirals, ellipticals, or lenticulars. As is clear from their name, irregular galaxies have no regular shape. However, much observational data has been collected since the Hubble classification of galaxies was first adopted, and many of the initial views about the morphology and physical parameters of galaxies have evolved.

Hodge and Hitchcock [4] were the first to suggest, based on measurements of the apparent sizes of 131 galaxies, that irregulars may have flattened shapes. Some authors had expressed similar ideas before [3], but produced no corroborative observational evidence. Later, radio observations established that irregular galaxies rotate, thereby putting them together with spiral galaxies in the group of axisymmetric objects. However, the spatial stellar structure of irregular galaxies remained unclear, since their images exhibited chaotically scattered regions of bright young supergiants, while the old stellar populations were detectable only near the telescope limits in Local-Group galaxies.

A new era in the study of galaxies began in the 1980s with the advent of new detectors with high quantum efficiency—CCDs. Surface photometry has established that irregular galaxies show exponential radial brightness decreases [5, 6] similar to those observed for the disk components in spiral galaxies, suggesting a similarity between spiral and irregular galaxies.

Photoelectric color measurements of galaxies of various types show that irregular galaxies become redder toward their edges. This was easy to understand, since it was already known even at the time of Baade [7] that the peripheral regions of irregular galaxies in the Local Group are populated by a considerable number of red giants, which are visible on the Palomar plates. This suggested that other irregular galaxies might have a similar structure. The distribution of red giants in irregular galaxies is often described using the term "sheet," introduced by Baade, or "halo," used in modern papers. The use of different terms leads to confusion in descriptions of galaxy morphology. Whereas the term "sheet" means simply a stellar distribution with a low surface-density gradient, "halo" implies a spherical distribution of stars around the associated galaxies.

We believe that the use of the term "halo" for irregular galaxies is incorrect, because, as we show below, most irregular galaxies possess only an extended thick disk, which can be mistaken for a halo. Only massive galaxies have a genuine more extended halo in addition to the thick disk.

1063-7729/05/4907-0501$26.00

Face-on galaxies

No.	Name	RA/Dec (2000.0)	Type	Size, arcmin	Magnitude
1	K52	$08^h23^m56.0^s + 71°01'46''$	I ?	1.3×0.7	16.5
2	DD O53	08 34 07.2 +66 10 54	Im	1.5×1.3	14.5
3	K73	10 52 55.1 +69 32 47	Im	0.6×0.4	14.9
4	GR8	12 58 40.4 +14 13 03	ImV	1.1×1.0	14.7
5	HIPASS 1321-31	13 21 08.2 −31 31 45	Im	0.7×0.5	17.0
6	DEEP 1337-33	13 37 04.3 −33 21 51	Im	0.3×0.3	16.8
7	PGC 48111	13 37 20.0 −28 02 42	Im	1.3×1.0	15.0
8	HIPASS 1337-39	13 37 26.0 −39 53 47	Im	0.6×0.5	16.1
9	UGC 8833	13 54 48.7 +35 50 15	Im	0.9×0.8	16.5
10	DDO 187	14 15 56.5 +23 03 19	ImV	1.7×1.3	14.4
11	DDO 190	14 24 43.4 +44 31 33	IAm	1.8×1.8	13.2
12	UGCA 438	23 26 27.5 −32 23 20	IBm	1.5×1.2	13.9

Deep images have been taken for all galaxies in the Local Group and a few dozen other nearby galaxies. These show both bright, young supergiants and fainter red giants. The spatial distribution of stars of various types has been studied in several irregular galaxies [8–14].

The most detailed of these studies showed that:

(a) the distribution of red giants extends well beyond the $25^m/\text{arcsec}^2$ limit commonly used to define the galaxy sizes;

(b) in the few cases when the corresponding measurements were made, the density of red giants was found to decrease exponentially from the center of the galaxy towards the edge, similar to the disk components in spiral galaxies.

Minniti and Zijlstra [8, 12] interpreted the extended distributions of red giants in the galaxies WLM and NGC 3109 as evidence for halos, i.e., spheroidal distributions of stars. However, this conclusion is not justified, since they did not report the measured distribution of red giants along the major axis of the galaxy. Establishing the real spatial distribution of stars requires detailed studies of individual galaxies, and analyses of a representative sample of galaxies are needed to eliminate effects due to features associated with individual galaxies.

2. SELECTION OF OBJECTS AND OBSERVATIONS

Studies of the spatial structures of flat systems require observations of both edge-on and face-on galaxies of the same type. The shapes of edge-on galaxies in the Z direction can easily be determined, and the disk and halo, if any, identified. Moreover, in such galaxies the boundaries of the distributions of stars of various types are easier to determine, since they are projected onto a small area of sky.

Observations of face-on galaxies can be used to analyze the distribution of stars from the center to the periphery, which is not possible for edge-on galaxies. Thus, joint studies of galaxies viewed at different angles make it possible to study the spatial distributions of the constituent stars. Other criteria used to select our target objects included their rotational velocities ($V_r < 100$ km/s), morphological types (Irr, Irr/Sph), distances ($D < 5$ Mpc), and sizes. We used the rotational velocities as a check for their morphological types; i.e., irregular galaxies are known to have relatively low rotational velocities. We compiled a list of galaxies meeting our criteria and cross-identified it with the HST archive. Resolving galaxies beyond the Local Group into stars is difficult for ground-based telescopes, except for the brightest supergiants, whereas this is easy with the high spatial resolution of the HST.

In addition to the images adopted from the archive of the Hubble Space Telescope, we used images of the three irregular Local-Group galaxies IC 10, IC 1613, and Pegasus obtained by us in 1999 with the 6-m telescope of the Special Astrophysical Observatory (SAO). In addition, the galaxies DDO 187, DDO 190, DDO 210, and SagDIG were observed in 1997 with the 2.5-m Nordic Optical Telescope (NOT). Observations with the SAO 6-m telescope were made with a CCD with a $2.5' \times 2.5'$ field of

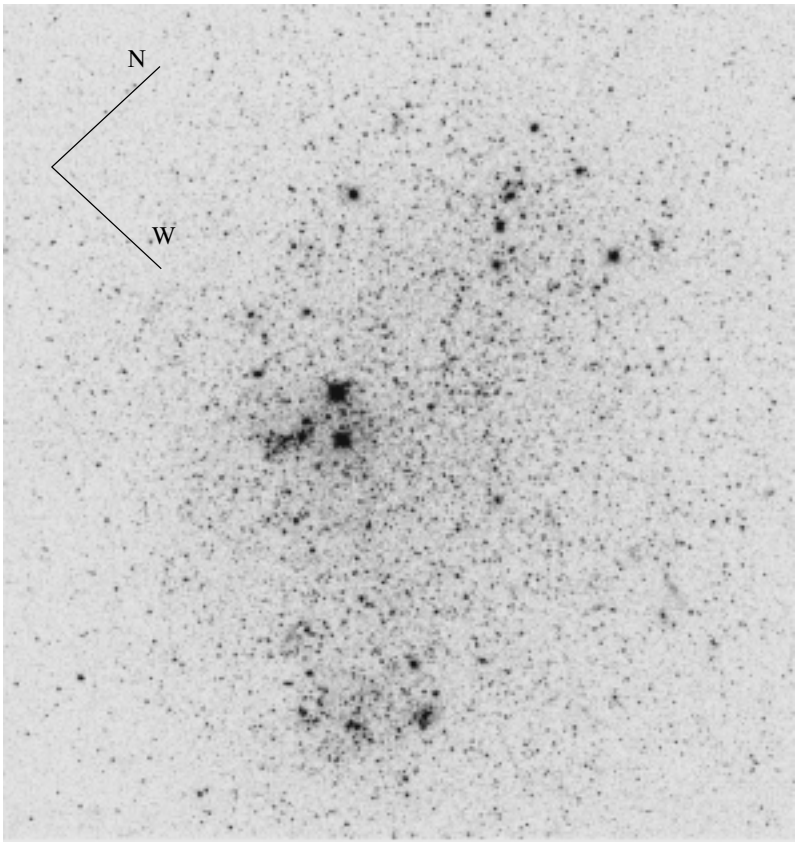

Fig. 1. Central part ($72'' \times 77''$) of GR8 as seen in the F550w and F814w HST images. The young, bright stars are concentrated in star-forming regions, whereas the fainter stars (mostly red giants) show a more extended and smoother structure.

view for the image scale of $0.137''$/pixel. Observations at the NOT were made with the HiRAC camera equipped with a Loral CCD producing a $3.75' \times 3.75'$ field of view for the image scale of $0.11''$/pixel. The HST field is $2.5'$ in size and has an image scale of $0.1''$/pixel. For many galaxies, these fields of view are too small to enable photometry of stars in the entire galaxy, but the required data about the stellar structure can be derived by selecting small galaxies or galaxies with efficiently chosen fields at appropriate locations along the major and minor axes. Our final list included 12 face-on and 12 edge-on galaxies. In addition to the irregular galaxies, we also studied about twenty galaxies of other types, however, those results lie beyond the scope of this paper.

Because of the large amount of observational data analyzed, we restrict our analysis here to the face-on galaxies. The table lists these galaxies and their main parameters, adopted from the NED database. The results for the two additional galaxies IC 10 and IC 1613 can be found in [15, 16].

3. STELLAR PHOTOMETRY

Prior to carrying out photometry of individual stars, we performed a standard preliminary reduction

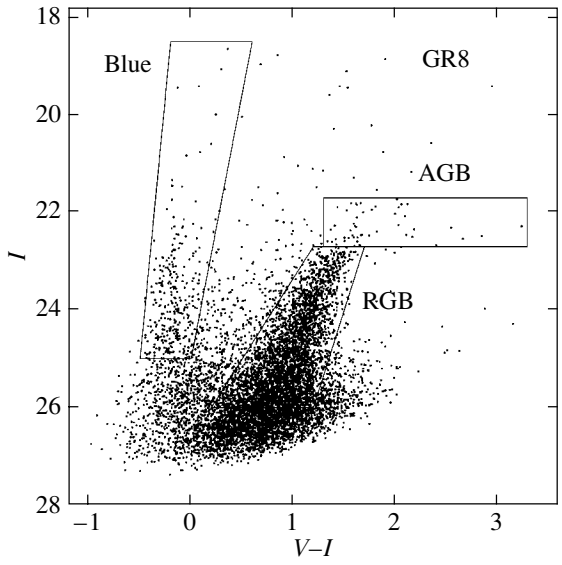

Fig. 2. Color–Magnitude diagram for stars of the galaxy GR8. Regions of young ("blue"—blue supergiants and giants), intermediate ("AGB"—asymptotic giant branch), and old ("RGB"—red giant branch) stars are marked.

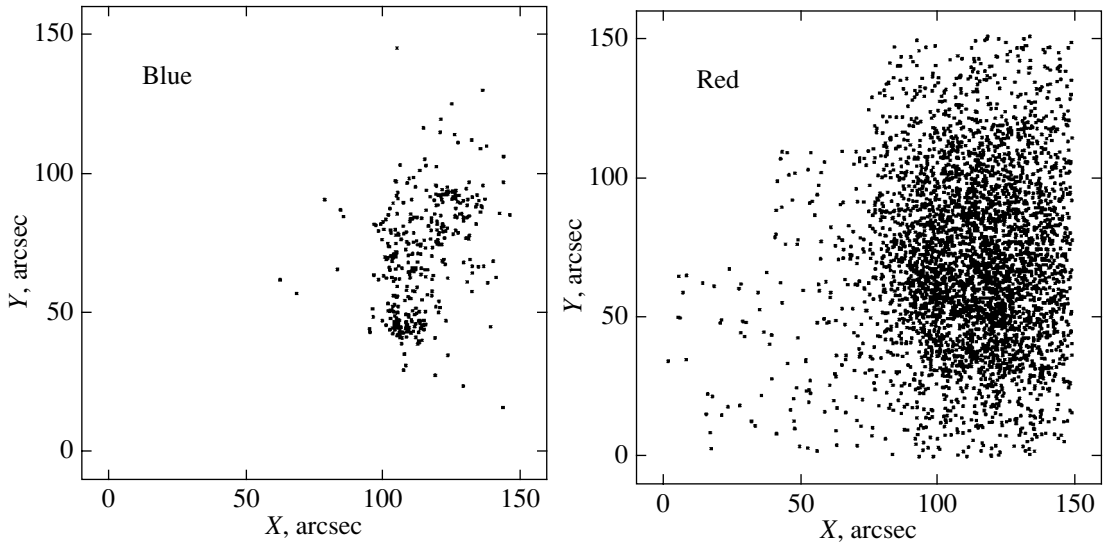

Fig. 3. Distributions of young (blue, left-hand plot) and old (red, right-hand plot) stars in GR8. All the young stars are concentrated near the central region of the galaxy, whereas the red giants form an extended structure resembling a thick disk.

of all the images, including dark-current subtraction, elimination of irregularities of the CCD sensitivity by dividing the image by a flat field taken at dusk, and removal of cosmic-ray traces and "hot" pixels. The images obtained from the HST archive did not require this procedure, which was performed automatically when we ordered the images from the archive. We extracted data for the stars and carried out the photometric measurements using the standard DAOPHOT II procedure in the MIDAS package [17]. To translate the instrumental magnitudes into the Kron–Cousins system, we carried out photometric observations of standard stars from the list of Landolt [18] on each night to derive the equations for the translation from the instrumental magnitudes to the $BVRI$ system.

The photometric measurements produced a list of coordinates, magnitudes, and accompanying parameters for the stars, which could be used to assess the photometric accuracy and differences of the photometric profiles of the objects studied from a standard stellar profile.

4. MEASUREMENT OF THE SURFACE DENSITY OF STARS

Figure 1 shows GR8, which is a typical irregular galaxy in our list. Figure 2 shows the Hertsprung–Russell diagram for this galaxy based on our stellar photometry, with regions occupied by different stellar types marked. We constructed distributions of various types of stars projected onto the plane of the galaxy (Fig. 3) and calculated the surface density of stars within annuli centered on the galaxy. We made the necessary corrections for the incompleteness of the stellar sample due to the asymmetric distribution of the four chips of the HST field relative to the center of the galaxy.

Figure 4 shows the results for the 12 galaxies in the form of plots of the density distributions for young (blue and red supergiants) and old (red giants) stars.

Star-forming processes that produce bright supergiants occur in all irregular galaxies. The presence of bright stars and the nonuniform background brightness distribution in star-forming regions hinder photometry of relatively faint stars, including red giants. As a result, the density of red giants is underestimated in the central regions of galaxies, as can be seen in Fig. 4. Another effect that decreases the calculated stellar density in central regions of galaxies is the "blending" of stellar images due to the extreme crowdedness of the stars in the central regions of galaxies. The DAOPHOT program for stellar photometry removes such images from the list, interpreting them as nonstellar. This decreases both the completeness of the sample and the calculated surface density of the stars, especially in the central regions of galaxies. We were able to compensate for these effects using the standard procedure of artificial-star photometry. However, the statistical influence of these effects is insignificant for stars at the periphery, and we excluded the parameters of the stellar distributions near the galactic centers when deriving the parameters for the exponential radial decrease of the stellar density.

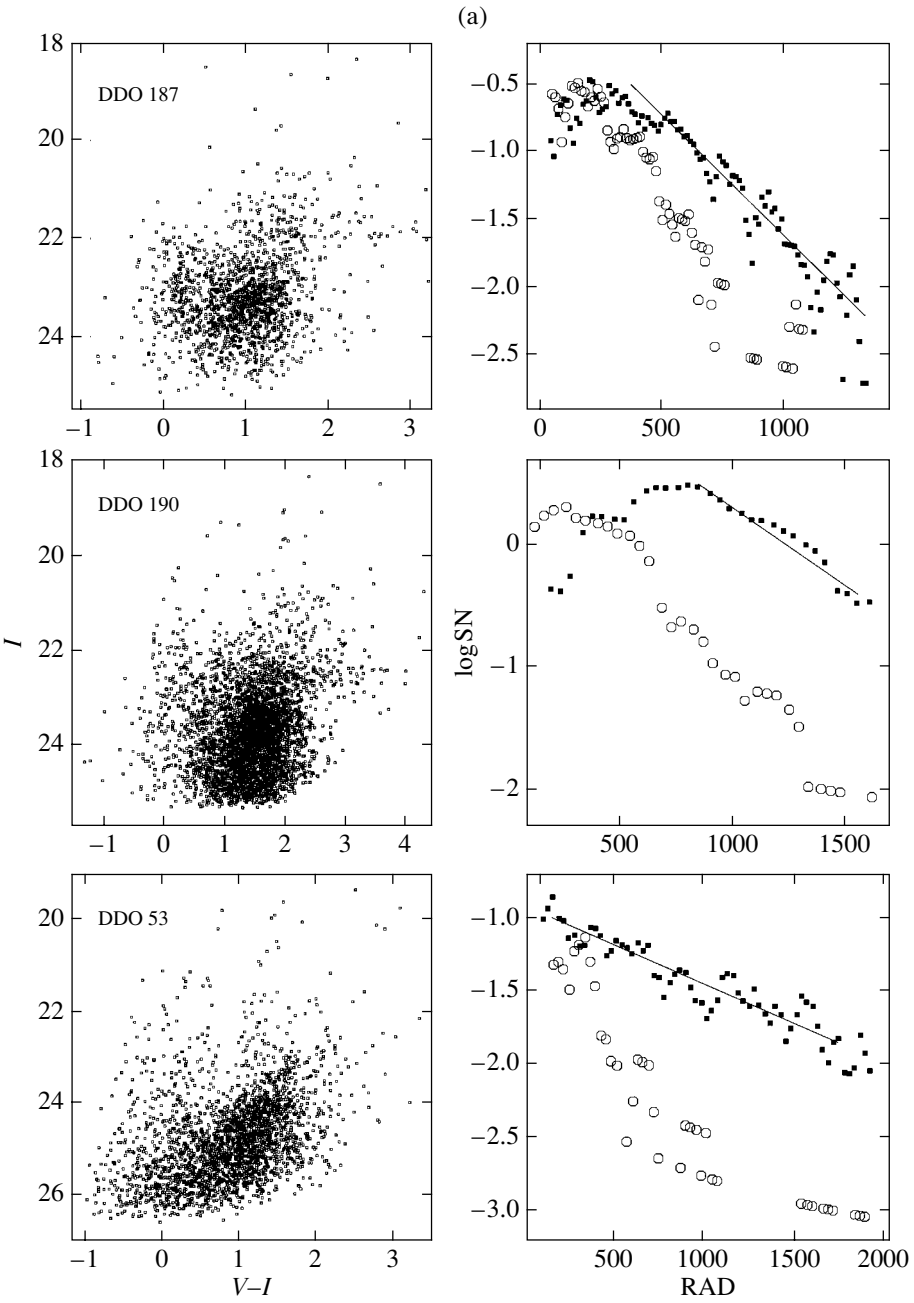

Fig. 4. Color–magnitude diagrams and radial distributions of stellar density in irregular galaxies (distance—in pc, star density—in relative units). All the color–magnitude diagrams show both young, blue stars (open circles) and stars with ages of several billion years (filled squares). On the radial-distribution plots, young stars occupy the visible regions of the galaxies, whereas the red giants, whose density decreases exponentially from the center, can easily be traced to much greater galactocentric distances.

5. STRUCTURE OF THE IRREGULAR GALAXIES

The results shown in Fig. 4 demonstrate that, despite the seemingly chaotic nature of the distribution of star-forming regions, they are nonetheless appreciably concentrated toward the centers of their galaxies, as can be seen in the density distributions for the young stars. It is obvious from a comparison of the morphologies of galaxies with different masses that the star-forming regions in more massive galaxies begin to be concentrated into spiral-arm type structures, which, however, remain barely distinguishable.

While the young, blue stars are concentrated in star-forming regions, giving the galaxy its irregular appearance, the red giants have a smoother distribution. Their surface-density contours accurately indicate the center of the galaxy, and can be used to estimate its inclination to the line of sight. In all

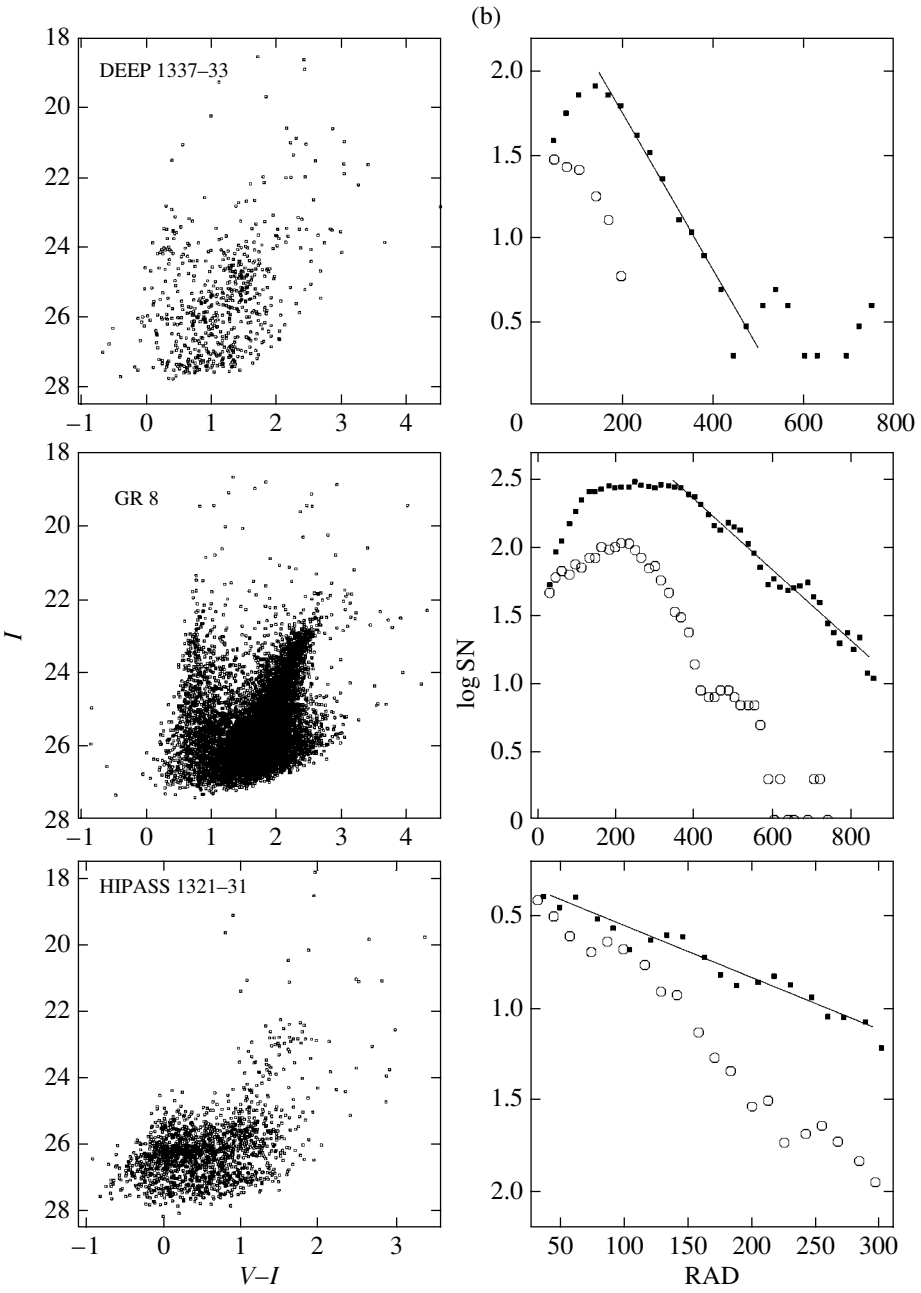

Fig. 4. (Contd.)

the galaxies, the red supergiants extend much farther from the center than the blue giants (Fig. 4). The ratio of the sizes of the corresponding spatial structures can reach five (IC 10), but its mean value is 2.5–3.0. The domains occupied by red giants have fairly well-defined boundaries, with very few, mostly foreground, stars seen beyond them. An analysis of the density distribution of red giants in IC 10 revealed a thick disk with a sharp boundary [15]. An even larger structure extending beyond the thick disk has a different density gradient than the thick disk. Thus, this galaxy exhibits a complex structure consisting of a thick disk and halo, similar to the structure of spiral galaxies [19, 20]. IC 10 differs from the other irregular galaxies in our list only in its luminosity (mass), suggesting that it is a galaxy's mass that determines whether it has a genuine halo. Although the small numbers of such galaxies prevent us from drawing firm conclusions, this observational fact can, nevertheless, be easily explained if there is an overall population of disk galaxies, whose low-mass and high-mass members have come to be known as irregulars and spirals,

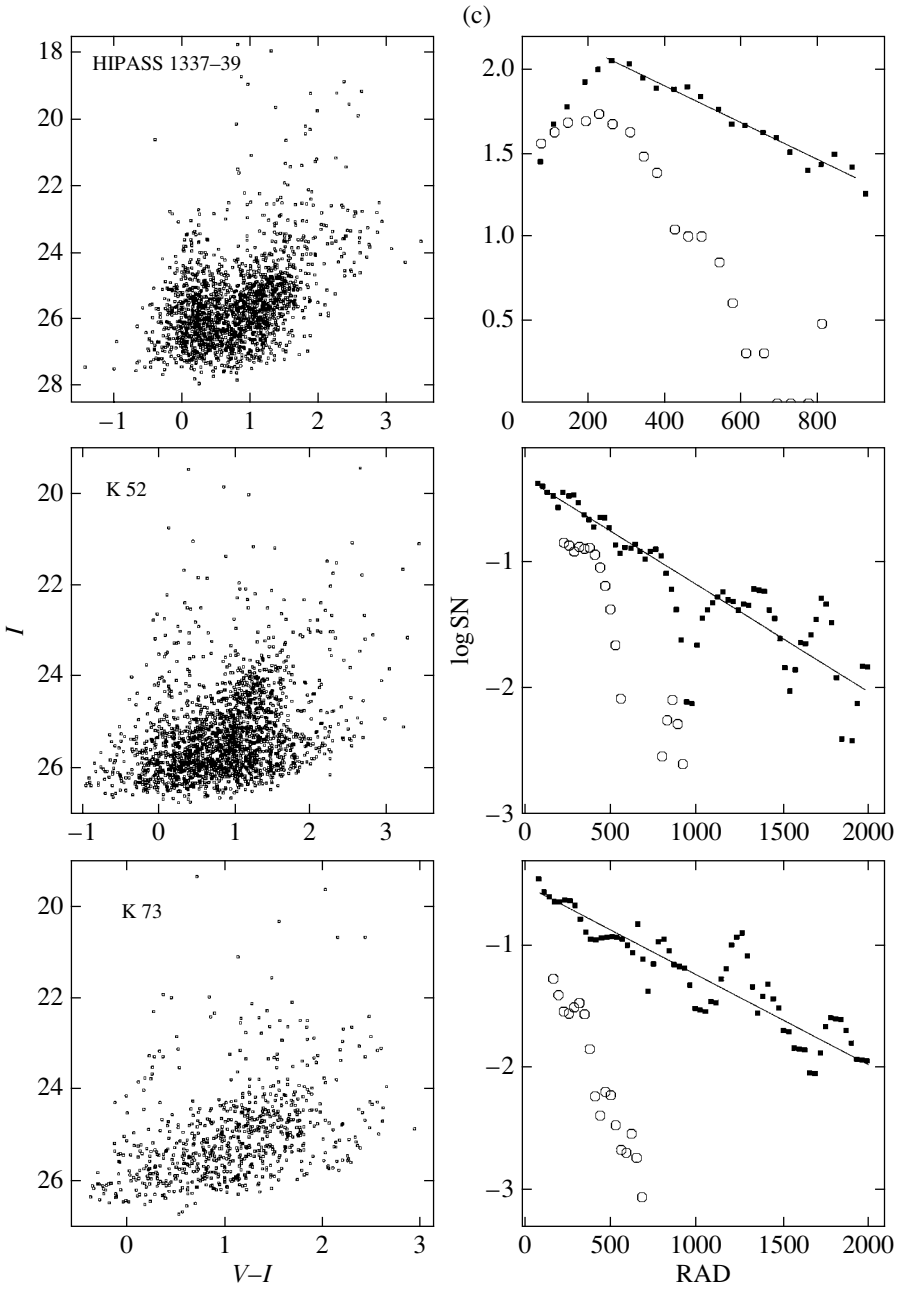

Fig. 4. (Contd.)

respectively. The reality of such a unified scheme is supported by the continuous range of physical parameters for irregular and spiral galaxies. In this case, the presence of a halo around a galaxy is determined only by the mass of the galaxy, and not by its membership in some artificially defined class of irregular or spiral galaxy.

The stars at the peripheries of galaxies have stable orbits, implying that all evolved invisible stars should be located within the boundaries outlined by the current distribution of red giants. In other words, if the dark matter in galaxies consists of the remnants of stellar evolution, the boundaries of the distribution of this matter can be determined by analyzing the distribution of red giants.

6. CONCLUSIONS

Our analysis of the stellar populations in 12 irregular face-on galaxies has led to the following conclusions.

(1) The radial distributions of stars of different types in the galaxy show exponential decreases, similar to the behavior of a disk component. The rate at

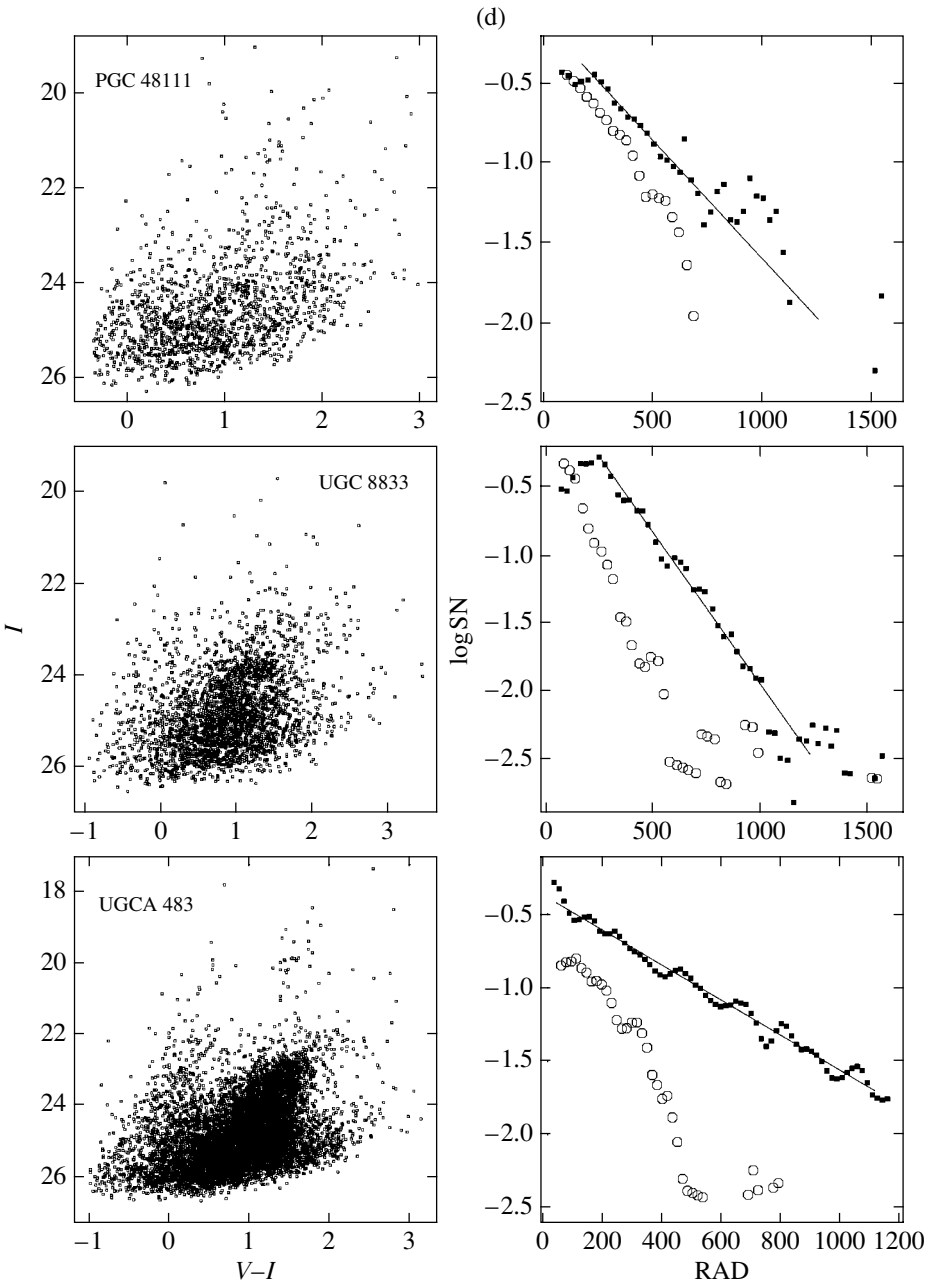

Fig. 4. (Contd.)

which the stellar density in a given galaxy decreases depends on the age of the stars. Younger stars show more rapid density decreases toward the periphery than older stars.

(2) The stellar populations of galaxies have fairly sharp boundaries if these boundaries coincide with the cutoff of the disk formed by red giants.

(3) Our stellar density measurements show that old stars form disks that extend a factor of two to three further than the visible isophotal sizes at $25^m/\mathrm{arcsec}^2$.

(4) All these conclusions refer to dwarf galaxies. Our preliminary studies show that massive irregular galaxies may possess a more extended genuine halo, in addition to a thick disk, as is observed in IC 10.

ACKNOWLEDGMENTS

This work was supported by the Russian Foundation for Basic Research (project nos. 00-02-16584 and 03-02-16344). Our work has made use of data from the NASA/IPAC Extragalactic Database.

REFERENCES

1. D. Pushe, D. Westphahl, *et al.*, Astron. J. **103**, 1841 (1992).
2. E. Wilcots and B. Miller, Astron. J. **116**, 2363 (1998).
3. A. Sandage, *The Hubble Atlas of Galaxies* (Carnegie Inst., Washington, 1961).
4. P. Hodge and J. Hitchcock, Publ. Astron. Soc. Pac. **78**, 79 (1966).
5. T. Bremens, B. Bingelli, and P. Prugniel, Astron. Astrophys., Suppl. Ser. **129**, 313 (1998).
6. T. Bremens, B. Bingelli, and P. Prugniel, Astron. Astrophys., Suppl. Ser. **137**, 337 (1998).
7. W. Baade, *Evolution of Stars and Galaxies* (Harvard Univ. Press, Cambridge, 1963).
8. D. Minniti and A. Zijlstra, Astron. J. **114**, 147 (1997).
9. A. Aparicio, N. Tikhonov, and I. Karachentsev, Astron. J. **119**, 177 (2000).
10. R. Lynds, E. Tolstoy, E. J. O'Neil, and D. Hunter, Astron. J. **116**, 146 (1998).
11. D. Martinez-Delgado, K. Gallart, and A. Aparicio, Astron. J. **118**, 862 (1999).
12. D. Minniti, A. Zijlstra, and V. Alonso, Astron. J. **117**, 881 (1999).
13. A. Aparicio and N. Tikhonov, Astron. J. **119**, 2183 (2000).
14. B. Letarte, S. Demers, P. Battinelli, and W. Kunkel, Astron. J. **123**, 832 (2002).
15. N. A. Tikhonov, Doctoral Dissertation (St. Petersburg, 2002).
16. N. Tikhonov and O. Galazutdinova, Astron. Astrophys. **394**, 33 (2002).
17. P. Stetson, *Users Manual for DAOPHOTII* (1994).
18. A. U. Landolt, Astron. J. **104**, 340 (1992).
19. J. Guillandre, J. Lequeux, and L. Loinard, in *IAU Symposium No. 192: The Stellar Content of Local Group Galaxies*, Ed. by P. Whitelock and R. Cannon (1988), p. 27.
20. N. Tikhonov and O. Galazutdinova, Astron. Astrophys. (2004) (in press).

Translated by A. Dambis

Astronomy Reports, Vol. 49, No. 7, 2005, pp. 510–519. Translated from Astronomicheskiĭ Zhurnal, Vol. 82, No. 7, 2005, pp. 573–583.

Evolution of Galaxies and the Tully–Fisher Relation

E. P. Kurbatov, A. V. Tutukov, and B. M. Shustov

Institute of Astronomy, Moscow, Russia

Received January 10, 2005; in final form, February 17, 2005

Abstract—We study the evolution of the [O/Fe]–[Fe/H] relation and the dependence of the iron abundance on distance from the galactic plane z in a one-zone model for a disk galaxy, starting from the beginning of star formation. We obtain good agreement with the observational data, including, for the first time, agreement for the [Fe/H]–z relation out to heights of 16 kpc. We also study the influence of the presence of dark matter in the galaxies on the star-formation rate. Comparison of the observed luminosity of the Galaxy with the model prediction places constraints on the fractional mass of dark matter, which cannot be much larger than the fractional mass of visible matter, at least within the assumed radius of the Galaxy, ∼20 kpc. We studied the evolution of disk galaxies with various masses, which should obey the Tully–Fisher relation, $M \propto R^2$. The Tully–Fisher relation can be explained as a combination of a selection effect related to the observed surface brightnesses of galaxies with large radii and the conditions for the formation for elliptical galaxies. © *2005 Pleiades Publishing, Inc.*

1. INTRODUCTION

Many thousands of theoretical papers have been written on the evolution of galaxies, often applying sophisticated mathematical methods: N-body models, multidimensional gas-dynamical models, statistical methods, etc. However, a number of very important results can be obtained using methods that are relatively simple and are not computationally demanding. In [1–5], we suggested and implemented an approach that is both simple mathematically and reasonably self-consistent in the treatment of all complex physical processes determining the evolution of a galaxy.

In mathematical terms, this evolution reduces to the solution of two equations. One defines the star-formation rate (SFR) assuming the complete ionization of the gas component of the galaxy, which is taken to be homogeneously distributed over the galactic disk. The other equation describes variations of the thickness of the galactic disk based on the condition of virial equilibrium, the input of mechanical energy into the gas component by supernovae, and the dissipation of energy due to collisions of gas clouds. Numerical modeling must also take into account the evolution of the galactic stellar component: the return of matter to the interstellar medium by old stars after the formation of the endproducts of their evolution—black holes, neutron stars, and degenerate dwarfs—and the exchange of matter between the galaxy and intergalactic medium.

Despite the simplicity of this approach, it led to a fairly complete picture of the evolution of disk galaxies—in particular, the Milky Way—that was consistent with observations. This made it possible for the first time to distinguish the role of the loss of heavy elements from the Galaxy during the formation of the radial chemical-composition gradient, and to derive self-consistent distributions of metals in the z direction over a scale of ∼2 kpc. This provided an explanation for the origin of enhanced metallicities (by a factor of a few over the solar value) of galaxies harboring quasars in their nuclei, via the enhanced density and higher minimum mass of the stars in these regions [5].

The present paper continues our study of the evolution of disk galaxies using the model developed by us earlier. This model enabled us to trace the chemical evolution of galaxies starting from their formation. However, the absence of data on very old, low-metallicity stars prevented comparison of the model results with observational data for the initial stages of the evolution of the Galaxy. New data for stars with extremely low metallicities has recently become available, making it possible to trace the early stages of the enrichment of the Galaxy in heavy elements. Section 2 discusses the evolution of abundances implied by our theoretical modeling. Section 3 discusses modern data on the distribution of metals in the direction of the Galactic rotational axis on scales of 16 kpc. In our previous studies, we used only fairly old data on stars that are located not further than 3 kpc from the disk—again hindering application of the model to the earliest stages of Galactic evolution. Another important circumstance influencing the evolution of the Galaxy is the presence of dark matter in the Galaxy.

1063-7729/05/4907-0510$26.00

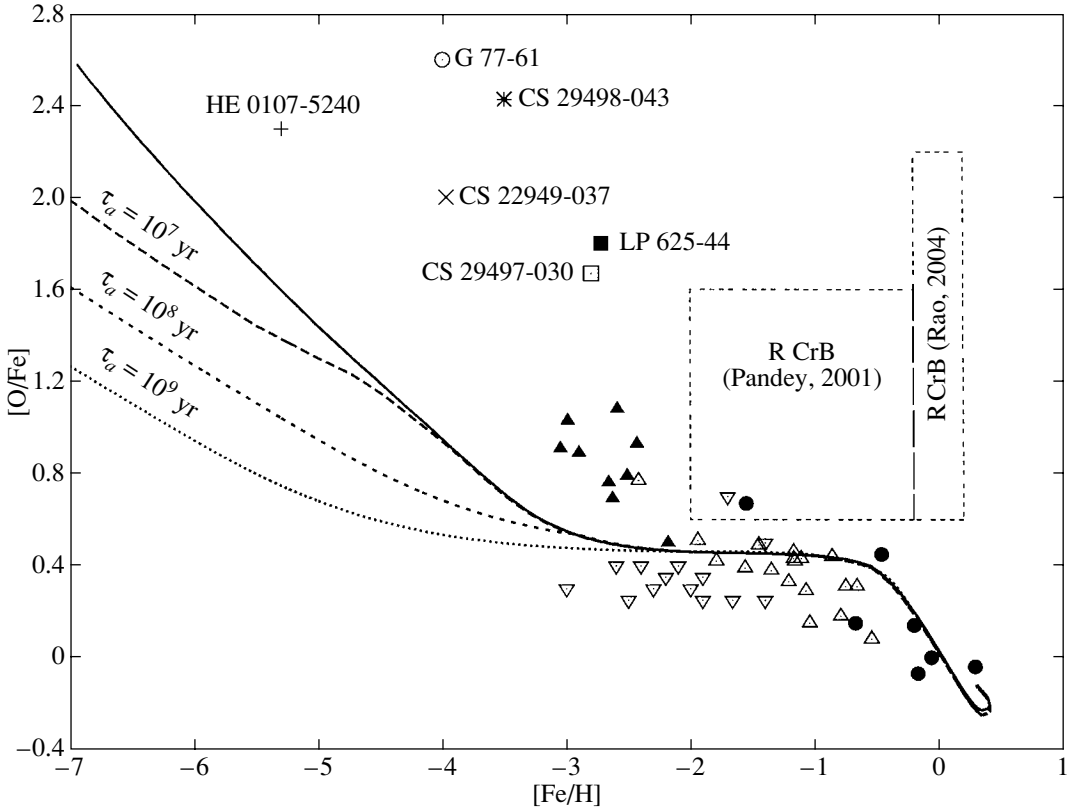

Fig. 1. [O/Fe]–[Fe/H] dependence for models with various initial accretion times τ_a. The solid curve shows the standard model ($\tau_a = 0$). The filled circles show data on subgiants [11], open triangles data on subgiants and main-sequence stars [12], filled triangles data on subdwarfs [13], inverted open triangles data on halo giants [14], and rectangles the positions of R CrB stars [15, 16]. The remaining objects are HE 0107-5240 [17], CS 22949-037 [18], CS 29498-043 [19], CS 29497-030 [19], LP 625-44 [19], and G 77-61 [20].

The nature and properties of dark matter are far from fully understood (see, e.g., the review [6]), but the necessity of taking this factor into account is beyond doubt. Section 4 presents an estimate of the fractional mass of dark matter obtained in our model.

The good agreement of the model results with the observations encourages us to use the model to interpret various statistical relations (mass–metallicity, mass–luminosity, etc.). In recent years, possibilities for applying the Tully–Fisher relation [7], which was discovered in 1977 by the two named authors, in various studies of galaxies have been widely discussed. This law relates the luminosity and rotational velocity of a disk galaxy. There are various ideas about the origin of the Tully–Fisher relation. In Section 5, we suggest an explanation that seems to us quite natural, based on an analysis of galactic evolution using our model. Finally, Section 6 presents a summary of our results.

We made some modifications to the set of standard parameters for the Galaxy for the computations; these are described in the corresponding sections.

2. EVOLUTION OF THE OXYGEN AND IRON ABUNDANCES

Analyses of the oxygen and iron abundances are the classical methods for testing our understanding of the evolution of stars and galaxies. These elements were adopted as tools for directly analyzing the abundances of the products of type I supernovae (SN Ia, which produce mainly iron) and type II supernovae (SN II or SN Ib,c, which produce mainly oxygen). The time between the formation of a massive star and its explosion as a SN II or SN Ib,c does not exceed $\sim 10^7$ yr. According to one possible scenario, SN Ia result from the mergers of degenerate dwarfs [8]. The lifetimes of SN Ia precursors cover a wide range, from 10^7 to 10^{10} yr, with the most probable values being from 2×10^8 to 2×10^9 yr [9]. The possibility that SN Ia make a significant contribution to the production of iron in the Galaxy at ages lower than $\sim 10^9$ yr is supported by the discovery of an [O/Fe] ratio equal to the solar value in a distant quasar [10] with $z = 6.4$ (age $\sim 7 \times 10^8$ yr). We have used here a standard model for the evolution of the Galaxy: the closed model with outer radius $R = 20$ kpc and

mass $M = 2 \times 10^{11}\,M_\odot$ described in [1]. The only difference is in the lifetime of SN Ia precursors (which was assumed to be 10^9 yr, close to the median value in the scenario for the evolution of close binaries [9]). In previous computations of the standard model [1], this time was taken to be 3×10^8 yr. Test runs have shown that this change does not result in any fundamental changes in the results of the computations; therefore, we shall adopt this modified model as our standard.

We considered the evolution of the [O/Fe]–[Fe/H] relation in a number of previous studies [1, 4, 5], using stars in the solar neighborhood with relative iron abundances [Fe/H] > -3. The metallicity range considered here is wider, extending to [Fe/H] $= -7$. The main results are presented in Fig. 1. When [Fe/H] < -1, the abundances of oxygen and iron are determined primarily by SN II explosions, leading to an overabundance of oxygen by a factor of two to four. At an age of $\sim 5 \times 10^8$ yr, SN Ia begin to explode, producing primarily iron [21] (in the closed model, this age corresponds to [Fe/H] ≈ -0.5). The ratio [O/Fe] begins to decline with time (along with the increase of [Fe/H]), and approaches the solar value at an age of several Gyr. The model provides an acceptable distribution for most stars with [Fe/H] > -3.

Among stars with the solar abundance of heavy elements, it has long been known that R CrB stars have abnormally high abundances of oxygen and carbon. The positions of R CrB stars with solar iron abundances are plotted in Fig. 1, based on the data of [15]; low-metallicity ([Fe/H] $\approx -0.5 \ldots -2.0$) R CrB stars are plotted based on the data of [16]. The overabundance of oxygen in R CrB stars reaches nearly two orders of magnitude, and may be nearly independent of [Fe/H] (Fig. 1). The reason for the overabundance of O and C in R CrB stars is the episodic penetration of the convective envelope of the star on the asymptotic giant branch onto the layer enriched in the products of helium burning [22]. This process enhances the observed abundances of C, O, and N in red supergiants by nearly two orders of magnitude. This oxygen-enrichment mechanism is possible only for red (super)giants with luminosities that are more than two orders of magnitude higher than the solar luminosity. Stars of lower mass may become enriched in carbon or oxygen due to mass exchange between the components of close binaries. This may explain the origin of such oxygen-rich stars as LP 625-44 and CS 29497-030 [19]. Stars with carbon abundances [C/H] $= 2$ and [Fe/H] $= -4$ are known [23].

An increasing number of observations of stars with [Fe/H] < -3 have been reported in recent years. The very low metallicities of these stars reflect the earliest stages of the evolution of the Galaxy [24]. Such stars can be arbitrarily separated into two groups (Fig. 1). The first group contains stars that show a substantial excess of oxygen relative to the model: G 77-61 [20], CS 29498-043 [19], CS 22949-037 [18], CS 22957-027 [25] ([O/Fe] ≈ 2, [Fe/H] $= -3.11$), and CS 31062-012 [25] ([O/Fe] ≈ 2, [Fe/H] $= -2.55$), and R CrB. The second group contains the giant HE 0107-5240 [17]. While the O excesses in stars of the first group can be explained by the penetration of their convective envelopes into the layer enriched in oxygen or by mass exchange between binary components, the oxygen overabundance in the stars with the lowest metallicities may be primordial, indicating that they formed during the first $\sim 10^7$ yr of the Galaxy's existence. Figure 1 shows that the [O/Fe] ratio in the earliest stages of the Galaxy's evolution is very high, and decreases with age. Since SN Ia have not yet started to enrich the interstellar medium in iron, a natural question arises: What is the reason for this behavior of [O/Fe]?

The reason for the increase of the [O/Fe] ratio is the increase in the production of oxygen and the decrease in the production of iron with increasing initial masses of SN II precursors. According to the numerical models [26, 27], the amount of oxygen M_O produced by stars with masses of 15–120 $M_\odot$ can be written

$$\frac{M_\mathrm{O}}{M_\odot} = 0.01 \left(\frac{M_\mathrm{i}}{M_\odot}\right)^{1.7},$$

where M_i is the initial mass of the star. The amount of iron produced by 13–25 $M_\odot$ stars can be estimated as [27]

$$\frac{M_\mathrm{Fe}}{M_\odot} = 21 \left(\frac{M_\mathrm{i}}{M_\odot}\right)^{-1.87}.$$

Combining these relations, we obtain

$$\frac{M_\mathrm{O}}{M_\mathrm{Fe}} \approx 5 \times 10^{-4} \left(\frac{M_\mathrm{i}}{M_\odot}\right)^{3.57}. \qquad (1)$$

This expression is valid for $13 < M_\mathrm{i}/M_\odot < 120$, since only stars of these masses were studied in [26, 27]. Of course, when working with (1), we must bear in mind that, while the production of oxygen by massive stars is estimated relatively accurately, the iron yield remains uncertain. It may depend on several parameters that are not accurately known, such as the initial chemical composition of the stars, the rotational velocity of the presupernova core, the magnetic-field strength, etc. It is clear from observations that the iron yield may be even smaller than the models [27] predict. For instance, SN 1997D, with a total mass of $\sim 25\,M_\odot$, ejected only $2 \times 10^{-3}\,M_\odot$ of nickel (which

produces iron as it decays) [28], much less than the $\sim 0.05\,M_\odot$ expected from the models [27]. On the other hand, SN 2002ap, with an initial mass of $\sim 25\,M_\odot$, produced $0.07\,M_\odot$ of nickel [29], close to the model expectations.

According to (1), obtaining the ratio [O/Fe] ≈ 2 observed in the extreme low-metallicity star HE 0107-5240 (Fig. 1) requires a supernova with an initial mass of $\sim 50\,M_\odot$ and an age of 3×10^6 yr. Thus, judging from the iron abundance, HE 0107-5240 is among the first stars to be formed in the Galaxy, during the first several million years of its existence. Stars with [Fe/H] $\lesssim -3$ have masses of the order of a solar mass. This suggests that the initial enrichment of the Galaxy in heavy elements was accomplished by ordinary stars with masses from $\sim 1\,M_\odot$ to $\sim 100\,M_\odot$.

The metallicity of the first Galactic stars could grow due to the accretion of interstellar gas. If the radius for capturing interstellar gas by a star is $r = 2GMv^{-2}$, where G is the gravitational constant, M is the mass of the star, and v is its relative velocity, the star can accrete during the lifetime of the Galaxy a mass

$$\frac{\Delta M}{M_\odot} \approx 10^{-5}\frac{n_{\rm H}}{v_{30}^3}, \qquad (2)$$

where $n_{\rm H}$ is the current number density of the hydrogen in the gaseous phase (in cm^{-3}) and v_{30} is the relative velocity (in units of 30 km/s). According to (2), even in stars that are completely devoid of heavy elements, the relative iron abundance could become equal to that observed in HE 0107-5240 (Fig. 1) due to accretion (if there is a negligible role of the stellar wind, low mixing efficiency in the outer layers of the star, etc.). Note that low-metallicity stars could have initially belonged to a former low-mass satellite that merged with the Galaxy in the past. The evolution of the chemical composition of low-mass spheroidal galaxies may end in an early phase, after loss of the gaseous component. Naturally, stars in such a galaxy could retain their high [O/Fe] values.

For completeness, we note an additional possible means of enrichment of population-III low-mass stars (which are initially devoid of heavy elements) in metals. Most stars are formed in stellar clusters, which, as a rule, are disrupted almost immediately after their formation because of the loss of the gaseous component due to the formation of HII regions and supernova explosions [30]. The first stars may also have formed in clusters. Then, some fraction of the lost gas, along with the products of the first, most massive, supernovae, would be captured by low-mass stars with the initial low-metal chemical composition. The capture radius is $r \approx 2GM_*v_{\rm ex}^{-2}$, where $M_* \approx M_\odot$ is the mass of the cluster star and $v_{\rm ex}$ is the velocity of the expanding gaseous envelope of the cluster. The fraction of the captured matter will then be

$$\alpha = \frac{G^2M_*^2}{v_{\rm ex}^4R^2} = \left(\frac{v_{\rm ff}}{v_{\rm ex}}\right)^4 N^{-2}, \qquad (3)$$

where R is the cluster radius, $v_{\rm ff}$ is the free-fall velocity at the edge of the cluster, and N is the number of stars in the cluster (assuming that all have the solar mass). If we assume that $v_{\rm ff} = v_{\rm ex}$, $N = 10^3$ and $M_{\rm Fe} \approx 0.01\,M_\odot$ ($M_{\rm O} \approx 50\,M_\odot$ [27]), then a solar-mass star can capture $\sim 10^{-8}\,M_\odot$ of iron. The iron abundance in Sun is $\sim 10^{-3}\,M_\odot$. This produces a star with an iron abundance of [Fe/H] ≈ -5, similar to that observed in HE 0107-5240 (Fig. 1). It is obvious that a high oxygen abundance will be observed, since stars with masses exceeding $\sim 50\,M_\odot$ have [O/Fe] ≈ 2, as was shown above. Note that not all the parameters in (3) are well enough known to enable confident conclusions about the role of this mechanism in the enrichment of population-III stars in heavy elements. The accretion of interstellar gas enriched in heavy elements produced by the first stars may substantially complicate, or even make impossible, the identification of low-mass population-III stars.

Note that the [O/Fe]–[Fe/H] evolutionary curve obtained for the closed model shown in Fig. 1 represents an upper bound for the oxygen abundance. In low-mass disk galaxies, the products of SN II explosions can efficiently leave the parent galaxies via the formation of supershells [31], thereby reducing the growth rate of the oxygen abundance in these galaxies. Since type Ia supernovae do not produce supershells, the iron abundance in low-mass disk galaxies increases at the usual pace. The example provided by the galaxy IZw 38 [32], which has active star formation with [Fe/H] $= -1.76 \pm 0.12$ and [O/Fe] $= -0.3 \pm 0.3$, shows that the loss of the products of type II supernovae may, indeed, be very important for dwarf galaxies. As our model computations show, allowing for the loss of type II supernova products in massive galaxies does not lead to any substantial differences in the [O/Fe]–[Fe/H] distribution. Moreover, special runs of the model taking into account the finite time for the accumulation of the Galactic matter show that increasing the Galaxy's formation time substantially reduces the [O/Fe] ratio at low [Fe/H] (Fig. 1). Increasing the amount of data on low-metallicity stars in the future may enable estimation of the time for the accumulation of the Galaxy's mass.

3. DISTRIBUTION OF HEAVY ELEMENTS ABOVE THE GALACTIC DISK

Let us now consider the distribution of heavy elements with height z above the Galactic disk.

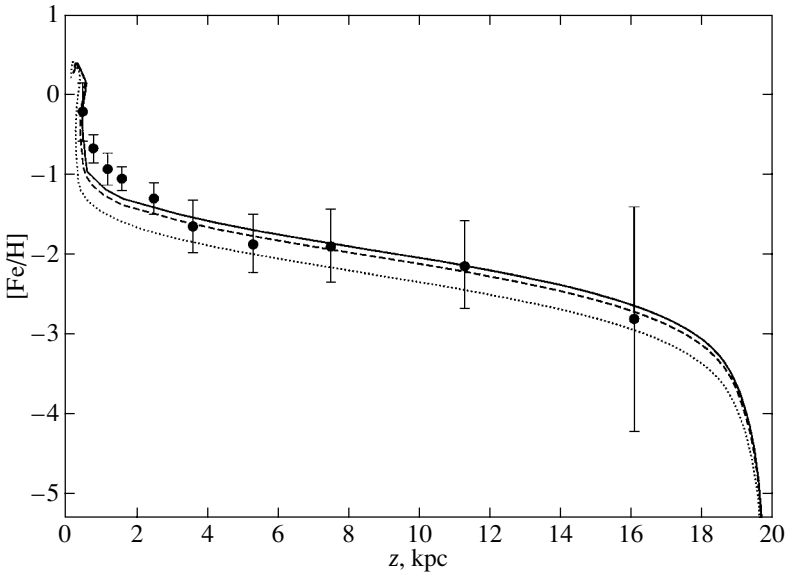

Fig. 2. Distribution of iron abundance with height above the Galactic plane in the standard model (solid curve) and in a model taking into account the loss of heavy elements due to SN II explosions, for fractional masses of heavy elements lost equal to 0.16 (dashed curve) and 0.5 (dotted curve). The solid circles show the data from [37].

Various observations show that the metallicity gradient with z measured using field stars may reach -0.65/kpc (according to data for the thin disk [33]), while the lowest value obtained from observations of open clusters is -0.34/kpc [34]. At the same time, some observations of field and open-cluster stars show no evidence for a metallicity gradient [35, 36]. To summarize, at $z < 4$ kpc, the gradient is in the range $(-0.55 \ldots -0.33)$/kpc, while it is in the range $(-0.18 \ldots 0.0)$/kpc at larger z [37].

In the standard model, we adopted the value of [Fe/H] as a function of the disk semi-thickness for the dependence of the iron abundance on the height above the Galactic plane. This dependence is shown in Fig. 2, along with data from [37]. We can distinguish three regions with different metallicity gradients: $d[\mathrm{Fe/H}]/dz = -3$/kpc for $z < 0.7$ kpc, $d[\mathrm{Fe/H}]/dz = -0.2$/kpc for $0.7 < z < 5$ kpc, and $d[\mathrm{Fe/H}]/dz = -0.1$/kpc for $5 < z < 16$ kpc. This corresponds to different iron abundances in stars of the thin disk, thick disk, and halo, and also to different spatial scales within these components.

Computations of galactic evolution allowing for the loss of heavy elements (Fig. 2) and accretion have shown that the "openness" of the galaxy weakly influences the model dependence of [Fe/H] on z. Thus, our one-zone model can explain well the variations of the distribution of heavy elements with z.

4. EVOLUTION OF A DISK GALAXY: THE INFLUENCE OF DARK MATTER

The main results obtained for the standard model are listed in the table. Comparison with observations indicates that this model provides an adequate description of the chemical and dynamical evolution of the Galaxy, as well as of its star-formation history. For example, the data of [38] provide evidence that young galaxies with $\dot{M}_* \approx 10$–$100\,M_\odot$/yr have optical depths of $\sim$5–10 in the direction perpendicular to the plane of the disk, as is confirmed by our model. The large optical depths of distant, and thus young, galaxies could influence the extragalactic distance scale (which is based on the assumption that SN Ia are standard candles), and therefore conclusions concerning the regime of the cosmological expansion. We should also bear this in mind in connection with analyses of the brightness of supernovae at $z = 2$–5. Variation of the time to accumulate the mass of the Galaxy in the initial stage of its formation did not substantially influence the Galaxy's parameters after the Hubble time (Fig. 1).

Our model has another important parameter—the mass of dark matter, i.e., of matter (baryonic or otherwise) that cannot be directly observed, but provides a (sometimes dominant) contribution to the gravitational field. The fractional mass of dark matter is small on small scales. For instance, estimates of the fractional mass of dark matter in the Sun yield less than 2–5% [39], and this is probably true for other stars as well. On scales of 100 kpc or more, the fractional mass of dark matter may be much larger [6].

We studied the role of dark matter in the evolution of the Galaxy by changing the expression for the gravitational potential in the standard model to

$$E = \frac{GM_\mathrm{g}H_\mathrm{g}^2}{R^2}\left(\frac{M_\mathrm{G}}{H_*} + \frac{M_\mathrm{dm}}{R}\right),$$

Evolution of the main parameters of the standard Galaxy model with age (SFR is the star formation rate in $M_\odot$/yr, H_g is the semi-thickness of the gaseous disk, M_g is the mass of the gas, Z is the fractional mass of heavy elements, τ_{dust} is the optical depth of the dust, $L_{opt} = L_{bol}/\tau_{dust}(1 - e^{-\tau_{dust}})$ is the optical luminosity with allowance for absorption by dust)

t, yr	SFR	H_g, pc	$M_g/M_\odot$	Z	[O/H]	[Fe/H]	τ_{dust}	$L_{opt}/L_\odot$	$L_{bol}/L_\odot$
3.6×10^6	34.3	2.0×10^4	2.0×10^{11}	7.0×10^{-7}	−4.4	−6.9	0.0012	1.1×10^{10}	1.1×10^{10}
4.8×10^6	34.4	2.0×10^4	2.0×10^{11}	2.0×10^{-6}	−3.9	−5.8	0.0034	1.2×10^{10}	1.2×10^{10}
6.3×10^6	34.5	2.0×10^4	2.0×10^{11}	4.3×10^{-6}	−3.6	−5.1	0.0072	1.3×10^{10}	1.3×10^{10}
8.2×10^6	34.7	2.0×10^4	2.0×10^{11}	7.5×10^{-6}	−3.4	−4.7	0.0012	1.3×10^{10}	1.4×10^{10}
1.0×10^7	34.9	1.9×10^4	2.0×10^{11}	1.2×10^{-5}	−3.2	−4.3	0.020	1.4×10^{10}	1.4×10^{10}
1.5×10^7	35.3	1.9×10^4	2.0×10^{11}	2.2×10^{-5}	−3.0	−3.8	0.036	1.5×10^{10}	1.6×10^{10}
2.5×10^7	36.2	1.9×10^4	2.0×10^{11}	4.3×10^{-5}	−2.7	−3.3	0.071	1.7×10^{10}	1.7×10^{10}
3.4×10^7	37.0	1.8×10^4	2.0×10^{11}	6.3×10^{-5}	−2.5	−3.1	0.10	1.8×10^{10}	1.9×10^{10}
4.4×10^7	37.9	1.8×10^4	2.0×10^{11}	8.4×10^{-5}	−2.4	−3.0	0.14	1.9×10^{10}	2.0×10^{10}
6.0×10^7	39.5	1.7×10^4	2.0×10^{11}	1.2×10^{-4}	−2.3	−2.8	0.20	2.0×10^{10}	2.2×10^{10}
7.3×10^7	40.9	1.6×10^4	2.0×10^{11}	1.5×10^{-4}	−2.2	−2.7	0.25	2.0×10^{10}	2.3×10^{10}
9.8×10^7	43.8	1.5×10^4	2.0×10^{11}	2.2×10^{-4}	−2.0	−2.5	0.36	2.2×10^{10}	2.6×10^{10}
1.2×10^8	47.0	1.4×10^4	2.0×10^{11}	3.0×10^{-4}	−1.9	−2.4	0.47	2.3×10^{10}	2.9×10^{10}
1.7×10^8	54.6	1.2×10^4	1.9×10^{11}	4.4×10^{-4}	−1.7	−2.2	0.72	2.5×10^{10}	3.5×10^{10}
2.5×10^8	69.7	8.7×10^3	1.9×10^{11}	7.2×10^{-4}	−1.5	−2.0	1.1	2.7×10^{10}	4.5×10^{10}
3.0×10^8	83.3	7.0×10^3	1.9×10^{11}	9.5×10^{-4}	−1.4	−1.8	1.5	2.9×10^{10}	5.5×10^{10}
4.0×10^8	123.7	4.3×10^3	1.8×10^{11}	1.6×10^{-3}	−1.2	−1.6	2.3	3.2×10^{10}	8.1×10^{10}
5.6×10^8	243.5	1.6×10^3	1.5×10^{11}	3.1×10^{-3}	−0.9	−1.3	4.0	3.6×10^{10}	1.5×10^{11}
7.1×10^8	342.7	6.2×10^2	1.1×10^{11}	6.9×10^{-3}	−0.5	−1.0	6.5	3.8×10^{10}	2.5×10^{11}
9.2×10^8	161.7	5.5×10^2	7.2×10^{10}	1.4×10^{-2}	−0.2	−0.6	8.6	2.4×10^{10}	2.0×10^{11}
1.2×10^9	76.1	4.9×10^2	4.7×10^{10}	2.1×10^{-2}	0.0	−0.4	8.2	1.6×10^{10}	1.3×10^{11}
1.6×10^9	33.7	5.4×10^2	3.3×10^{10}	2.7×10^{-2}	0.0	0.0	7.4	1.2×10^{10}	8.9×10^{10}
2.1×10^9	21.1	5.0×10^2	2.5×10^{10}	3.3×10^{-2}	0.1	0.3	6.8	9.8×10^9	6.7×10^{10}
2.9×10^9	12.8	4.1×10^2	1.8×10^{10}	3.8×10^{-2}	0.1	0.4	5.6	9.5×10^9	5.3×10^{10}
3.8×10^9	7.2	3.8×10^2	1.3×10^{10}	4.2×10^{-2}	0.2	0.4	4.4	9.4×10^9	4.2×10^{10}
4.9×10^9	4.4	3.5×10^2	9.5×10^9	4.4×10^{-2}	0.2	0.4	3.5	9.4×10^9	3.4×10^{10}
6.4×10^9	2.7	3.3×10^2	7.2×10^9	4.6×10^{-2}	0.2	0.4	2.7	9.5×10^9	2.8×10^{10}
8.7×10^9	1.6	3.1×10^2	5.4×10^9	4.7×10^{-2}	0.2	0.4	2.1	9.5×10^9	2.3×10^{10}
1.1×10^{10}	1.1	2.9×10^2	4.4×10^9	4.5×10^{-2}	0.2	0.3	1.6	9.1×10^9	1.9×10^{10}
1.5×10^{10}	0.8	2.8×10^2	3.6×10^9	4.3×10^{-2}	0.2	0.3	1.3	8.4×10^9	1.5×10^{10}

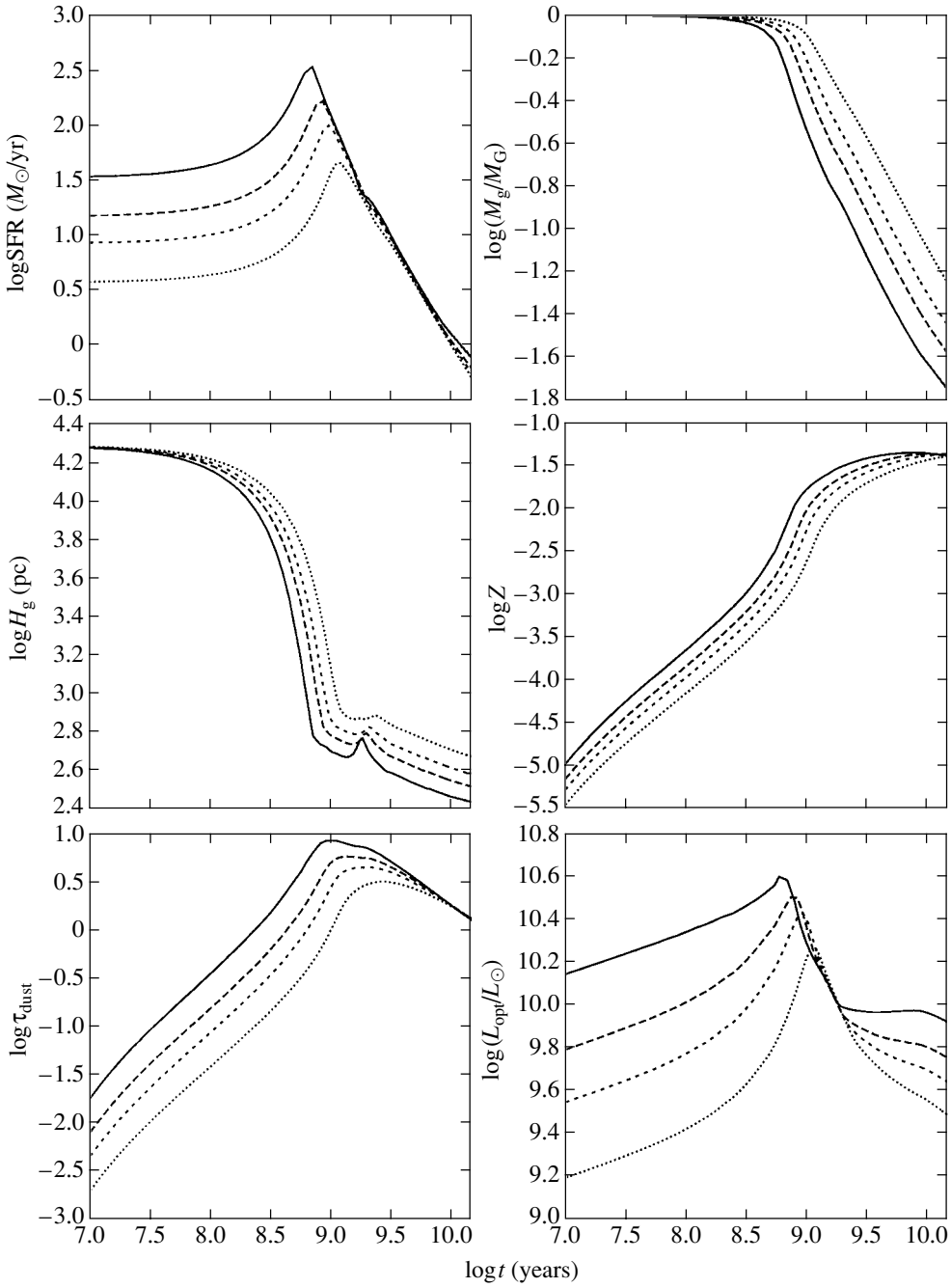

Fig. 3. Evolution of the Galaxy with allowance for dark matter. SFR is the star-formation rate, M_g/M_G is the ratio of the masses of gas and visible matter, H_g is the semi-thickness of the gaseous disk, Z is the heavy-element abundance, τ_{dust} is the optical depth of the dust, and L_{opt} is the optical luminosity with allowance for absorption by dust. Computational results are shown for ratios of the masses of dark and visible matter M_{dm}/M_G equal to 0 (solid curve), 0.5 (long dashed curve), 1.0 (short-dashed curve), and 2.0 (dotted curve).

where G is the gravitational constant, M_g is the mass of gas, H_g is the semi-thickness of the gaseous disk, M_G is the mass of visible matter, H_* is the semi-thickness of the stellar disk, M_{dm} is the mass of dark matter, and R is the radius of the disk. Figure 3 shows the evolution of the main parameters of the Galaxy as functions of the ratio of the masses of dark and visible matter, which was varied from zero (corresponding to the standard model) to two. Reduction of the mass of matter involved in star formation results in a delay of the star-formation burst, and so reduces the thickness of the gaseous disk. This is in qualitative agreement with estimates following from the observational relation between the relative thickness of the disk and the mass–luminosity relation for galaxies [40]. Increasing the mass-to-

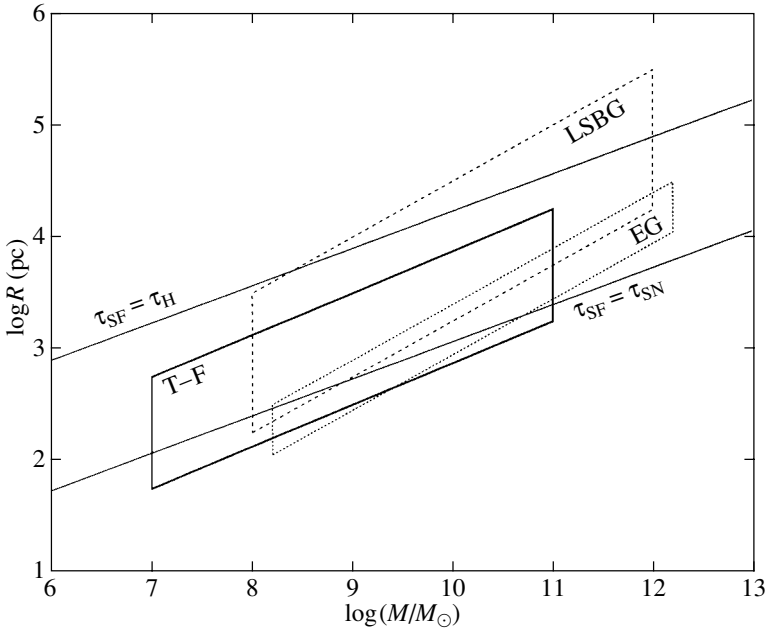

Fig. 4. Mass–radius diagram for various galaxies; galaxies obey the Tully–Fisher relation in the region T–F. The lines $\tau_{SF} = \tau_{SN}$ and $\tau_{SF} = \tau_H$ define the positions of galaxies with star-formation timescales τ_{SF} and τ_H, respectively. The region LSBG is occupied by low-surface-brightness galaxies [46, 48]. Early-type galaxies are located in the region EG [49, 50] (see Section 5).

luminosity ratio in the model decreases the galaxy's relative thickness. The observed optical luminosity of the Galaxy places constraints on the fractional mass of dark matter, <50%. Note that our initial mass function, $dN \propto M^{-2.35}dM$ for $M > 0.1\,M_\odot$, overestimates the number of low-mass stars compared to the observed value. According to [41], the observed mass function changes slope at $M \approx 1\,M_\odot$ ($dN \propto M^{-1.5}dM$ for $M < 1\,M_\odot$), which makes the fraction of stars with $<1\,M_\odot$ less pronounced. Thus, an excess of matter appears in our model compared to the observations. A simple analytical estimate of its fractional mass is ~37%.

5. TULLY–FISHER RELATION

About a quarter of a century ago, Tully and Fisher [7] discovered a dependence between the luminosity of a disk galaxy and its rotational velocity. In modern form, this relation can be written

$$\Delta M_B = (8 \pm 1)\Delta \log v_{rot}, \qquad (4)$$

where M_B is the absolute B magnitude of the galaxy and v_{rot} is the rotational velocity of the galactic disk, estimated from the flat part of the rotation curve. We can use the mass–luminosity relation for disk galaxies, $M/M_\odot \sim 10\,L/L_\odot$ [42], to estimate the relation between the mass of a disk galaxy M and its radius R. Assuming $v_{rot} \propto M^{1/2}R^{-1/2}$, we obtain

$$R \propto M^{0.5\pm0.07}. \qquad (5)$$

Relations similar to (4) for various groups of disk galaxies have been studied by numerous authors (see, e.g., [43–45]). If selection effects are not considered, it appears that the locations and slopes of the $\log R - \log M$ relation derived from (4) are fairly uncertain (they vary by about a factor of three for galaxies with masses from 10^7 to $10^{11}\,M_\odot$). The Tully–Fisher relation can be written $M = \pi\Sigma R^2$, where Σ is the surface density of gravitating matter. The observed range of Σ is rather wide. According to [46], disk galaxies display values $\Sigma \approx 10$–$600\,M_\odot/\mathrm{pc}^2$; another estimate yields $\Sigma = 20$–$1500\,M_\odot/\mathrm{pc}^2$ [47]. Figure 4 plots a mass–radius diagram for galaxies of various types that obey the Tully–Fisher relation (located inside the "T–F" region in this figure), elliptical and early-type galaxies (EG; [49, 50]), and low-surface-density galaxies (LSBG; [46, 48]).

We used (5) to compute a series of models with masses of 10^6–$4.5 \times 10^{11}\,M_\odot$. The results show that, in this range, the mass of a galaxy exerts almost no influence on the star-formation history or the evolution of the chemical composition. In particular, the final heavy-element abundance does not depend on the mass, in contradiction with the observed increase of the heavy-element abundance with increasing galactic mass and luminosity [51]. This may be explained by the intensive loss of heavy elements by low-mass galaxies.

Our formalism [2, 3] enables us to derive a simple relation defining the time scale for star formation in a

spherical galaxy [52]:

$$\tau_{\rm SF} = 3 \times 10^8 \frac{R_4^3}{M_{11}},$$

where R_4 is the galactic radius in units of 10^4 pc and M_{11} is the mass of its gaseous component in units of $10^{11}\,M_\odot$. The observed masses and radii of young galaxies are consistent with $\tau_{\rm SF} = 10^7$–10^9 yr [53]. The spherical model describes the early stages of the evolution of disk galaxies. We can place limits on the time for the existence of star-forming galaxies. An upper bound for the region they can occupy in Fig. 4 is given by the Hubble time: $\tau_{\rm SF} = \tau_{\rm H} = 1.4 \times 10^{10}$ yr, as is shown in Fig. 4. In galaxies located above this line, the SFR is so low that only a small fraction of the gas has been turned into stars over the Hubble time. Note that the position of this bound virtually coincides with the position occupied by low-surface-brightness galaxies [46, 48]. Nearby galaxies with masses of 10^6–$10^{12}\,M_\odot$ from the catalog [54] abut on the upper boundary of the region of star-forming galaxies (they are not shown in Fig. 4); the star-formation time scale in such galaxies is $\tau_{\rm SF} \approx 10^9$–$10^{10}$ yr.

On the other hand, the SFR in high-density galaxies is so high that almost all the gas has been transformed into stars even before the first explosions of SN II, whose precursors have lifetimes $\tau_{\rm SN} \approx 5 \times 10^6$ yr. This corresponds to the relation $\tau_{\rm SN} < \tau_{\rm SF}$, or $M_{11} > 60\,R_4^3$ (the line $\tau_{\rm SN} = \tau_{\rm SF}$ is also plotted in Fig. 4). As soon as the SN II begin to explode in these galaxies, they clean out any remaining gas. This is the scenario for the evolution for elliptical galaxies. The mass lost by old stars in these galaxies is unable to revive star formation, since SN Ia explosions drive the galactic wind, hindering star formation throughout the galaxy, with the possible exception of a circumnuclear region with a high gas density (see, for example, [55]). In fact, only a few percent of S0 and E galaxies show signs of star formation in their nuclei [56]. Some S0 and E galaxies may form via collisions of disk galaxies [57, 58]. However, the number of such galaxies is not large, since observations [59] show only a small increase in the fraction of E galaxies with the age of Universe; hence, most formed at large redshifts. Albeit with a fairly large scatter, the positions of early-type galaxies in Fig. 4 are close to the boundary defined by the relation $\tau_{\rm SF} = \tau_{\rm SN}$. However, elliptical galaxies formed in collisions of disk galaxies may also have larger sizes.

Figure 4 shows that the galaxies with active continuing star formation are located in a strip defined by the conditions $\tau_{\rm SN} = \tau_{\rm SF}$ and $\tau_{\rm SN} = \tau_{\rm H}$; the slope of this strip is close to the slope of the Tully–Fisher relation. This suggests that the power of the $R \propto M^\alpha$ law is determined by the similarity of the slopes of the boundaries of the region occupied by disk galaxies in the mass–radius diagram. At the lower boundary of this zone, galaxies that are initially elliptical are formed, while the upper boundary is apparently defined by two circumstances. The first is the condition that there be a sufficient SFR on a time scale that is shorter than the Hubble time. The second is the near coincidence of the upper boundary with the position of galaxies that have surface brightnesses at the detection limit. Galaxies with lower surface densities, $\Sigma < 10\,M_\odot/{\rm pc}^2$, are probably not detectable.

6. CONCLUSION

Our study of the evolution of a disk galaxy with star formation governed by ionization has enabled us to apply this model to several new fields. In particular, we have shown that high oxygen-to-iron abundance ratios are characteristic of the very first stars formed: $[{\rm O/Fe}] \approx 2$ when $[{\rm Fe/H}] \lesssim -5$. This is a result of the reduction in the iron production and increase in the oxygen production with increasing initial mass of type II supernovae. This suggests that some stars with low iron abundances and relatively high oxygen abundances (G 77-61, HE 0107-5240, Fig. 1) may be either the earliest second-generation stars or first-generation stars that are "contaminated" by products of the first supernovae. Our model distribution of metals with height H above the Galactic disk agrees with the observed distribution to $H \sim 16$ kpc. In our model, the well-known Tully–Fisher relation may stem from a combination of observational selection effects and conditions that are necessary for the formation of disk galaxies.

ACKNOWLEDGMENTS

This study was supported by the Presidential Program "Leading Scientific Schools of Russia" (NSh 162.2003.2), the Russian Foundation for Basic Research (project nos. 02-02-17524, 03-02-162254), and the Program of the Physical Sciences Branch of the Russian Academy of Sciences "Extended Objects in the Universe."

REFERENCES

1. D. Z. Wiebe, A. V. Tutukov, and B. M. Shustov, Astron. Zh. **75**, 3 (1998) [Astron. Rep. **42**, 1 (1998)].
2. C. Firmani and A. Tutukov, Astron. Astrophys. **264**, 37 (1992).
3. C. Firmani and A. Tutukov, Astron. Astrophys. **288**, 713 (1994).
4. D. Wiebe, B. Shustov, and A. Tutukov, Astron. Astrophys. **345**, 93 (1999).

5. D. Z. Wiebe, A. Moiseev, and A. V. Tutukov, Astron. Zh. (in press).
6. B. M. Shustov, *Proc. 34th International Student Science Conference on Physics of the Cosmos* (Ural'skii Univ., Yekaterinburg, 2005), p. 207.
7. R. B. Tully and J. R. Fisher, Astron. Astrophys. **54**, 661 (1977).
8. I. J. Iben and A. Tutukov, Astrophys. J., Suppl. Ser. **54**, 335 (1984).
9. A. V. Tutukov and L. R. Yungel'son, Astron. Zh. **79**, 738 (2002) [Astron. Rep. **46**, 667 (2002)].
10. A. J. Barth, P. Martini, C. H. Nelson, and L. C. Ho, Astrophys. J. **594**, L95 (2003).
11. P. Thorén, B. Edvardsson, and B. Gustafsson, Astron. Astrophys. **425**, 187 (2004).
12. P. E. Nissen, F. Primas, M. Asplund, and D. L. Lambert, Astron. Astrophys. **390**, 235 (2002).
13. G. Israelian, R. Rebolo, R. J. García López, *et al.*, Astrophys. J. **551**, 833 (2001).
14. B. Barbuy, Astron. Astrophys. **191**, 121 (1988).
15. G. Pandey, N. Kameswara Rao, D. L. Lambert, *et al.*, Mon. Not. R. Astron. Soc. **324**, 937 (2001).
16. N. K. Rao, astro-ph/0410648 (2004).
17. M. S. Bessell, N. Christlieb, and B. Gustafsson, Astrophys. J. **612**, L61 (2004).
18. R. Cayrel, E. Depagne, M. Spite, *et al.*, Astron. Astrophys. **416**, 1117 (2004).
19. G. Israelian, N. Shchukina, R. Rebolo, *et al.*, Astron. Astrophys. **419**, 1095 (2004).
20. B. Plez and J. G. Cohen, astro-ph/0501535 (2005).
21. T. Bensby, S. Feltzing, and I. Lundström, Astron. Astrophys. **415**, 155 (2004).
22. I. J. Iben and A. Renzini, Annu. Rev. Astron. Astrophys. **54**, 271 (1983).
23. S. G. Ryan, astro-ph/0211608 (2002).
24. T. Suda, M. Aikawa, and M. Machida, Astrophys. J. **611**, 476 (2004).
25. H. Umeda and K. Nomoto, Astrophys. J. **619**, 427 (2005).
26. A. Maeder, Astron. Astrophys. **264**, 105 (1992).
27. F. Tielemann, K. Nomoto, and M. Hashimoto, Astrophys. J. **460**, 408 (1996).
28. H. Umeda and K. Nomoto, Nature **422**, 871 (2003).
29. P. A. Mazzali, J. Deng, K. Maeda, *et al.*, Astrophys. J. **572**, L61 (2002).
30. A. V. Tutukov, Astron. Astrophys. **70**, 57 (1978).
31. I. V. Igumenshchev, B. M. Shustov, and A. V. Tutukov, Astron. Astrophys. **30**, 524 (1990).
32. A. Aloisi, S. Savaglio, T. M. Heckman, C. G. Hoopes, *et al.*, Astrophys. J. **595**, 760 (2003).
33. T. Yamagata and Y. Yoshii, in *IAU Symposium No. 161: Astronomy from Wide-Field Imaging* (Kluwer, Dordrecht, 1994), p. 420.
34. G. Carraro, Y. K. Ng, and L. Portinari, Mon. Not. R. Astron. Soc. **296**, 1045 (1998).
35. G. Gilmore and R. F. G. Wyse, Astron. J. **90**, 2015 (1985).
36. E. D. Friel, Annu. Rev. Astron. Astrophys. **33**, 381 (1995).
37. C. Du, X. Zhou, J. Ma, J. Shi, *et al.*, Astron. J. **128**, 2265 (2004).
38. Y. C. Liang, F. Hammer, H. Flores, *et al.*, Astron. Astrophys. **423**, 867 (2004).
39. N. Kardashov, A. Tutukov, and A. Fedorova, Astron. Zh. **82**, 157 (2005) [Astron. Rep. **49**, 134 (2005)].
40. A. V. Zasov, D. V. Bizyaev, D. I. Makarov, and N. V. Tyurina, Pis'ma Astron. Zh. **28**, 599 (2002) [Astron. Lett. **28**, 527 (2002)].
41. P. Kroupa and C. M. Boily, Mon. Not. R. Astron. Soc. **336**, 1188 (2002).
42. I. D. Karachentsev and A. M. Kut'kin, astro-ph/0412369 (2004).
43. S. J. Kannappan and E. J. Barton, Astron. J. **127**, 2694 (2004).
44. L. S. Pilyugin, J. M. Vílchez, and T. Contini, Astron. Astrophys. **425**, 849 (2004).
45. D. R. Andersen and M. A. Bershady, Astrophys. J. **599**, L79 (2003).
46. A. Y. Kniazev, E. K. Grebel, S. A. Pustilnik, *et al.*, Astron. J. **127**, 704 (2004).
47. D. Pfenninger and Y. Revaz, in *The Dusty and Molecular Universe: A Prelude to Herschel and ALMA*, Ed. by A. Wilson (ESA, Paris, 2004), p. 63.
48. K. Okoshi and M. Nagashima, astro-ph/0412561 (2004).
49. S. De Rijcke, D. Michielsen, H. Dejonghe, *et al.*, astro-ph/0412553 (2004).
50. C. J. Walcher, R. P. van Marel, D. McLaughlin, H.-W. Rix, *et al.*, astro-ph/0409216 (2004).
51. J. J. Salzer *et al.*, astro-ph/0502202 (2005).
52. A. V. Tutukov, Rev. Mex. Astron. Astrofis., Conf. Ser. **17**, 60 (2003).
53. C. Papovich, M. Dichinson, M. Giavalisco, C. J. Conselice, and H. C. Ferguson, astro-ph/0501088 (2005).
54. I. D. Karachentsev, V. E. Karachentseva, W. K. Huchtmeier, and D. I. Makarov, Astron. J. **127**, 2031 (2004).
55. I. Chiligarian, P. Prugniel, O. Silchenko, and V. Afanasiev, astro-ph/0412293 (2004).
56. M. Fukugita, O. Nakamura, and E. Turner, Astrophys. J. **601**, L127 (2004).
57. W. Keel and K. Borne, Astron. J. **126**, 1257 (2003).
58. C. Nipoti, M. Stiavelli, L. Ciotti, *et al.*, astro-ph/0311424 (2003).
59. J. A. Aguerri and I. Trujillo, Mon. Not. R. Astron. Soc. **333**, 633 (2002).

Translated by L. Yungel'son

Astronomy Reports, Vol. 49, No. 7, 2005, pp. 520–525. Translated from Astronomicheskiĭ Zhurnal, Vol. 82, No. 7, 2005, pp. 584–589.

Numerical Modeling of the Solutions of the Jacobi Equation on a Geodesic with Random Curvature

M. E. Artyushkova and D. D. Sokolov

Moscow State University, Moscow, Russia

Received March 3, 2004; in final form, February 17, 2005

Abstract—We have carried out numerical simulations of solutions of the Jacobi equation on a geodesic with arbitrary curvature, describing the propagation of light in a Universe with inhomogeneities. We used a Runge–Kutta method and a special method involving the multiplication of random matrices. The results are compared with analytical predictions of the asymptotic behavior of a typical realization of this equation and of the behavior of the mean and higher-order statistical moments. © *2005 Pleiades Publishing, Inc.*

1. INTRODUCTION

As early as 1964, Zel'dovich [1] pointed out that the influence of small density inhomogeneities, which are undoubtedly present in the Universe despite its overall exceptional degree of uniformity and isotropy, cannot be reduced to fluctuations of a network of isotropic geodesics and some noise introduced into cosmological tests. It turns out that there arises a small systematic distortion of cosmological tests corresponding to a Universe whose spatial curvature is, on average, equal to zero, so that it resembles to some extent an open cosmological model. The concept of the effective curvature can be introduced [2], and turns out to be negative and proportional to the magnitude of the inhomogeneity. In a Universe with inhomogeneities, an observer measuring the curvature of space by comparing the angular sizes and distances to standard objects will derive the effective curvature, which is negative, instead of the mean curvature, which is zero.

The Zel'dovich effect is little related to the dynamical expansion of the Universe, and is associated with the geometry of space [1]. Moreover, it is associated with the geometry of a two-dimensional slice of space, which is determined by the direction toward an observed object and the object's orientation (for concreteness, we will represent an observed object as a luminous arrow). From a geometrical point of view, the Zel'dovich effect, like other effects associated with cosmological tests, can conveniently be described in terms of Jacobi fields on the spatial geodesics along which a light ray propagates.

Let $\gamma(\theta, x)$ be a family of geodesics passing through some point in space, where x is the distance from the point where they intersect and θ is the angle measured from some basis geodesic, for which $\theta = 0$. The distance between points located at a distance x on nearby geodesics of this family is then equal (within high-order terms in small quantities) to $y(x)\theta$, where y is the Jacobi field along the basis geodesic. The Jacobi field can be found from the Jacobi equation, or the equation for the deviations of the geodesics:

$$y'' + K(x)y = 0, \qquad (1)$$

where K is the curvature of the two-dimensional slice and the derivatives are taken with respect to the distance from the initial point. Density fluctuations lead to curvature fluctuations, so that the Zel'dovich effect is related to the behavior of the solutions of (1) with a random coefficient K.

The study [1] was one of the early works in which unexpected properties of equations with random coefficients were discovered. These situations were subsequently studied primarily in condensed matter physics, where they arise in a number of problems associated with localization (solid-state physics) and intermittency (hydrodynamics) [3]. It is now clear that the solutions of evolutionary equations with random coefficients have many common properties that depend only weakly on the specific form of the equation [4]; we consider these properties in a cosmological context below. Equation (1) is interesting for both cosmology and geometry, but also as a fairly simple model equation in which the behavior of solutions of equations with random coefficients can be studied much more deeply than for the complex equations of condensed-matter physics.

In spite of the considerable analytical progress that has been made with such studies, it is necessary to confirm these results with numerical simulations. First, analytical results usually represent some assertions about the asymptotic behavior of solutions without specifying the time required for the asymptotic behavior to be achieved. Second, many of the

1063-7729/05/4907-0520$26.00

analytical results make full use of models that treat fluctuations like a random field. This type of model has recommended itself well overall, but its adequacy for specific problems in physics is not unlimited [5]; in particular, its limitations in the context of cosmology were pointed out by Zel'dovich [1]. Since the analytical results on the behavior of solutions of the Jacobi equation cardinally disrupt conventional views of statistical physics, their verification via numerical modeling is absolutely necessary. However, there are virtually no such studies in the literature, and it is difficult to apply experience with extensive numerical simulations of turbulence due to their multi-factor nature.

In the current paper, we present results of numerical simulations of the behavior of solutions of the Jacobi equation. These results confirm the qualitative properties of solutions of the Jacobi equation with random coefficients, in particular, the Zel'dovich effect. At the same time, the type of detailed quantitative agreement between the results of the theory and numerical simulations that is sometimes obtained for such comparisons [5] is not achieved.

Of course, a statistical influence on the propagation of light can be exerted not only by cosmological perturbations of the density and curvature, but also by similar perturbations that arise due to the motions of the bodies comprising galaxies. One example is the phenomenon of microlensing (see, for example, [6, 7]), which has implications for the limiting accuracy that can be attained in astrometric measurements [8, 9]. The numerical-simulation results presented below may be of interest in this context as well.

2. NUMERICAL SIMULATIONS

We used natural initial conditions for the numerical simulations of the solutions of (1): $y(0) = 0$ (a light ray emerges from a single point) and $y'(0) = 0$ (the normalization condition).

To correctly construct the desired numerical solution, it is essential to constructively describe the properties of the random process $K(x)$. We based this description on models that are convenient for analytical study (i.e., models with renewal). We divide the basis geodesic into segments of length δ (the correlation length, which we use here as a unit length; the segment itself is usually taken to be the renewal interval). We used random-noise generators to specify in each segment independent constants for the curvature, which are uniformly distributed in the interval $[-K^*, K^*]$. As the analytical results show [2], the solutions of the Jacobi equation for such a random process grow along a geodesic at a rate determined by the quantity $\sqrt{K^*}/\delta \sim \nu$, where ν is the typical deviation angle imparted to the light ray by each inhomogeneity. Roughly speaking, this constitutes the Zel'dovich effect. The smaller K^*, the longer the solution modeling segment interval must be in order to display the growth in which we are interested. On the other hand, the modeling interval cannot be too large because it is not easy to numerically specify a very large number of independent random numbers (see below). Note that we cannot choose $K^* \gg 1/\delta^2$, since the length of a great circle of a sphere is inversely proportional to the square root of its curvature. A choice of ν, and accordingly K^*, based on astrophysical data goes beyond the framework of this study, which is focused on demonstrating the physical phenomenon lying at the basis of the Zel'dovich effect. Therefore, we chose $K^* = 1$, which is close to the limiting value. In reality, the fluctuations of the curvature are appreciably smaller, and the size of the interval of x on which we must carry out the numerical simulations increases proportionally, together with the required set of random numbers.

According to the predictions of the theory, the growth rates γ_p of different higher-order statistical moments $\langle |y|^p \rangle^{1/p}$ differ, since each is determined by the contribution of a different realization of the curvature field. The higher the number of the moment, the more rapid the growth of this moment, so that the growth rate $\bar{\gamma}$ for $\langle y \rangle$ can be analytically calculated, where $\langle \ldots \rangle$ is the sign of the statistical mean. The difficulty in our numerical simulations is that the analytical theory predicts that the Jacobi field grows very nonuniformly (this property is called intermittency). On the one hand, along a typical geodesic, we expect y to grow with some rate γ (the Lyapunov exponent) that is independent of our choice of the basis geodesic. It is difficult to predict the specific value of γ theoretically, and it is of interest to find this quantity numerically. On the other hand, there exist rare basis geodesics on which the Jacobi field grows anomalously rapidly.

Since the intermittency of interest is associated with rare realizations of solutions of the Jacobi equation [3], it was necessary to carry out many realizations in order to estimate the extent to which this phenomenon could be observed in astronomical data. If the angular size of the perturbation is less than $20'$, it is possible to observe 10^6 approximately independent realizations on the celestial sphere. We used random-number generator codes written in Visual C^{++} (version 6.0) and the Maple 5 package; these codes produced a chain of pseudo-random numbers with a repetition period of 2^{32}, which approximately corresponds to the required number of random numbers. To estimate the stability of the results, we compared the results of 10^5 realizations for 100 values of K

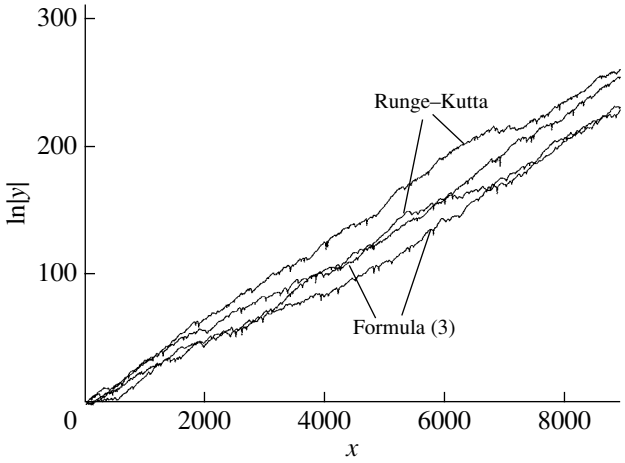

Fig. 1. Typical realizations of $\ln|y|$ constructed using the Runge–Kutta method and formula (3).

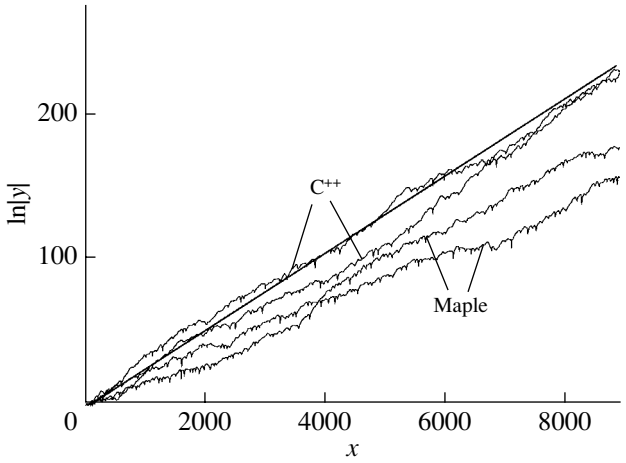

Fig. 2. Typical realizations of $\ln|y|$ constructed using random-number generators written in C^{++} and the Maple package.

obtained in our computations using the two random-number generators.

3. PRODUCT OF INDEPENDENT RANDOM MATRICES

To numerically solve the Jacobi equation for a specified realization of the curvature field, we first used a standard second-order Runge–Kutta method. We also used another approach based on the fact that, in each renewal interval, the solution can easily be expressed in terms of the solution at the left end of the interval and its derivative together with a certain standard transformation matrix that depends only on the curvature in this renewal interval [2]. The solution across several renewal intervals can be expressed as a product of the corresponding random matrices [6]. Using explicit formulas for the transformation matrices, it is possible to compute this product much more rapidly and accurately than can be done with an ordinary Runge–Kutta method.

To obtain this formula, we rewrite (1) as a system of linear equations for the two-component row vector $\mathbf{z}$ with its components $z_1 = y$, $z_2 = \delta y'$:

$$\frac{d\mathbf{z}}{dx} = \mathbf{z}\begin{pmatrix} 0 & -\delta k(x) \\ 1/\delta & 0 \end{pmatrix}, \qquad (2)$$

where y' is multiplied by δ in order to give the components of $\mathbf{z}$ the same dimensions. This equation must be supplemented with the initial condition $z_1(0) = 0$, $z_2(0) = \delta$.

We then have

$$\mathbf{z}(x_{n+1}) = \mathbf{z}(x_n)B_n = \ldots = \mathbf{z_0}B_nB_{n-1}\ldots B_1, \quad (3)$$
$$\mathbf{z}(0) = \mathbf{z_0}.$$

4. RESULTS OF THE NUMERICAL SIMULATIONS

4.1. A Typical Realization

We first compared the results of our numerical simulations of solutions of the Jacobi equation using the Runge–Kutta method with those obtained via a multiplication of appropriate random matrices. We set $\delta = 10$ and reproduced two realizations for each method up to values $x = 10\,000$. These results are presented in Fig. 1, which shows that, in accordance with the analytical predictions, $\ln|y|$ grows nearly linearly, beginning already from 50 renewal points. Since $y = 0$ at the initial point due to the boundary condition, the curves are shown beginning from $x = 150$. All four random sequences were obtained using the C^{++} random-number generator. We can see in this figure that both of the curves constructed using the Runge–Kutta method lie systematically over the two curves constructed by multiplying random matrices. This seems to indicate that the Runge–Kutta method introduces an additional artificial instability in the solution of the Jacobi equation, compared to the multiplication of random matrices, which uses special properties of the equation being considered. Further, we used the method of multiplying random matrices to estimate the accuracy of the results based on the convergence of the results obtained for different realizations.

Let us now compare the solutions of the Jacobi equation obtained for the random sequences obtained using the C^{++} and Maple random-number generators. Figure 2 presents two realizations for each of these generators. We can see that, as in Fig. 1, the solutions grow exponentially beginning from small values of x. We calculated the growth rate γ (Lyapunov

Table 1. Growth rates of typical realizations for the C^{++} and Maple random-number generators

Generator	γ					$\langle\gamma\rangle$	$\Delta\gamma$
C^{++}	0.0225	0.0235	0.0240	0.0246	0.0254	0.0245	0.001
Maple	0.0180	0.0181	0.0190	0.0189	0.0179	0.0183	0.002

exponent) of each of the realizations as the tangent of the slope of the straight line approximating this plot (one such line is shown in the figure). We emphasize that the analytical predictions refer to the slope above the x axis, but not the points of intersection of the line with the coordinate axes. The numerical results of our comparative analysis of the random-noise generators are presented in Table 1. Here, γ is the growth rate of a typical realization, $\langle\gamma\rangle$ is the mean growth rate for five realizations, and $\Delta\gamma$ is the rms deviation.

We can see that the scatter of the γ values for realizations obtained using a single random-number generator is lower than the scatter for the growth rates for different realizations obtained using both generators. In turn, the difference between the growth rates obtained using the two different generators is approximately equal to the difference in the growth rates for the solutions obtained using the Runge–Kutta and matrix-multiplication methods. At the same time, in all cases, these differences in the estimates of γ are smaller than the typical value of γ, demonstrating that the instability considered is not an artefact of a numerical realization.

Note that all the curves in Figs. 1 and 2 contain a shallow ripple. This arises because, from time to time, the vector **z** in the corresponding two-dimensional space turns such that its first component vanishes. In geometrical terms, this means that a conjugate point arises on the geodesic; from the point of view of general relativity, this denotes the appearance of a gravitational lens that is associated not with some individual perturbation of the curvature, but with the joint action of many perturbations. Since we chose a dispersion for the curvature that is close to the limiting possible value, our model appreciably overestimates the number of conjugate points compared to the situation in the real Universe. Numerical modeling of the distribution of conjugate points goes beyond the framework of this study.

4.2. Mean and Higher-Order Statistical Moments

We will now turn to verifying the theoretical prediction that the statistical moments of the Jacobi field grow more rapidly than a typical realization, and that the rate of this growth is higher the higher the number of the moment. For this purpose, we obtained solutions of the Jacobi equation for 5×10^5 realizations of the random curvature field obtained using the C^{++} random-number generator. We used these solutions to construct the mean and two subsequent statistical moments, whose behavior along the geodesic is shown in Fig. 3, together with the behavior of a typical realization for comparison. We can see that the statistical moments grow exponentially with time, and that the growth rate increases with the moment number. On the scales considered, the exponential growth of a typical realization has not yet begun. Note that the growth of the statistical moments slows with time, with the point at which the deceleration starts, h_p, being closer to the coordinate origin the higher the moment number. This deceleration is due to the fact that, although our sample is large, it is not infinite. According to the analytical results, to sustain the exponential growth of the moments along the entire geodesic, the volume of the sample must grow exponentially with distance from the origin. Modeling the behavior of moments with numbers higher than three would require an excessively large number of realizations.

We also compared the results for the mean solution obtained using the C^{++} and Maple random-number generators. Figure 4 shows the mean values $\ln\langle|y|\rangle$ for 10^5 realizations for the two generators. The two growth rates do not coincide, but the difference

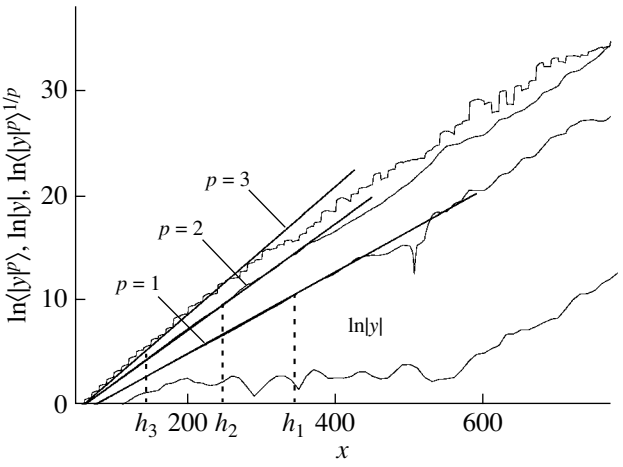

Fig. 3. Typical realization of $\ln|y|$, the mean value $\ln\langle|y|\rangle$, and the moments $\ln\langle|y|^p\rangle^{1/p}$ $(p = 2, 3)$ constructed for 5×10^5 realizations.

Table 2. Growth rate of statistical moments of the sample size N

N	Deceleration point						Growth rate					
	h_1	h_2	h_3	h'_1	h'_2	h'_3	γ_1	γ_2	γ_3	γ'_1	γ'_2	γ'_3
10^5	259	156	149	278	179	137	0.0370	0.0505	0.0605	0.395	0.0516	0.0611
5×10^5	338	234	120	355	228	134	0.0380	0.0503	0.0584	0.396	0.0519	0.0625
10^6	344	233	172	446	250	190	0.0381	0.0501	0.0559	0.0393	0.0506	0.04629

between them is much smaller than for the typical realizations in Fig. 2. Thus, the results obtained for the two random-number generators approach each other after a large number of typical realizations are averaged.

Overall, the results of the numerical simulations coincide with the predictions of the analytical treatment, at least qualitatively. Quantitative data on the characteristics of the growth of the moments are given in Table 2, where h_p ($p = 1 \ldots 3$) is the point where the deceleration in the growth begins and γ_p is the growth rate for the pth moment. When obtaining the data in this table, we also verified the stability of the results against changes in the volume of the sample, N.

4.3. Mean Jacobi Field

One characteristic result of the analytical treatment of the Jacobi field is the expectation that, not only should the mean modulus of the Jacobi field grow, but also the mean of the Jacobi field itself. The nontriviality of this assertion is that the sign of the Jacobi field changes at the conjugate points that arise sooner or later on each geodesic, so that the contributions of various realizations to $\langle y \rangle$ begin to subtract rather than add. The behavior of $\langle y \rangle$ undoubtedly differs from the behavior of $\langle |y| \rangle$, and, nevertheless, intermittency also occurs in the absence of a modulus for $\langle y \rangle$.

The behavior of the mean values $\langle y^p \rangle$ ($p = 1 \ldots 3$) for 5×10^5 is shown in Fig. 5, which resembles Fig. 3. The exponential growth of the moments $\langle y^p \rangle$, like the growth in the moments $\langle |y^p| \rangle$, continues only in a finite interval of x. Table 2 presents the points where the deceleration in the growth h'_p and the growth rate γ'_p begins, calculated as the tangents of the slopes of tangent lines at the deceleration points h'_p of the moments $\langle y^p \rangle$ for various sample volumes N.

Analytical studies of the growth of the mean Jacobi field yield $\gamma_1 \approx 0.0288$ [2], while we obtained $\gamma_1 \approx 0.0377$. This difference is probably associated with errors introduced by the random-noise generators.

ACKNOWLEDGMENTS

This work was supported by the Russian Foundation for Basic Research (project no. 04-02-16094). The authors thank M.V. Sazhin for useful discussions.

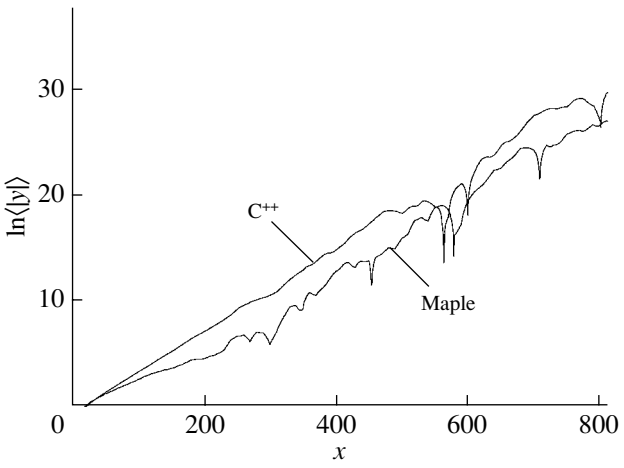

Fig. 4. Mean values $\ln\langle |y| \rangle$ for 10^5 realizations constructed using the C^{++} and Maple random-number generators.

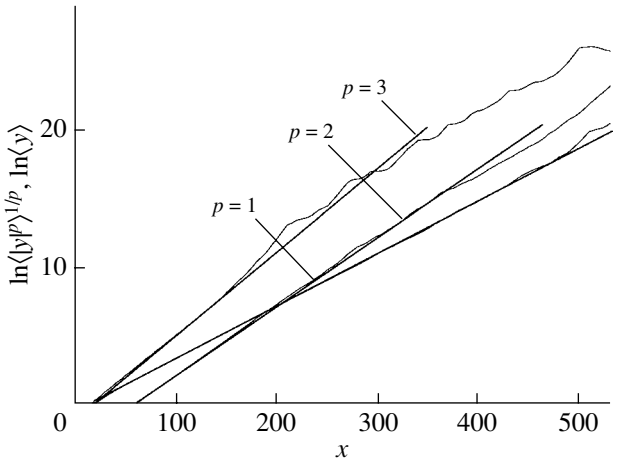

Fig. 5. Mean $\ln\langle y \rangle$ and the moments $\ln\langle y^p \rangle^{1/p}$ ($p = 2, 3$) constructed for 10^5 realizations.

REFERENCES

1. Ya. B. Zel'dovich, Astron. Zh. **41**, 19 (1964) [Sov. Astron. **8**, 13 (1964)].
2. V. G. Lamburt, D. D. Sokolov, and V. N. Tutubalin, Mat. Zametki **74** (3), 416 (2003).
3. Ya. B. Zel'dovich, S. A. Molchanov, A. A. Ruzmaikin, *et al.*, Usp. Fiz. Nauk **152**, 3 (1987) [Sov. Phys. Usp. **30**, 353 (1987)].
4. Ya. B. Zeldovich, A. A. Ruzmaikin, and D. D. Sokolov, *The Almightly Chance* (World Sci., Singapore, 1991).
5. V. N. Tutubalin, *Probability Theory and Random Processes* (Mosk. Gos. Univ., Moscow, 1992) [in Russian].
6. M. V. Sazhin, V. E. Zharov, and T. A. Kalinina, Mon. Not. R. Astron. Soc. **323**, 952 (2001).
7. M. V. Sazhin, V. E. Zharov, A. V. Volyankin, and T. A. Kalinina, Mon. Not. R. Astron. Soc. **300**, 287 (1998).
8. I. A. Trifalenkov, M. V. Sazhin, and A. M. Cherepashchuk, Astron. Rep. **40**, 458 (1996).
9. V. E. Zharov, M. V. Sazhin, and N. A. Chuikova, Astron. Rep. **44**, 122 (2000).
10. F. R. Gantmakher, *The Theory of Matrices* (Nauka, Moscow, 1967; Chelsea, New York, 1959).

Translated by D. Gabuzda

Astronomy Reports, Vol. 49, No. 7, 2005, pp. 526–534. Translated from Astronomicheskiĭ Zhurnal, Vol. 82, No. 7, 2005, pp. 590–600.

Variability of Stars in the Pulkovo Spectrophotometric Catalog

A. A. Arkharov, E. I. Hagen-Thorn, and E. V. Ruban

Main (Pulkovo) Astronomical Observatory, Pulkovskoe sh. 65, St. Petersburg, 196140 Russia

Received April 26, 2004; in final form, February 17, 2005

Abstract—We present the results of a statistical study of brightness variability for 693 stars of the Pulkovo spectrophotometric database in five spectral bands in the range $\lambda\lambda$ 320–1080 nm. Significant brightness variations were detected in at least one spectral band against the background of the random noise for one-third of the stars not earlier believed to be variable. A comparison of the distributions of these variations in amplitude and spectral band for the normal and variable stars shows that variability is inherent to most stars to some extent and is often wavelength dependent. © *2005 Pleiades Publishing, Inc.*

1. INTRODUCTION

Photoelectric stellar spectrophotometry has been carried out at the Main (Pulkovo) Astronomical Observatory of the Russian Academy of Sciences for more than two decades. The first large-scale observations were started during a joint expedition of the Main Astronomical Observatory and the Crimean Astrophysical Observatory to Chile in the early 1970s [1, 2]. This work was then continued in the Pamirs, Armenia, and Bolivia. Observations with the AZT-7 and Zeiss-600 telescopes were made in the visual (320–737.5 nm) and near-infrared (500–1080 nm).

The observations from different seasons were reduced independently using the techniques of absolute spectrophotometry, with separate determinations of the atmospheric extinction coefficients and the spectral response of the instruments. Finally, the data were presented in the form $m(\lambda) = -2.5 \log E(\lambda)$, where $E(\lambda)$ represents the quasi-monochromatic flux from the star at the outer boundary of the Earth's atmosphere in erg cm^{-2} s^{-1} cm^{-1} averaged over the season. These values were included in the corresponding (seasonal) catalog along with their rms deviations $S(\lambda)$, with a wavelength increment of 2.5 nm. This yielded a large spectrophotometric database comprised of the individual seasonal catalogs, which can be used for various studies of stellar physics.

The data correspond to series of observations of stars during various periods, and cover a long time interval. Therefore, one obvious study is to search for brightness variability. This is an important goal, as variability has recently been discovered for many stars in our database that were believed earlier to be non-variable. The absence of results for certain individual observations does not exclude variability studies. Our data are abundant and sufficiently accurate [3] to enable statistical analyses, making it possible to detect real brightness variations of the catalog stars.

2. CHARACTERISTICS OF THE DATABASE

The total number of stars in all our catalogs is 693. For these stars, 1510 spectral energy distributions are available, which are the result of averaging 12 932 individual observations for individual seasons. There are a total of 21 seasonal catalogs: 9 for the visual and 12 for the infrared. The number of stars in the catalogs varies from 8 to 425 (in the catalog for the Chilean expedition [1]), comprising, on average, about 60–70 stars. More than half of all the stars (367) are present in only one catalog; these are mainly southern stars contained in the Chilean catalog that are not observable from the northern hemisphere. Most of the remaining stars are present in two to six catalogs (17 catalogs at most). On average, a series of observations of a given star during one season comprises 5–10 individual observations, with the mean number of observations of one star during all seasons being 8–20. These numbers are much higher for stars selected as standards and extinction calibrators.

The database presented here was fundamental for the compilation of the Pulkovo Spectrophotometric Catalog (PSC) [4, 5], which combines observations for all the seasons. The catalog contains 608 bright stars of various spectral types from O to M, as a rule, with magnitudes $V < 5^m$. Estimates of the internal and external consistency demonstrate the high accuracy of the PSC data [6]. The rms uncertainty for the magnitudes averaged for all observations of a star is about 1.5%. In the central part of the spectral range covered (500–740 nm), the uncertainties for more than half of the catalog's stars are within 1%. These become larger towards the ends of the

1063-7729/05/4907-0526$26.00

range: to 5–7% in the ultraviolet and to 3–5% in the infrared. Estimates of the external accuracy of the PSC data were derived via comparisons with several spectrophotometric catalogs containing detailed stellar spectral energy distributions [7–11] and the 13-band photometry of Johnson and Mitchel [12]. The systematic deviations are within the errors in the absolute spectrophotometry, and are about 3% for smooth parts of the spectra and increase to 5–7% in lines and bands, reaching 10% near the Balmer jump. These accuracy estimates for the PSC reflect the uniformity and reliability of the original observations.

The structure of the database can be used to identify variability in two ways: by comparing data for the seasonal catalogs averaged over the observing periods or by analyzing the scatter of data within a given observing season. For both techniques, the dispersion of the observational data and the corresponding rms (standard) error, which we, for brevity, will call the observational error, is an important quantity for statistical analyses. The observational errors have been analyzed in a number of papers [1, 3, 6, 13]. Here, we consider some of the conclusions following from these analyses.

3. OBSERVATIONAL SPECTROPHOTOMETRIC ERRORS

The observational errors depend on various factors associated with the observing conditions, as well as the individual properties of stars. A fairly large number of variables appear to be present among the stars in the database, which we subdivide into three groups: known variables (V), suspected variables (VN), and "normal" stars, for there is no prior evidence of variability (N). Information on the known variables was taken from the variable-star catalog [14]. We studied each of these groups of stars separately.

The spectrophotometric observational errors are different for different spectral ranges. A curve describing the wavelength dependence of the rms error of a single observation, averaged for all the program stars, was derived in [3]. This curve shows that the observational errors increase considerably for steep parts of stellar spectra (spectral lines and bands, the Balmer jump). This is apparently due to uncertainties in the wavelength fits. Problems in correcting for atmospheric extinction increase the errors in telluric bands and in the ultraviolet, where the atmosphere's transparency drops rapidly. The errors also increase towards the ends of the observed spectral ranges, due to the decreased instrumental sensitivity.

We carried out our statistical analysis in several spectral intervals in which the error levels were approximately the same. The data for all the seasonal catalogs were averaged in five spectral intervals: 320–370, 410–507.5, 510–737.5, 740–900, and 902.5–1080 nm, which we will designate using their central wavelengths (345, 459, 624, 820, and 991 nm), with the region of the Balmer jump excluded from consideration [15–17]. The averaged data were analyzed separately for each of the spectral intervals.

Even if the instruments and techniques used are the same, the observing conditions can differ from season to season. A preliminary comparison of several mean characteristics calculated using data from the seasonal catalogs revealed some systematic deviations for the mean monochromatic magnitudes and their standard errors [3]. These deviations can be significant for individual intervals and also for the spectrum as a whole. The observational errors are crucial when searching for low-amplitude brightness variability, and are increased by systematic seasonal deviations; therefore, we analyzed the errors for each observing period separately. In this case, a star's variability is studied only within a single observing season, imposing limitations on the time scale of the variability that can be detected.

The scatter of the data within a single observing season also depends on several factors, most importantly atmospheric and instrumental effects. The former influence the observations most strongly at large air masses. However, as a rule, the program stars were never observed at elevations corresponding to more than two air masses, so that the influence of atmospheric factors was insignificant. This is confirmed by the fact that the observational errors are independent of declination, as is verified in [13].

Instrumental errors are related to the detector sensitivity, and depend on the level of the photometric signal. In fact, the study described in [13] demonstrated that the relations between the observational errors averaged within spectral intervals and the corresponding magnitudes displayed certain similar trends for all the seasonal catalogs. For all the stars, the mean errors are practically constant for relatively high brightness levels ($m < 6^m$) and increase appreciably at lower brightness levels ($m > 7^m$). Some catalogs show an increase in the error level for the brightest stars ($m < 1^m$), due to the nonlinear sensitivity of the detectors in the presence of strong signals. This is observed in all spectral ranges, and is most pronounced in peripheral spectral intervals. It follows that, when analyzing the observational errors, we must take into account their dependence on the apparent magnitude, individually for each seasonal catalog and for each spectral interval.

4. SEARCH FOR BRIGHTNESS VARIABILITY WITHIN OBSERVING SEASONS

To detect variability in the presence of the observational errors of the seasonal data, we applied a

dispersion analysis technique aimed at separating the observational dispersion into components due to various factors and estimating the relative importances of the individual factors.

In the absence of pointing or systematic errors, the dispersion of a star's observations, S^2, is the sum of the dispersion due to the random scatter of the observed magnitudes, S_0^2, and the dispersion due to real variability, S_v^2. These contributions can be considered to be independent, since the dependence of S_0^2 on variations in the magnitude, m, is insignificant for low-amplitude variability, being manifest, as is indicated above, only when $m > 6^m$. We then have

$$S^2 = S_0^2 + S_v^2,$$

where S, S_0, and S_v are the corresponding standard errors.

Thus, to derive a star's brightness variations and estimate their significance in the presence of random errors, we must know the random error for the corresponding seasonal catalog, S_0, in each of the spectral intervals.

Our approach to isolating the random component in the observational error is based on the idea that, after eliminating all factors apart from the random scatter, the observations should display a normal distribution. The corresponding initial dispersion describes the accuracy of the observing technique.

Thus, the random errors should be approximately the same for most stars of a given magnitude. Consequently, the dispersions of the observational series for stars that are not influenced by nonrandom factors should not differ significantly at a specified probability level, and should each represent sample estimates of the same parent dispersion. We can use a collection of such errors to determine the sample mean standard deviation, S_0, which describes the random scatter of a specified seasonal catalog in a specified spectral interval. We used stars in all the variability groups for this study, since they should have the same characteristic random errors. The random scatter could be slightly higher for the variable stars, due to the presence of small brightness variations.

Because it is difficult to approximate $S(m)$ with a single curve for all m values, the magnitude range was subdivided into intervals, within which the form of this relation can be considered constant. We analyzed the errors separately for each of these intervals. We used an iterative procedure to obtain the most accurate and reliable estimates of the dispersions of the random components.

We adopted as a first approximation the minimum observational error: $S_0 = S_{\min}$. This value was compared to the closest value of another star's observational error using the Fisher ratio test with the probability level $p = 95\%$. In the case of nearly coincident dispersions, we assigned a new S_0 value equal to their weighted mean. We repeated this procedure in order of increasing errors for all the catalog's stars in a given magnitude range.

This approach enabled us to select stars whose standard errors did not differ significantly, and could be considered good estimates of the dispersion of the random component. These stars were then used to derive the final weighted mean error for the magnitude range considered:

$$S_0^2 = \frac{1}{n - l_0} \sum_{j=1}^{l_0} (n_j - 1) S_j^2,$$

where S_j, n_j are the standard error and the number of observations for the jth selected star, and l_0 is the number of stars selected, $n = \sum_{j=1}^{l_0} n_j$. The higher the number of degrees of freedom,

$$f_0 = \sum_{j=1}^{l_0} (n_j - 1) = n - l_0,$$

the more reliable the estimate of the random dispersion.

When it was necessary to take into account the $S_0(m)$ relation within some magnitude range, we obtained least-squares regression lines or first- or second-order curves for this relation using the errors, S_j, and their corresponding magnitudes, m_j. Combining intervals of the curves for individual ranges of m yields a master $S_0(m)$ curve for the corresponding catalog. This procedure is described in detail in [13].

Using the resulting curves for each of the seasonal catalogs, we can select stars whose observational errors exceed the random errors for their magnitudes, indicating that their brightness shows significant variations in a given spectral interval. When the difference between the star's dispersion, S_j^2, and the dispersion for its magnitude m_j, $S_0^2(m_j)$, is significant according to the Fisher ratio test, we can estimate the star's brightness variations. For this purpose, we applied the approximate formula

$$S_{vj}^2 = S_j^2 - S_0^2(m_j),$$

which describes the dispersion due to the variability and the corresponding standard error, S_{vj}.

5. SEARCH FOR BRIGHTNESS VARIABILITY BETWEEN OBSERVING SEASONS

Let us now turn to longer-term stellar brightness variations over several observing seasons. Consider the scatter of a star's seasonal mean magnitudes corresponding to data from different seasonal catalogs.

A comparison reveals some deviations, which can be considerable. The question we wish to ask is whether these deviations are significant, given the presence of certain random errors. Another important question is whether there exist any patterns related to particular observing seasons, in other words, whether the deviations are systematic.

Though the observations used similar instruments and the same observing and reduction techniques, strictly speaking, the resulting catalogs are not uniform. This means that analysis of a star's season-to-season brightness variations may indicate deviations due to nonuniform data rather than genuine brightness variability. Such nonuniformities were studied in [3], and systematic corrections, $\Delta m_i(\lambda)$, were derived for the ith seasonal catalog. These were calculated by averaging, for all stars, the deviations of the data in the corresponding catalog from the PSC data. Note that the magnitude in the PSC is a weighted mean of the data in all catalogs containing the star.

As a rule, the systematic error is small—less than the random error in most cases. However, the systematic error must be taken into account, because it can be significant in searches for low-amplitude variability. For this reason, the corrections $\Delta m_i(\lambda)$, averaged over λ in the five wavelength intervals considered, were applied to the corresponding original data. The corrected magnitudes provided the starting data for our subsequent analyses. The scatter of these magnitudes in different seasonal catalogs may now reflect real variations of stellar brightness, and we can estimate the significance of these variations in the presence of random scatter using statistical methods.

Variability can not only change the seasonal mean flux of a star, but also the observed dispersion, so that it will differ from the random-scatter dispersion. Based on the dispersion analysis discussed above, we derived sample mean standards for each seasonal catalog, describing the scatter of the observations for all the catalog stars, and their dependence on the observed magnitude, $S_0(m)$. We can then determine, for each star in our database, the random observational error corresponding to its magnitude for each of the seasons and in each of the five spectral intervals.

Thus, we have a collection of k sets of values for each star in each wavelength interval: $\{m_i,\ n_i,\ S_i(m_i)\}$. Here, k is the number of catalogs (observing seasons) containing the star, m_i is the magnitude in the ith ($i = 1, \ldots, k$) catalog, averaged over the observing season and corrected for systematic errors, n_i is the number of observations of the star during the season (the length of the series), and $S_i(m_i)$ is the random observational error. We can compare the mean values in several samples using various techniques. Our statistical analysis is described in detail in [18]. Here, we only list the tests used and describe their most important features.

The most obvious way to detect variability is to compare the minimum, $m_{\min}$, and the maximum, $m_{\max}$, values in the set of magnitudes, m_i. The most accurate and reliable estimates of the significance of deviations of the mean values for two magnitude samples can be obtained when the corresponding parent dispersions, σ^2, are known. However, the number of stars used to derive the $S_i^2 = S_0^2$ values (to simplify our notation, we drop the dependence on m) is not always high enough to regard S_i^2 as the parent dispersion. For small samples, we must use a Student rather than a normal distribution. However, in this case, accurate estimates are possible only when the dispersions coincide; i.e., when the S_i^2 values for the compared catalogs differ insignificantly. In the general case of differing dispersions, we must apply approximate criteria.

We compared a star's maximum and minimum brightness by applying the following, most widely used and convenient, technique for comparing two sample means, which is described by Pustylnik [19].

We calculate the value

$$T = \frac{V_{\min} t_{1-p/2}(f_{\min}) + V_{\max} t_{1-p/2}(f_{\max})}{\sqrt{V_{\min} + V_{\max}}},$$

where $V_{\min} = \dfrac{S_{\min}^2}{n_{\min}}$, $V_{\max} = \dfrac{S_{\max}^2}{n_{\max}}$, $f_{\min} = n_{\min} - 1$, $f_{\max} = n_{\max} - 1$, $t_{1-p/2}(f)$ is the Student distribution for the corresponding number of degrees of freedom and the significance level p, and $S_{\min}$, $S_{\max}$, $n_{\min}$, and $n_{\max}$ are the random errors for the magnitudes $m_{\min}$ and $m_{\max}$ and the number of observations used to derive them. The difference between the magnitudes is significant if $|m_{\max} - m_{\min}| > T$.

The comparison of a star's maximum and minimum brightnesses in the seasonal catalogs enables us to judge whether the brightness is variable, at least between the corresponding observing seasons. However, we obtain no information about variability for other series of observations. Even if there is no significant difference between the maximum and minimum values, we can be sure that the differences for all intermediate values are likewise not significant only if the corresponding samples have the same volume, $n_1 = n_2 = \ldots = n_k$.

We can obtain more trustworthy estimates by simultaneously comparing several mean values, if the dispersions for the samples are all equal. The weighted mean dispersion can then be used as an estimate of the parent dispersion, σ^2, and the total weighted mean value as an estimate of the unified parent mean. Another σ^2 estimate can be obtained

from the scatter of the mean values among the samples. A comparison of these results using the Fisher ratio test can be used to estimate the significance of the differences between the sample mean values.

When the dispersions of the compared samples are different, it is convenient to use an equalizing test [20]. Here, the existing set of mean values for several observational series is treated as a series of measurements with unequal but known uncertainties. Using weights inversely proportional to the squared errors, we can equalize the sample parameters and compare the resulting dispersion to the mean dispersion weighted using the initial uncertainties. If the two dispersions are different, this indicates the presence of deviations that exceed the natural scatter.

In addition to the above tests, we can also estimate the significance of differences between results for individual observing series and the overall mean based on the S_i^2 dispersions, applying a Student distribution.

We used all these techniques to estimate the deviations of the data in the seasonal catalogs, applying each whenever possible and taking into account the imposed restrictions. We tested for the equality of the dispersions of the series of observations using the test of Bartlet [19], for which sufficiently large series of observations are needed: $n_i > 5$. This limits the use of the Fisher test for equal sample dispersions, because this condition is met by only 30% of our data. All our estimates were based on a probability level of 95%.

6. ANALYSIS OF THE RESULTS

The above techniques were applied to all the stars in our spectrophotometric database in all five selected spectral intervals, separately for the variability groups N, VN, and V defined in [15–17].

It is especially interesting to search for variability among the normal (N) stars. These are stars whose brightness was earlier believed to be constant, and whose spectra show no features due to factors other than their temperature (rotation, a strong magnetic field, unusual chemical abundances, etc.). In addition, these should display low reddening, with color excesses $<0.1^m$, and with normal color distributions (according to Straizys).

Significant brightness variations within a season, S_v, were demonstrated by 52 of the analyzed 172 stars, or about 30%. For most stars, significant S_v values were found for a single season only, and only for seven stars was significant variability found for several seasons. The lowest significant value of S_v we found is 0.02^m, and the highest 0.17^m. We do not discuss the possible origins of the variability here, but note that the 30% of stars whose brightness variations have been detected are not double stars or spectroscopic binaries.

Significant S_v values were found for less than 50% of the variable stars (VN and V), and not for every observing season. Brightness variability within an observing season was demonstrated by 62 stars of 134 variables with known types and 76 of 176 suspected variables. Note, however, that many suspected variables demonstrated brightness variations exceeding the photometrically-determined ΔV values in some of the spectral intervals. The lowest significant S_v we find is 0.02^m, as for the normal stars. A detailed analysis of the detected brightness variations for different types of variables is presented in [21]. If we restrict our consideration to low-amplitude variations, S_v ($<0.1^m$), the fraction of detected stars showing real variations within an observing season is the same for the normal and variable stars, ~30%.

We searched for season-to-season brightness variations for each wavelength interval for all the stars contained in several seasonal catalogs. Naturally, this condition is satisfied not by all stars, and the number of stars for which it is satisfied is different for different spectral intervals. Brightness variability in several seasonal catalogs was demonstrated by 25 of 69 normal stars, 61 of 111 stars suspected variables, and 39 of 65 known variables. More than half of the detected variations for stars in any group are within 0.1^m, but we also encounter stronger variations, including among the normal stars.

The identified cases of variability were compared with the data in the Hipparcos catalog [22]. Variability is noted in [22] for 36% of the normal stars that demonstrated brightness variations according to our analysis. The corresponding fractions for the other groups are 51% (VN) and 88% (V).

We present the results of our variability searches for the normal stars (N, Table 1) and the variables of unknown types or suspected variables (VN, Table 2). These tables combine the results of our searches for variability within observing seasons [13, 21] and between seasons [18]. They contain the highest values of the single-season variations, S_v, for the wavelength intervals. The interseason variations are presented as the differences Δm between the maximum and minimum mean magnitudes derived for different seasons, with their significance confirmed simultaneously by several tests.

The tables present data for the stars whose brightness variability can be taken to be real. These stars showed significant brightness variations in several spectral intervals. An exception is the interval where the observed ranges intersect (624), where we combine all the data available for a star, so that the chances to detect variability are the highest. Detailed

Table 1. Brightness variations for the normal group (N)

BS	V^m	Sp	Db	k		n		345 nm		459 nm		624 nm		820 nm		991 nm	
				vi	ir	vi	ir	S_v	Δm	S_v	Δm	S_v	Δm	S_v	Δm	S_v	Δm
165	3.27	K3III	D	2	2	18	9	–	–	0.07	–	0.06	–	–	–	–	–
285	4.25	K2II-III	–	2	2	13	11	–	–	–	–	–	0.04	–	–	–	0.08
402	3.60	K0IIIb	D	2	2	8	8	–	–	–	–	–	0.05	–	–	–	–
804	3.47	A3V	D	2	3	128	18	0.11	–	0.11	–	0.10	–	–	–	–	0.08
1208*	3.24	M2III		1	1	5	7	–		0.06		0.04	0.07	–		–	
1931*	3.81	O9.5V	D	2	1	10	3	–	–	–	0.05	–	0.07	–		–	
2618*	1.50	B2II	D	1	2	4	12	–		–		0.02	0.04	0.03	0.05	–	–
2878*	3.25	K5III	D	1	1	4	16	–		–		0.03	0.07	–		-	
3165*	2.25	O5Iaf	–	1	1	54	17	0.07		0.05		0.06	–	0.06		–	
4232	3.11	K2III	–	2	3	10	15	0.07	0.25	0.06	0.09	–	0.06	–	–	–	–
4335	3.01	K1III	–	2	3	10	18	–	–	–	–	0.17	0.12	0.15	0.10	0.17	0.12
5190*	3.41	B2IV	SB	1	0	4	0	0.05		0.03		–					
5235*	2.68	G0IV	D	1	5	10	87	0.05		0.04		0.05	0.10	0.03	0.06	0.03	0.05
5264	4.26	A3V	D	1	0	21	0	0.05		0.04		–					
5708*	3.37	B2IV-V	D	1	0	4	0	0.07		0.10		0.06					
6378*	2.43	A2V	D	2	2	13	14	–	–	–	–	0.05	0.05	0.04	0.04	0.07	–
6396*	3.17	B6III	–	3	2	12	19	–	–	–	–	–	0.04	–	–	–	–
6566	5.05	K0III	D	1	1	4	3	–		–		–	0.05	–		–	
6629	3.75	A0V	–	2	2	15	8	–	0.05	–	0.03	–	0.06	–	0.04	–	0.06
6743*	3.66	B2Ib	–	1	0	125	0	0.05		0.04		0.05					
6879	1.85	B9.5III	D	1	1	220	6	0.05		0.04		0.03	–	–		–	
7121*	2.02	B2.5V	D	7	7	113	66	0.05	0.08	0.05	0.04	0.06	0.16	0.05	0.12	0.07	0.10
7304	4.96	G8II	D	1	1	3	4	–		–		–	0.06	–		–	
7310	3.07	G9III	D	2	3	12	32	–	–	–	–	–	–	–	0.07	–	0.05
7710	3.23	B9.5III	D	1	1	5	18	–		–		–	–	0.05		0.12	
7882*	3.63	F5IV	D	2	0	11	0	–	0.06	–	0.05	–	–				
8254	3.76	K0III	D	1	0	9	0	0.14		0.05		0.05					
8353	3.01	B8III	–	1	0	7	0	0.05		0.07		0.07					
8414	2.96	G2Ib	D	3	3	33	25	0.04	–	–	–	–	0.08	–	–	–	–
8728	1.16	A3V	D	7	7	313	136	0.05	0.08	0.06	0.03	0.05	0.07	0.04	–	0.05	0.05

results of our analysis, along with a complete list of the stars showing significant brightness variations in at least one of the intervals, are given in the papers cited above.

The columns of the tables present the star numbers in the BS catalog, with asterisks denoting stars for which variability information is available in the Hipparcos catalog [22]; the visual magnitudes (V^m, Table 1) or their ranges (ΔV^m, Table 2) from [17]; a star's spectral type, with more detailed information for some stars given in the footnotes; a code indicating stars that are doubles (D) or spectro-

Table 2. Brightness variations for the suspected variables (VN)

BS	V^m	Sp	Db	k		n		345 nm		459 nm		624 nm		820 nm		991 nm	
				vi	ir	vi	ir	S_v	Δm	S_v	Δm	S_v	Δm	S_v	Δm	S_v	Δm
98	0.06	G2IV	–	1	1	4	5	0.05				0.05		0.05	–	–	–
188*	0.15	K0III [1]	–	3	2	12	10	0.07	0.11	0.05	0.04	0.05	0.04	–	–	–	–
337*	0.09	M0IIIa	D	3	6	31	403	–	–	0.05	–	–	0.04	–	0.07	–	0.08
553	0.14	A5V	SB	2	6	20	25	–	–	0.03	–	–	–	0.04	–	0.07	–
617	0.06	K2IIIab	–	1	1	7	10	0.13		0.12		0.10	0.05	–		–	
1017*	0.14	F5Ib	D	1	4	19	31	–		–		0.03	0.03	0.02	0.04	–	–
1088		B8V [1]	SB	1	1	7	6	0.04		–		0.04	0.04	–		–	
1203*	0.13	B1Ib	D	3	2	17	11	0.19	0.18	0.19	0.11	0.20	–	–	0.17	–	0.03
1347*		B9V	D	1	0	11	0	0.05		0.07		0.07					
1577	0.15	K3II	–	1	3	6	22	–		–		0.03	–	–	0.03	–	0.04
1666	0.08	A3III	D	3	2	17	10	0.08	0.09	0.03	–	–	–	–	–	–	–
1713*	0.27	B8Iae?	D	1	5	7	27	0.05		0.06		0.06	0.11	0.10	0.07	0.08	0.14
1790*	0.05	B2III	D	4	4	17	22	–	–	0.04	0.10	–	0.09	–	0.05	–	0.08
1865*	0.06	F0Ib	D	2	1	8	7	–	–	–	–	–	–	0.03		0.04	
2004*	0.08	B0.5Iav	–	4	2	13	8	0.05	0.41	0.04	0.16	0.03	0.14	–	0.09	–	–
2693*	0.08	F8Ia	–	1	1	4	5	–		–		–	–	0.04		0.07	
2943	0.07	F5IV-V	D	1	5	22	13	–		–		0.07	0.08	–	0.09	–	0.07
2990*	0.07	K0IIIb	D	3	6	22	106	–	–	–	–	0.06	0.07	0.07	–	0.07	0.03
3685*		A2IV	–	1	1	6	2	0.05		0.04		–	–	–		–	
3845	0.04	K2.5III [1]	–	1	2	4	5	–		–		–	0.10	0.05	0.10	0.07	0.12
3873	0.09	G1II	–	2	3	7	12	–	0.19	–	0.19	–	0.31				
3982	0.07	B7V	D	8	8	108	187	0.05	0.07	0.04	0.04	0.04	0.06	0.02	0.04	–	0.05
4301*	0.03	K0IIIa	D	2	2	15	13	–	–	0.03	–	0.04	0.06	–	–	–	–
4554*	0.04	A0Ve	–	4	2	18	15	–	–	–	–	0.09	–	0.06	–	–	–
4662*	0.04	B8III[1]	–	4	1	351	8	0.11	0.04	0.06	–	0.05	–	–		–	
4763*	0.07	M3.5III	D	1	1	5	7	–		–		0.03	0.05	–		–	
4910*	0.08	M3III	D	1	2	4	5	–		0.14		0.11	0.10	–	–	–	–
4932*	0.19	G8IIIab	D	2	2	12	4	–	–	0.06	0.04	0.05	0.04	–	–	–	–
5191*	0.06	B3V	–	7	8	163	134	–	0.04	0.04	0.03	0.04	0.06	0.04	0.03	0.04	0.06
5340*	0.10	K1IIIb[1]	–	1	3	5	64	–		–		0.02	0.02	–	0.03	0.02	0.04
6056	0.03	M0.5III	D	1	1	7	9	–		0.03		–	0.03	–		–	
6148*	0.05	G7IIIa	D	2	1	12	12	0.05	–	–	–	–	0.04	–		–	
6556	0.11	A5III	D	5	4	121	20	0.12	–	0.09	–	0.08	–	0.05	–	0.05	–
6596		F5V	D	1	1	5	4	–		–		–	0.04	–		0.04	
6705*	0.16	K5III	D	1	2	20	17	–		0.04		0.03	0.02	–	–	–	–
6869	0.06	K0IV	D	1	0	6	0	0.09		0.06		0.04					

Table 2. (Contd.)

BS	V^m	Sp	Db	k		n		345 nm		459 nm		624 nm		820 nm		991 nm	
				vi	ir	vi	ir	S_v	Δm	S_v	Δm	S_v	Δm	S_v	Δm	S_v	Δm
6973	0.06	K3III-IIIb	–	1	0	6	0	–		0.06		0.05					
7417*	0.07	K5II?[1]	D	1	1	7	8	–		–		–	0.12	–		–	
7446*	0.04	B0.5III	–	1	0	10	0	–		0.06		0.06					
7602	0.06	G8IV	D	1	1	7	13	–		–		–	0.03	0.04		–	
7635*	0.09	M0III	–	2	1	5	11	–	–	0.17	0.11	0.15	0.11	–		–	
7665	0.13	G6-8IV	–	1	0	4	0	0.11		0.09		0.07					
8001*	0.08	A1V	SB	1	2	3	5	–		–		–	–	–	0.09	–	0.22
8079*	0.23	K4-5Ib-II	SB	2	2	11	11	–	–	–	–	–	0.06	–	0.04	–	0.03
8465*	0.21	K1.5Ib	SB	2	3	12	18	–	–	–	–	0.04	0.04	–	0.03	–	0.04
8650	0.04	G2II-III[1]	D	2	2	8	14					–	–	–	0.06	–	0.06
8675	0.06	A3V	–	1	0	7	0	0.08		0.07		0.07					
8709	0.04	A3V	–	2	1	165	13	0.09	–	0.09	–	0.09	–	0.03		–	
8781	0.05	B9V	–	8	9	365	146	0.11	0.07	0.08	0.03	0.16	0.08	0.12	0.10	0.10	0.10
9008	0.60	K1IIIa	–	1	1	6	6	0.25		0.05	–		–	–		–	

[1] BS 188 K0IIICH
1088 B8V+B8V
1347 B9VHgMn
3845 K2.5III-IIIbBa
4662 B8IIIHgMn
5340 K1IIIbCN
7417 K5II?+B?
8650 G2II-III+F0V

scopic binaries (SB) [the column Db]; the number of observing seasons, k, separately for the visual (vi) and infrared (ir), and the total number of observations for all the seasons, n, also separately for the visual and infrared; and S_v and Δm for each of the five spectral intervals. A dash indicates that variability was not detected or that S_v was not determined (for $m > 8^m$). The latter case is mainly characteristic of K–M stars at wavelengths near 345 nm. A blank field means that no observations are available for the given part of the spectrum; for Δm values, this can also mean that the data is present in a single seasonal catalog only.

The fraction of detected cases of variability is different for different spectral intervals. This could have methodical origins, for example the presence of different random errors for different wavelengths when deriving S_v or different catalog numbers when calculating Δm. However, the existence of a real dependence of the variations on wavelength is possible, manifest in different ways for stars of different spectral types. We found such a wavelength dependence for the brightness variability during a detailed analysis of the variability detection rates at different wavelengths and for stars of different spectral types [13].

Our comparison of the amplitude and wavelength distributions of the interseason brightness variations for stars in different variability groups (N, VN, N) [18] shows the following. The detection rates for low- and medium-amplitude variability ($\Delta m \leq 0.1^m$) are approximately the same for normal and variable stars, ~30%. The probability of finding large brightness variations ($\Delta m > 0.1^m$) among the normal stars in the infrared is comparable to the corresponding probability for variable stars, whereas no large variations are observed for the normal stars in the visual. This could be due to the fact that the visual is the domain that has been most often used earlier to search for stellar variability, so that stars whose visual brightnesses vary have, as a rule, already been noted as variables.

7. CONCLUSIONS

Our statistical study of the results of many-year spectrophotometric monitoring have enabled us to

detect real brightness variations for many stars, including normal stars, not previously believed to vary. Some 30% of these stars showed significant brightness variations exceeding the expected random scatter. This brightness variability can be indicated by the data for several observing seasons (different seasonal means in the data for the seasonal catalogs), as well as within a single season (larger observational error for the star, compared to the random error).

The limited size of the stellar samples and irregular nature of the observations (gaps in time) make the search for variability more difficult. For this reason, our analysis of the observational errors for the known variable stars indicates a lack of brightness variability in about 50% of the cases, independent of their variability type, amplitude, and period.

Detecting small variations in the presence of random scatter is possible only when a sufficiently large number of observations is available, enabling reliable statistical estimates. On the other hand, such estimation is naturally also hindered if the random errors are large. Note that the random observational error for each season was determined using all the stars, including known variables, possibly leading to overestimation of this error due to the presence of small brightness variations that could not be distinguished from the random scatter. All these factors hinder the detection of low-amplitude variability.

A comparison of our results with the data of the Hipparcos catalog [22] demonstrates that brightness variability had also been noted in [22] for 61% of the stars of any of our variability groups (N, VN, N) that displayed brightness variations.

The structure of our data does not enable accurate determination of the character of the variability for any individual star. The brightness variations appear to be associated with both gradual, long-term changes of the brightness from season to season and more abrupt jumps between seasons. More rapid, irregular variations within a season are also possible. The presence of different variability detection rates at different wavelengths indicates that components with different wavelength dependences are present in the variable signals from the stars.

Our analysis suggests that brightness variability is inherent to both previously known variable stars and normal stars. The differences in the amplitudes and spectral ranges are due only to variations in the contribution of the variable component.

Since normal stars are used as standards, their possible variability should be borne in mind. If possible, several standards should be used to ensure against corruption of the data due to variability of these standard stars.

REFERENCES

1. N. L. Alekseev, G. A. Alekseeva, A. A. Arkharov, *et al.*, Tr. Glav. Astron. Obs. Pulkovo **83**, 1 (1978).
2. N. L. Alekseev, G. A. Alekseeva, A. A. Arkharov, *et al.*, Izv. Glav. Astron. Obs. Pulkovo **202**, 71 (1984).
3. E. I. Hagen-Thorn, Izv. Glav. Astron. Obs. Pulkovo **211**, 26 (1996).
4. G. A. Alekseeva, A. A. Arkharov, V. D. Galkin, *et al.*, Baltic Astron. **5**, 603 (1996).
5. G. A. Alekseeva, A. A. Arkharov, V. D. Galkin, *et al.*, Baltic Astron. **6**, 481 (1997).
6. E. I. Hagen-Thorn, Izv. Glav. Astron. Obs. Pulkovo **212**, 289 (1998).
7. A. V. Kharitonov, V. M. Tereshchenko, and L. N. Knyazeva, *Master Spectrophotometric Catalog of Stars* (Nauka, Alma-Ata, 1978) [in Russian].
8. I. B. Voloshina, I. N. Glushneva, and T. S. Khruzina, Tr. Gos. Astron. Inst. im. Shternberga **52**, 182 (1982).
9. I. B. Voloshina, I. N. Glushneva, and V. I. Shenavrin, Tr. Gos. Astron. Inst. im. Shternberga **55**, 84 (1983).
10. N. S. Komarov, V. A. Pozigun, S. I. Belik, *et al.*, *Spectrophotometry of Stars at λλ 580–900 nm* (Naukova Dumka, Kiev, 1983) [in Russian].
11. A. L. Cochran, Publ. Dept. Astron. Univ. Texas **16**, 1 (1980).
12. H. L. Johnson and R. I. Mitchel, Rev. Mex. Astron. Astrofis. **1**, 299 (1975).
13. A. A. Arkharov, E. I. Hagen-Thorn, and E. V. Ruban, Izv. Glav. Astron. Obs. Pulkovo **215**, 5 (2000).
14. *General Catalog of Variable Stars*, Ed. by P. N. Kholopova (Nauka, Moscow, 1985) [in Russian].
15. A. A. Arkharov, T. Yu. Puzakova, and E. V. Ruban, Izv. Glav. Astron. Obs. Pulkovo **212**, 247 (1998).
16. A. A. Arkharov, T. Yu. Puzakova, and E. V. Ruban, Izv. Glav. Astron. Obs. Pulkovo **212**, 261 (1998).
17. A. A. Arkharov, T. Yu. Puzakova, and E. V. Ruban, Izv. Glav. Astron. Obs. Pulkovo **212**, 277 (1998).
18. A. A. Arkharov, E. I. Hagen-Thorn, T. Yu. Puzakova, and E. V. Ruban, Izv. Glav. Astron. Obs. Pulkovo **216**, 483 (2002).
19. E. I. Pustyl'nik, *Statistical Methods for the Analysis and Reduction of Observations* (Nauka, Moscow, 1968) [in Russian].
20. T. A. Agekyan, *Foundations of Error Theory for Astronomers and Physics* (Nauka, Moscow, 1972) [in Russian].
21. A. A. Arkharov, E. I. Hagen-Thorn, and E. V. Ruban, Izv. Glav. Astron. Obs. Pulkovo **215**, 21 (2000).
22. *The Hipparcos and Tycho Catalogues*, ESA SP-1200 (1997).

Translated by N. Samus'

Astronomy Reports, Vol. 49, No. 7, 2005, pp. 535–547. Translated from Astronomicheskiĭ Zhurnal, Vol. 82, No. 7, 2005, pp. 601–615.

Analysis of the Na, Mg, Al, and Si Abundances in the Atmospheres of Red Giants of Different Spectral Subgroups

L. I. Antipova[1], A. A. Boyarchuk[1], Yu. V. Pakhomov[1], and M. V. Yushkin[2]

[1] *Institute of Astronomy, ul. Pyatnitskaya 48, Moscow, 119017 Russia*

[2] *Special Astrophysical Observatory, Russian Academy of Sciences, Nizhniĭ Arkhyz, Karachaĭ-Cherkessian Republic, 357147 Russia*

Received January 12, 2005; in final form, February 17, 2005

Abstract—We analyze the Na, Mg, Al, and Si abundances in the atmospheres of more than 40 stars, including red giants of different spectral subgroups (normal red giants, mild and classical barium stars) and several supergiants. All these elements exhibit abundance excesses, with the overabundance increasing with the star's luminosity. The dependence of the overabundances for each of these elements on the luminosity (or $\log g$) is the same for all the spectral subgroups, testifying to a common origin: they are all products of hydrogen burning in the NeNa and MgAl cycles that have been dredged up from the stellar interiors to the outer atmospheric layers by convection that gradually develops during the star's evolution from the main sequence to the red-giant stage. The sodium abundances derived for several stars are lower than for other stars with similar atmospheric parameters. The ages and kinematic characteristics of these two groups of stars suggest that they probably belong to different stellar generations.

1. INTRODUCTION

This paper continues our series of studies of the chemical abundances in the atmospheres of red giants (see, e.g., [1–4]). We aim to estimate the abundances of as many elements as possible in the atmospheres of red giants belonging to different spectral subtypes using homogeneous, high-quality observational material and techniques, enabling a trustworthy comparative analysis of the results. We have now completed our analysis for a group of more than 40 stars that includes both normal red giants (without spectral peculiarities) and mild and classical barium stars.

This paper presents our results for the chemical compositions of four red giants, undertaken to increase our database. We refine, analyze, and discuss the relations between the atmospheric abundances of Na, Mg, Al, and Si and the luminosities of red giants [4].

2. CHEMICAL ABUNDANCES OF FOUR BARIUM STARS

The studied stars are listed in Table 1. We can see that three of these are moderate barium stars, and one is classified as a Ba1 star. According to the classification of [5], this star should be listed as a classical barium star, whereas, more recently, such stars have often been considered to be moderate barium stars [6]. It was concluded in [2], which was especially concerned with the chemical compositions of mild barium stars, that these stars are single red giants at a more advanced evolutionary stage than most normal red giants. However, different opinions are also encountered in the literature. Radial-velocity observations of barium stars are not numerous, and require long series of observations due to the long characteristic orbital periods of these stars; it cannot be ruled out that new observations of radial velocities will demonstrate binarity in some or all mild barium stars. With this in mind, we tried to analyze the available radial-velocity data for each of the studied stars as carefully as possible.

HD 9856. A check of the data in the Simbad astronomical database and several catalogs did not reveal any radial-velocity variations or other indications of possible binarity (such as common proper motions with surrounding stars or an ultraviolet excess testifying to the presence of a white dwarf).

HD 20644 is a bright late-type star. Although the Bright Star Catalog [7] contains no indications of spectral anomalies (in particular, of its barium-star nature), the star appears in the list of barium stars [8], where its class is estimated to be Ba0.5. The star has a low radial velocity (−2 km/s) [9]. Note that the latest version of [7] claims possible variability of its radial velocity, and the radial-velocity catalog [9] even identifies it as a possible spectroscopic binary. According to Simbad's data base, an essentially weaker

Table 1. List of program barium stars

No.	HD	HR	Name	Coordinates (2000.0)		m_v	Spectral type	Observatory and telescope
				α	δ			
1	9856	459	50 Cet	$01^h35^m59.0^s$	$-15°24'01''$	5.42	K2IIIaBa0.2CN1	SAO 6 m
2	20644	999	–	03 20 20.4	+29 02 54	4.47	K2II-IIIBa0.5	CrAO 2.6 m
3	104979	4608	*o* Vir	12 05 12.5	+08 43 59	4.12	G8IIIaCN-1Ba1CH1	CrAO 2.6 m
4	181053	7321	24 Aql	19 18 50.9	+00 20 20	6.41	K0IIIa:Ba0.3CH1	SAO 6 m

and variable star ($10.29^m-13.04^m$) is located very closely to the former star. In addition, it is also colder ($B-V=1.67^m$), i.e., it does not represent a white dwarf. However, according to the VizieR database, a special Tycho-based study found no indications of binarity. Thus, we conclude that HD 20644 is a single red giant. The typical radial-velocity uncertainty (2 km/s [9]) is comparable to the radial velocity itself, and it is possible that this is the origin of the suspicions of radial-velocity variability and spectroscopic binarity [9].

HD 104979 (or *o* Vir) is a well-studied barium star. The star's large proper motion is noted in the Simbad database. This could be due to nearness to the Sun (see Table 6 below), as well as a genuine high spatial velocity. The star is not recorded or suspected as a binary in either [7] or any other catalog. The radial-velocity catalog [9] also gives no indications of radial-velocity variations. The sole exception is [6], which reports that radial-velocity variations were detected in the course of CORAVEL observations covering 4764 days (a total of 25 radial-velocity measurements), which could be interpreted as orbital motion; the authors cautiously concluded that the star had an orbital period exceeding 4700 days. Incredibly, the radial-velocity change during this observing interval was only 2 km/s (!), with the uncertainty of a single observation being 0.3 km/s. The diagram in Fig. 2 of [6] shows a steady change in V_r, which could represent a sinusoidal variation due to orbital motion covering about one half or one fourth of the period. If this is the case, the actual period must a factor of two or four longer than 4700 days. Thus, it cannot be excluded that the star is a binary system with a very long orbital period, which is difficult to determine due to the small radial-velocity variations produced (only 1 or 2 km/s over the period). Among the program stars, this one has the highest level of barium-star characteristics (Table 1). This problem may be somewhat clarified by an analysis of the chemical composition of the star's atmosphere, in particular, the ratio of the carbon and nitrogen abundances, C/N, which can provide information about whether matter from an evolved component that has undergone a helium-burning stage was partially transferred to the red giant's atmosphere.

HD 181053. According to the Simbad astronomical database, this star is a member of a binary. The secondary is 0.2^m fainter than the primary, and its spectral type is given as F0. There are also two much fainter companions. Among the four stars, no two have similar proper motions. Thus, we conclude that no pair is a physical binary, and that HD 181053 is only a visual binary. The radial velocity given in [9] is -25.15 km/s, with an uncertainty of 0.04 km/s; the estimated probability that the radial velocity is constant (rather than variable) is 0.884. The absence of radial-velocity variations of HD 181053 that would suggest orbital motion, along with the different proper motions of the component stars, suggest that HD 181053 evolves as a single star, and that this evolution determines its spectral peculiarities.

We thus conclude that all the program stars, with the possible exception of HD 104979, are single red giants. In our subsequent analysis of their atmospheric abundances (also in agreement with Table 1), we will consider them to be moderate barium stars, whose *s*-element excesses are due to the fact that they are in a more advanced evolutionary stage than normal red giants (see the conclusion in [4]). The nature of *o* Vir (HD 104979) is not clear, as we will discuss below.

The last column of Table 1 indicates the observatory and the instrument used for each set of observations (SAO is the Special Astrophysical Observatory; CrAO is the Crimean Astrophysical Observatory). Details of our observations and data reduction are presented in [3]. The comparison of the equivalent widths for individual stars based on observations with the CrAO and SAO telescopes carried out in [3] demonstrates good agreement between these two sets of data, with the scatter of the individual equivalent widths (several milliÅngstrom) being comparable to the measurement uncertainties and with no evidence for systematic deviations, which is important when comparing results obtained with different instruments. The

results of our equivalent-width measurements are collected in Table 2, which is available electronically (ftp://cdsweb.u-strasbg.fr/pub/cats/J).

Our method for deriving the stellar-atmosphere parameters based on analyzing the abundances of iron-peak elements is described in detail in [1]. The derived effective temperatures, gravities, and turbulent velocities for each star are presented in Table 3. We used the ATLAS9 code of Kurucz [10] to calculate model atmospheres for each star, which we used together with the WIDTH9 code to calculate the atmospheric abundances based on data for uncontaminated (unblended) lines. The results are given in Table 4, which uses the following notation:

$$[\mathrm{El/H}] = \log\left(\frac{\epsilon(\mathrm{el})}{\epsilon(\mathrm{H})}\right)_* - \log\left(\frac{\epsilon(\mathrm{el})}{\epsilon(\mathrm{H})}\right)_\odot .$$

For each element, Table 4 also contains the number of lines, N, used to derive its abundance. Each star's abundances relative to iron ([El/Fe]) are shown in Fig. 1. We can see from Table 4 and Fig. 1 that the chemical-composition patterns of the studied stars are similar to those of the other stars in our sample: overabundances of Na, Mg, Al, Si and s-process elements. We showed earlier that the overabundances of Na, Mg, Al, and Si were correlated with the luminosity (see, for example, [4]). We present updated versions of these diagrams here (Figs. 2a, 2b, 2c, 2d, respectively, for Na, Mg, Al, Si) including the new stars, whose positions are shown by the larger symbols with numbers inside, corresponding to their numbers in Table 1. Table 2 indicates that, in general, these stars satisfy the previous relations fairly well. We also present an updated diagram of the relation between [s-el/Fe] and [Fe/H] (Fig. 3), which demonstrates that the new stars lie either among the normal giants and mild barium stars or on a sequence where, as was noted in [4], we encounter stars that could be classical barium stars whose binarity has not been established, or alternatively fairly old single stars. As we noted above, HD 104979 (o Vir) (star No. 3 in Fig. 3) may prove to be such a binary whose orbital period has not yet been determined.

We noted above that it may be possible to clarify the nature of HD 104979 (o Vir; where it is binary or single) using data on the abundances of CNO-cycle elements in its atmosphere. If the star is a single red giant, hydrogen burning via the CNO cycle occurs in its core, and the products of this cycle will be dredged up to the atmosphere by convection, so that the star should display the carbon deficiency and nitrogen excess typical of this stage of evolution. The C/N abundance ratio is sensitive to this process, and decreases with growing convection. However, if the star is binary, as is characteristic of classical barium stars, and if the secondary is a white dwarf—the remnant of a companion that has evolved and ejected its envelope—the star's atmosphere should contain traces of this envelope, namely, a carbon excess and nitrogen deficiency, i.e., consistent with the products of helium burning. Analysis of the C, N, and O abundances fall outside the scope of this paper. However, following [2], we examined data in the literature. Boyarchuk *et al.* [2] present mean C/N ratios for 53 red giants (1.72 ± 0.8) and 20 moderate barium stars (1.10 ± 0.5) derived from literature data, together with the corresponding references. The mean C/N ratio for 4 classical barium stars presented in [11] is 2.56 ± 0.3, higher than for the other groups and testifying to the presence of helium-burning products. The value C/N = 2.40 is given for o Vir [11]. This ratio is much closer to the value for the classical barium stars than the value for the normal red giants or mild barium stars. Thus, given the high barium class of the star (compared to the other stars studied here), evidence for long-period radial-velocity variations, and the high C/N abundance ratio, we conclude that the probability of HD 104979 (o Vir) being a classical barium star is high.

Table 3. Atmospheric parameters for the barium stars

HD	T_{eff}, K	$\log g$	V_t, km/s	[M/H]	[s-el/Fe]
9856	4400	1.81	1.64	−0.16	0.20 ± 0.09
20644	4160	1.47	1.25	+0.08	0.38 ± 0.12
104979	4929	2.41	1.09	−0.30	0.73 ± 0.13
181053	4837	2.45	1.33	−0.18	0.47 ± 0.08

3. DEPENDENCE OF THE Na, Mg, Al, AND Si ABUNDANCES ON GRAVITY

As a star evolves from the main sequence to the red-giant branch, it develops convection that becomes stronger as the star's luminosity increases, and brings the products of nuclear reactions occurring in its core during the main-sequence stage to the stellar surface. This was demonstrated by the discovery of Na overabundances in the atmospheres of supergiants [12], and then also giants [1], leading to the conclusion that the NeNa hydrogen-burning cycle had operated in the interiors of these stars [12, 13]. Later, overabundances of Mg, Al, and Si were detected, indicating that the MgAl hydrogen-burning cycle operated in those stellar cores. These abundance anomalies all show the same pattern, namely an increase with increasing luminosity (decreasing $\log g$), providing evidence for the growth of convection with increase in the star's luminosity. This problem

Table 4. Atmospheric elemental abundances

	HD 9856		HD 20644		HD 104979		HD 181053	
	N	[El/H]	N	[El/H]	N	[El/H]	N	[El/H]
NaI	2	0.09 ± 0.02	3	0.55 ± 0.04	2	-0.33 ± 0.03	1	-0.10
MgI	1	0.22	2	0.22 ± 0.01	3	0.02 ± 0.10	2	-0.02 ± 0.01
AlI	2	0.17 ± 0.06	1	0.31	2	0.05 ± 0.04	2	-0.03 ± 0.05
SiI	5	-0.09 ± 0.08	10	0.08 ± 0.07	15	-0.19 ± 0.09	19	-0.03 ± 0.08
CaI	2	-0.17 ± 0.01	3	-0.10 ± 0.12	8	-0.15 ± 0.08	3	-0.04 ± 0.09
ScI	5	-0.07 ± 0.07	4	-0.16 ± 0.12	1	-0.20	4	-0.23 ± 0.02
ScII	7	-0.04 ± 0.07	4	0.16 ± 0.01	4	-0.09 ± 0.03	6	-0.16 ± 0.05
TiI	43	-0.21 ± 0.08	26	0.02 ± 0.10	22	-0.25 ± 0.07	42	-0.19 ± 0.07
VI	11	-0.14 ± 0.09	7	0.11 ± 0.13	18	-0.34 ± 0.11	12	-0.20 ± 0.07
CrI	34	-0.17 ± 0.10	18	0.01 ± 0.12	8	-0.28 ± 0.15	24	-0.17 ± 0.08
CrII	4	-0.14 ± 0.05	–	–	1	-0.37	2	-0.17 ± 0.01
MnI	3	-0.07 ± 0.11	2	0.16 ± 0.06	2	-0.58 ± 0.07	5	-0.34 ± 0.11
FeI	120	-0.17 ± 0.12	73	0.07 ± 0.10	117	-0.30 ± 0.11	121	-0.12 ± 0.07
FeII	10	-0.21 ± 0.11	8	0.08 ± 0.16	10	-0.29 ± 0.07	11	-0.17 ± 0.07
CoI	15	-0.11 ± 0.11	14	0.20 ± 0.11	9	-0.27 ± 0.11	10	-0.17 ± 0.09
NiI	43	-0.20 ± 0.14	23	0.09 ± 0.12	30	-0.28 ± 0.10	50	-0.21 ± 0.06
ZnI	–	–	–	–	–	–	2	-0.14 ± 0.06
SrI	–	–	–	–	–	–	1	0.40
YII	4	-0.11 ± 0.08	3	0.26 ± 0.03	3	0.25 ± 0.10	7	0.35 ± 0.09
ZrII	3	0.01 ± 0.02	1	0.41	1	0.35	2	0.42 ± 0.06
LaII	3	-0.03 ± 0.05	4	0.65 ± 0.12	2	0.64 ± 0.03	6	0.35 ± 0.07
CeII	5	0.16 ± 0.08	5	0.26 ± 0.18	1	0.45	7	0.27 ± 0.18
PrII	4	0.07 ± 0.07	4	0.47 ± 0.09	–	–	2	0.29 ± 0.01
NdII	19	0.09 ± 0.13	11	0.37 ± 0.10	5	0.48 ± 0.08	18	0.43 ± 0.11
SmII	–	–	–	–	–	–	3	-0.10 ± 0.02
EuII	–	–	2	-0.02 ± 0.20	1	0.24	–	

was widely discussed earlier (see [1–4], where references to the corresponding theoretical studies can also be found).

As the number of studied objects increased, it was found that some stars did not satisfy the general relation: they lay below it, i.e., their [Na/Fe] and [Si/Fe] abundances were lower than those for other stars with similar $\log g$ [4, Figs. 2a, 2d]; the origins of these deviations from the general relation remained unclear [4].

Here we consider possible reasons why some stars might display abundances below the expected values. Let us begin with the sodium abundances (Fig. 2a).

Figure 2a shows that there are at least four stars with Na overabundances in their atmospheres that lie far below those exhibited by the stars satisfying the general relation (with the same $\log g$). These differences are larger than the observational uncertainties, reaching 0.3–0.4 dex for some stars. The four stars are HD 175190, HD 88562, HD 183915, HD 104979, which we will refer to below as the "problem stars."

The deviations could be associated with (1) errors in the equivalent-width measurements due to incor-

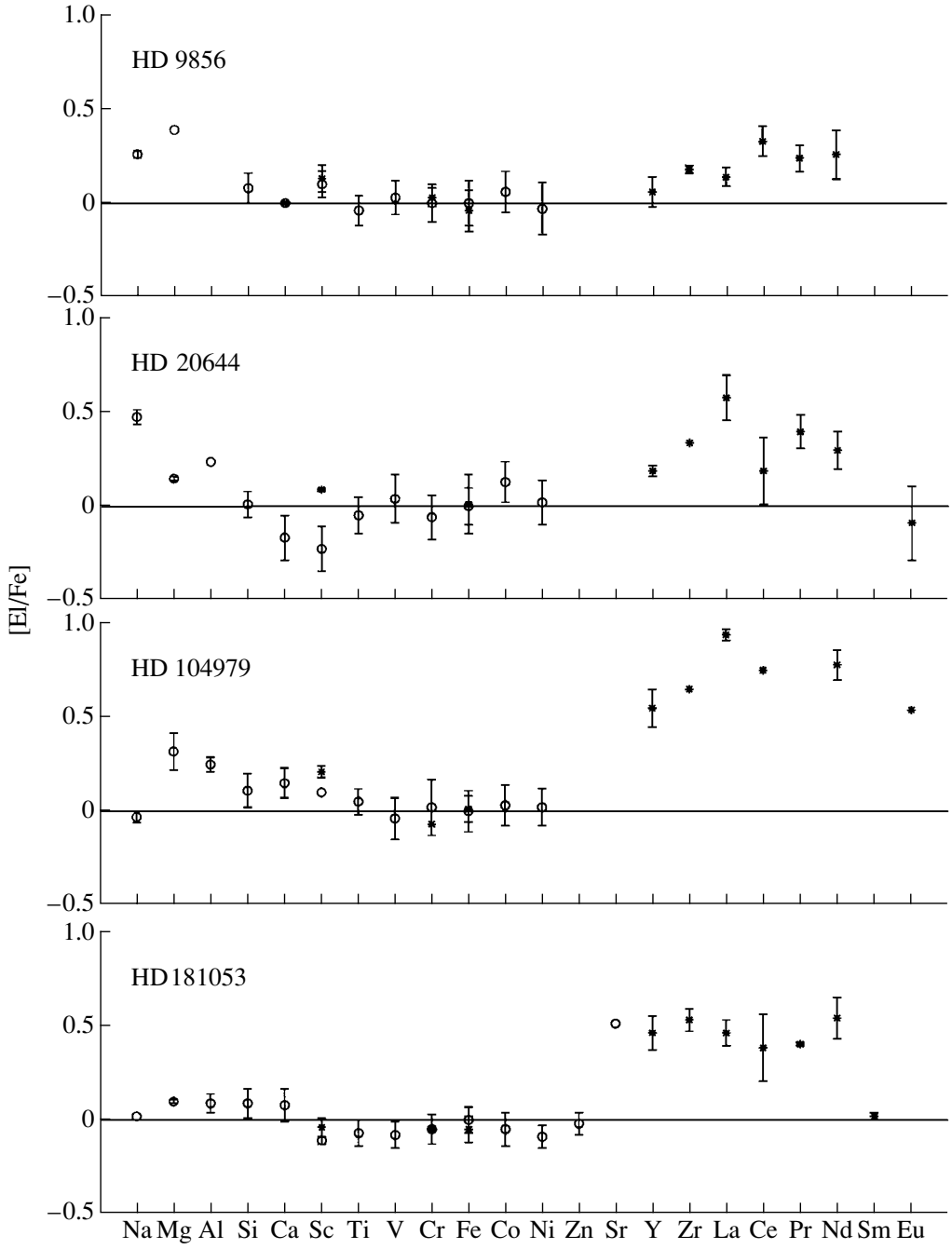

Fig. 1. Elemental abundances in the atmospheres of the program barium stars relative to their abundances in the solar atmosphere. Circles denote abundances derived from lines of neutral atoms and asterisks, those derived from lines of ions. The error bars are shown. The absence of an error bar means that the abundance was derived from a single line.

rect fitting of the continuum, (2) non-LTE effects that are not taken into account, (3) the use of incorrect atmospheric parameters, or (4) a real reduced abundance of Na for some or all of these stars.

The problem stars are 4 of 28 classical and moderate barium stars; the remaining 24 stars, like the normal giants and supergiants, satisfy the relation fairly well. Note that our observations of the classical barium stars were acquired with the 6 m telescope of the Special Astrophysical Observatory, whereas observations of sufficiently bright moderate barium stars, including the problem star HD 104979, were obtained at the Crimean Astrophysical Observatory. The observed spectral regions were somewhat different in these two cases: 4600–6100 Å for the SAO and 5100–6800 Å for the CrAO. Consequently, the

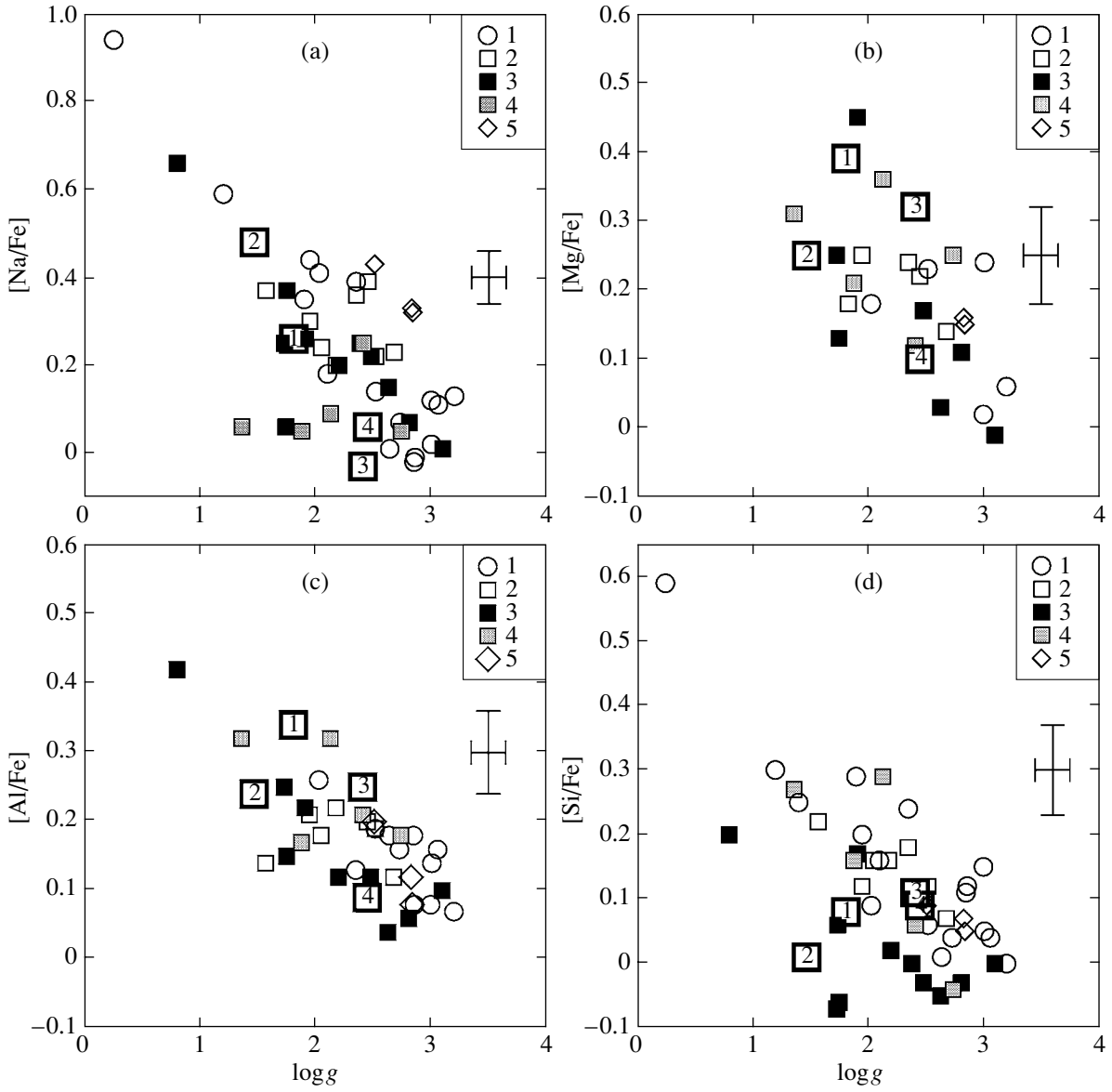

Fig. 2. Overabundances of (a) Na, (b) Mg, (c) Al, and (d) Si relative to the iron abundance in the red-giant atmospheres, compared to the analogous abundances for the Sun. Shown are data for (1) normal giants and supergiants; (2) moderate barium stars; (3) classical barium stars in binary systems; (4) classical barium stars with no binarity indications; and (5) giants in the Hyades cluster.

Na abundances for the different stars were derived from different lines, depending on the observed spectral region. Since abundance estimates derived from different lines can differ for several reasons (for example, because of non-LTE effects, which may be different for different lines), it is preferable to compare abundances derived using the same lines.

For this purpose, we acquired new observations of several moderate and classical barium stars at 5000–6700 Å using the NES quartz echelle spectrograph [14] on the SAO 6 m telescope. The spectra have good resolution ($R = 60\,000$) and high signal-to-noise ratio ($S/N > 100$). To improve the efficiency of our spectroscopic observations and obtain high signal-to-noise ratio without loss of resolution, we employed an image slicer rather than the standard spectrograph entrance slit [15], which increased the transmission at the spectrograph's entrance by a factor of three. The light detector installed at the NES spectrograph is a large, high-efficiency CCD with 2048×2048 pixels [16]. The wavelength scale for the stellar spectra was calibrated using spectra from a hollow-cathode lamp whose cathode was coated with thorium salts and its bulb filled with argon. The initial reduction of the CCD images was carried out in the MIDAS package using special software developed for

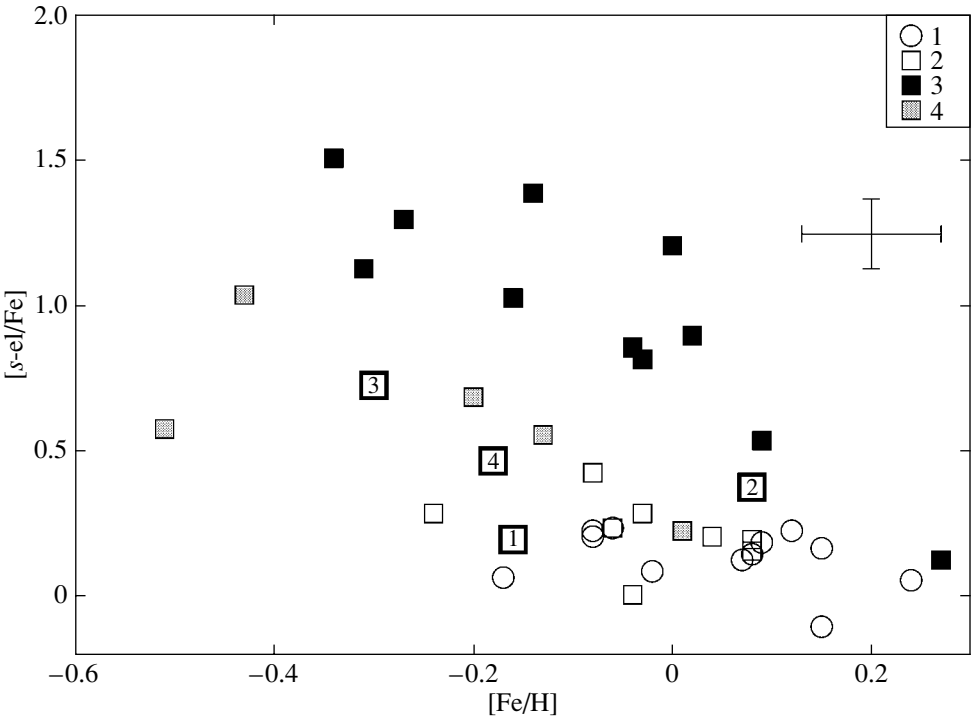

Fig. 3. Relation between the overabundances of the *s*-process elements and metallicity. The symbols are the same as in Fig. 2.

correct extraction of echelle spectra taken with an image slicer [17]. We used these spectroscopic data to obtain new sodium-abundance estimates from the NaI $\lambda\lambda$6154, 6160 Å lines, as we had earlier for the normal giants and supergiants. Our estimates of the Na, Mg, Al, and Si equivalent widths for the new SAO observations and the abundances derived from them are collected in Table 5, which is available electronically (ftp://cdsweb.u-strasbg.fr/pub/cats/J).

Note that the spectral range used contains fewer lines, so that the continuum can be fit more confidently than in the band observed earlier at the SAO (4600–6100 Å). For this reason, the abundance estimates derived from the new observations seem preferable.

We used these results to replot the dependence of the Na overabundances on $\log g$ for the atmospheres of the red giants studied by us and four supergiants whose data were taken from [12, 18, 19], using only abundance estimates derived from the NaI $\lambda\lambda$6154, 6160 Å lines (Fig. 2a of the present study).

A comparison of Fig. 3a in [4] and Fig. 2a in this paper shows that the Na abundances derived from the NaI $\lambda\lambda$6154, 6160 Å lines are somewhat lower than those obtained earlier from NaI lines in the range 4600–6100 Å, causing the deviations of these stars from the general relation to increase somewhat. NaI lines are known to be influenced by non-LTE effects, with the correction always being negative and differing from line to line. Including the non-LTE corrections did not eliminate the observed Na overabundances of red giants, demonstrating that they were real [20, 21]. In our red-giant studies, we preferred to use the NaI $\lambda\lambda$6154, 6160 Å lines, for which the non-LTE corrections are the smallest [22], although we did not include these corrections. Since the corrections for other NaI lines are larger, the sodium-abundance estimates obtained without the corrections will be systematically lower when derived from the NaI $\lambda\lambda$6154, 6160 Å lines than when derived from lines at bluer wavelengths in the observed range. Note that the differences between the abundances derived from the lines in the two spectral regions are comparable to the magnitude of the non-LTE corrections [22]. Thus, we conclude that problems fitting the continuum level at 4600–6100 Å, the choice of certain lines for the sodium-abundance measurements, and neglect of non-LTE corrections cannot explain the reduced Na abundances observed in the atmospheres of some stars (Fig. 2a).

The stars with reduced [Na/Fe] abundances are, on average, cooler than stars lying closer to the sequence (see Table 6 below). Generally speaking, the atmospheric parameters, and hence abundance estimates, obtained using our technique are less accurate in the low-temperature domain than for higher temperatures. Our analysis for the red giants employs Kurucz's ATLAS9 code for the model-atmosphere

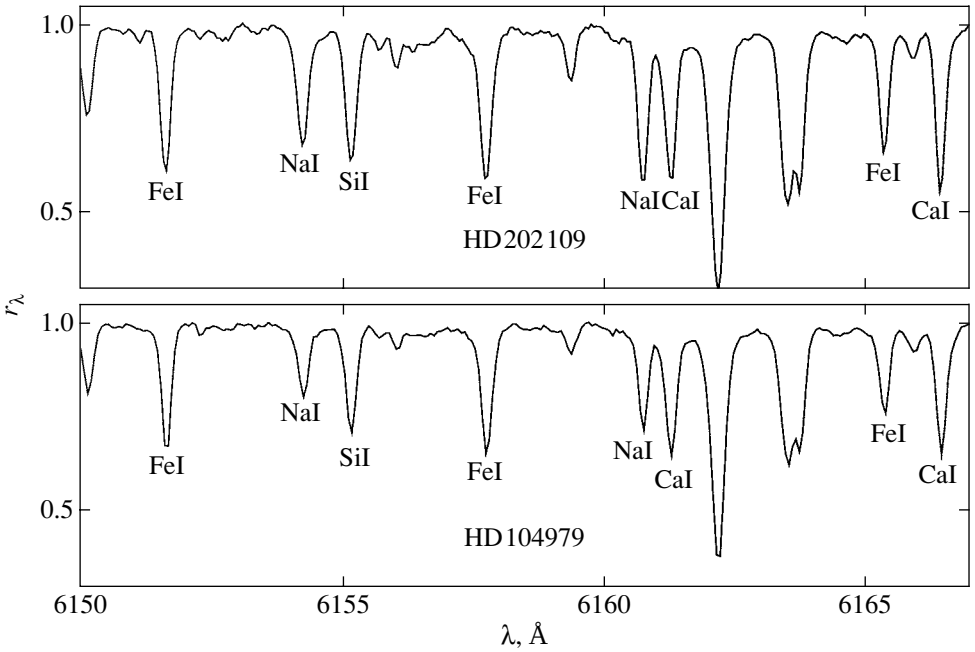

Fig. 4. Comparison of the spectrograms of ζ Cyg (HD 202109) and o Vir (HD 104979).

calculations. However, this code does not take into account three-atom molecules when determining the opacities, which can be a significant effect for cool stars. The limiting temperature for which ATLAS9 is applicable is given as 3500 K. However, when deriving the atmospheric parameters, we carried out preliminary calculations of the iron-peak abundances over a fairly wide range, to both sides of the expected values. In principle, this circumstance could influence our estimates of the atmospheric parameters, thereby influencing the abundances.

This revision of the atmospheric parameters for the cool stars was important for one of the coolest stars, HD 178717, which was studied earlier and displayed good agreement with the [Na/Fe]–$\log g$ relation. According to [23, 24], the atmospheric carbon and nitrogen abundances for this K4 star are enhanced compared to those of normal red giants. As a result, the spectrum exhibits numerous lines of molecular compounds, which often distort the iron-group lines used to derive the atmospheric parameters. The molecular bands also have a strong effect on the continuum, which is difficult to trace for this star. To solve this problem and find lines that are not blended with molecular bands, we calculated synthetic molecular spectrum using V.V. Tsymbal's SynthV code and the molecular database. This yielded for the atmospheric parameters of HD 178717 $T_{\rm eff} = 3973$ K, $\log g = 0.80$, and $V_t = 1.81$ km/s. These refined atmospheric parameters differ appreciably from the old values, but, although the sodium abundance is changed by using these parameters, the star remains on the relation. We conclude that our use of Kurucz's ATLAS9 code is unlikely to lead to systematically low sodium-abundance estimates, and is not able to explain the deviations of several cool stars from the general relation.

We proceeded to analyze the spectra of the problem stars in order to test if the sodium deficiency in their atmospheres could be real. This required that we find for each of the problem stars another star among those we studied earlier that had similar atmospheric parameters and showed good agreement with the [Na/Fe]–$\log g$ relation.

We begin with HD 104979 (o Vir), which shows a reduced abundance of Na, but is not as cool as the other three problem stars. The atmospheric chemical composition of this star was analyzed using observations obtained at the CrAO, i.e., using the $\lambda\lambda 6154, 6160$ Å lines. We first remeasured the NaI equivalent widths taken with the same telescope one year earlier. The equivalent widths of the NaI lines in the two spectra coincided to within ± 2 mÅ, ruling out the possibility of incorrect line measurements. We then selected a star from among the studied red giants, ζ Cyg (HD 202109), whose atmospheric parameters ($T_{\rm eff} = 4977$ K, $\log g = 2.52$, [Fe/H] $= -0.08$) are closest to those of o Vir ($T_{\rm eff} = 4929$ K, $\log g = 2.41$, [Fe/H] $= -0.30$). Figure 4 displays fragments of the two stars' spectra containing the Na $\lambda\lambda 6154, 6160$ Å lines, which were used to determine the sodium abundances. We can see that

the NaI lines in the spectrum of *o* Vir are much weaker, whereas the lines of other elements have approximately the same intensity, implying a lower sodium abundance for *o* Vir, in the presence of very similar atmospheric parameters. Model-atmosphere calculations showed that the sodium lines are not sensitive to variations of $\log g$, but change substantially with varying temperature. Deriving the "needed" abundance from the given equivalent width requires a temperature of 5200 K, much higher than the various effective-temperature estimates for the star: $T_{\rm eff} = 4990$ K [11], 4893 K [25], 4870 K [26], 4825 K [27], 4850 K [28]. Moreover, in addition to the $T_{\rm eff}$ value derived from the spectrum, we obtained estimates using the $T_{\rm eff}$–$(B-V)$ relation based on information about the diameters of the studied stars (4870 K) and their IR fluxes (4855 K, see Appendix). Thus, the reduced Na abundance in this star's atmosphere cannot be explained by uncertainty in the equivalent-width measurements or atmospheric parameters, and we are forced to conclude that the deficiency is real.

We can compare the sodium-line intensities for other pairs of stars with similar atmospheric parameters in this same way. For example, the equivalent widths of the NaI λ6154 Å line for HD 20644 ($T_{\rm eff} = 4160$ K, $\log g = 1.75$, [Fe/H] $= +0.08$), which satisfies the relation well, and HD 175190 ($T_{\rm eff} = 4188$ K, $\log g = 1.36$, [Fe/H] $= -0.13$), which lies below it, are 140 and 107 mÅ, respectively; the equivalent widths of the NaI λ6160 Å line are 164 and 128 mÅ, respectively. In the case of HD 9856 ($T_{\rm eff} = 4400$ K, $\log g = 1.64$, [Fe/H] $= -0.16$), which agrees with the relation, the equivalent lines of the NaI $\lambda\lambda 4668.6, 4982.8, 5682.6$ Å lines are 121, 148, and 174 mÅ, whereas, for HD 88562 ($T_{\rm eff} = 4274$ K, $\log g = 1.74$, [Fe/H] $= -0.16$), they are 102, 132, and 162 mÅ. A similar situation arises when we compare the NaI equivalent widths for HD 199939, which satisfies the relation, and HD 183915, which falls below it. We thus conclude that the sodium lines are systematically weaker for the problem stars than for stars with similar atmospheric parameters that satisfy the relation well. The reduced line intensities lead to the reduced sodium abundances we have obtained. Thus, the four stars that fall below the general relation have genuine low Na abundances.

A star's position in Fig. 2a is determined not only by its [Na/Fe] abundance, but also by $\log g$, which has an uncertainty of about 0.1 dex [29] and is unable to significantly influence the pattern of the stellar positions. In order to bring the problem stars in line with the general relation, $\log g$ would have to be increased by approximately 0.6–1.0 dex, which would introduce strong disagreements between the abundances derived from lines of neutral atoms and ions of the same element.

Thus, the reduced [Na/Fe] abundances in the atmospheres of the four problem stars are real. Let us now discuss possible physical origins of this result.

The [Na/Fe] abundance could be reduced by convection, for which the theory is not fully understood. We might expect that convection could be suppressed or slowed in some stars, for example, by their magnetic fields, hindering the dredge-up of matter from the stellar interiors to the atmospheres.

Another possible origin could be the nonuniform chemical composition of the Galaxy. Although the chemical composition of the Galaxy as a whole agrees with the standard theory for the Galaxy's evolution, there exist regions where the abundances deviate from predicted values. In particular, there exist groups of stars with reduced Na abundances. For example, chemical-composition studies of halo and disk stars, whose metallicity ranges considerably overlap ($-1.3 <$ [Fe/H] < -0.5) [30], indicate the presence of a subgroup with reduced abundances of α-process elements and Na. Analysis of their spatial velocities suggests that they are older than most disk and halo stars, with the anomalies occurring in regions whose chemical evolution was different from that predicted by the standard theory for the Galaxy's evolution (because they had a reduced rate of SN II outbursts, which are the main source of these elements).

Possible origins of the reduced [Na/Fe] atmospheric abundances of the four problem stars are that these stars are older, or were formed in regions in the Galaxy where the initial chemical composition differed from that for matter in the solar neighborhood. To test this hypothesis, we compared the ages and kinematic characteristics of our stars. The list of all the stars presented in Table 6 contains the distance R to the star calculated using the parameters from HIPPARCOS catalogue [31]; the star's distance to the Galactic plane Z; the total spatial velocity relative to the Sun V_0; the components of the Galactic velocity relative to the centroid of the nearest stars, U, V, W; the effective temperature derived from the photometric calibration $T_{\rm eff}$ (see the Appendix); the metallicity [Fe/H]; the mass $M/M_\odot$; and our age estimate. The masses and ages were determined using the evolutionary tracks of [32, 33] taking into account the metallicities of the studied stars.

The data in Table 6 indicate that all the studied stars belong to the disk population. This is demonstrated by their low heights above the Galactic plane Z and their Galactic velocities, which are typical of disk objects. Table 6 also shows that, as a rule, the stars with reduced [Na/Fe] abundances

Table 6. Some characteristics of the studied red giants and supergiants

HD	R, pc	Z, pc	V_0, km/s	U, km/s	V, km/s	W, km/s	$T_{\rm eff}$, K	[Fe/H]	$M/M_\odot$	Age, years
Normal supergiants										
8890	132	59	33.6	−5	−13	0	6055	+0.05	6.3	6.39×10^7
45348	96	−41	24.9	−1	−6	8	7400	−0.12	9.5	2.34×10^7
194093	467	15	9.5	7	7	1	5806	+0.00	12	1.52×10^7
224014	3571	−281	105.7	109	10	−29	6000	+0.05	24	6.79×10^6
Normal red giants										
9270	90	−35	17.4	−4	13	−1	4898	−0.02	3.9	1.85×10^8
19787	51	−14	44.0	−27	−6	13	4759	−0.08	2.1	1.08×10^9
40035	43	5	33.1	−5	−13	12	4816	+0.08	2.3	8.09×10^8
62509	10	2	30.9	−5	19	−18	4836	+0.07	2.0	1.08×10^9
112989	275	187	32.9	−8	−8	−5	4521	+0.12	5.2	8.98×10^7
113226	31	30	43.5	−27	−2	−4	4964	+0.24	2.7	6.90×10^7
153210	26	13	67.3	−38	−31	7	4552	+0.13	1.6	2.20×10^8
168723	18	0	80.3	52	−51	22	4964	−0.18	1.8	1.65×10^9
180711	30	6	31.0	−10	38	8	4920	−0.08	2.4	7.00×10^8
188947	42	1	28.1	9	−13	8	4778	+0.15	2.2	9.74×10^8
197912	63	−4	7.7	6	15	13	4740	+0.09	2.4	7.01×10^8
216131	35	−9	28.7	−6	16	−15	4964	−0.06	2.4	7.00×10^8
Red giants in the Hyades star cluster										
27371	47	−19	46.8	−31	−5	6	4857	+0.11	2.6	5.56×10^8
27697	47	−18	46.1	−31	−4	5	4877	+0.19	2.5	5.91×10^8
28305	48	−16	46.6	−31	−5	6	4816	+0.11	2.6	5.33×10^8
Moderate barium stars										
9856	168	−162	29.9	−13	15	−10	4470	−0.16	2.5	5.90×10^8
20644	196	−78	17.3	18	8	−7	3961	+0.08	3.2	3.90×10^8
49293	114	1	14.5	2	6	−1	4634	+0.08	3.3	2.00×10^8
74739	91	28	26.3	−4	−6	5	4816	−0.21	3.5	2.61×10^8
83618	84	49	39.3	26	−17	22	4312	−0.03	2.5	2.68×10^9
133208	67	58	24.7	6	−7	−1	4898	+0.04	3.5	1.38×10^8
158899	113	54	29.6	−11	7	−10	4130	−0.06	2.4	1.01×10^9
176411	47	4	53.5	−8	−35	5	4686	−0.04	2.2	3.06×10^8
181053	150	−16	31.6	−19	6	2	4730	−0.18	2.0	1.09×10^9
202109	46	−5	24.3	23	28	−7	4857	−0.03	2.9	4.26×10^8
215665	121	−32	33.6	−14	0	−9	4704	+0.09	4.2	1.52×10^8

Table 6. (Contd.)

HD	R, pc	Z, pc	V_0, km/s	U, km/s	V, km/s	W, km/s	T_{eff}, K	[Fe/H]	$M/M_\odot$	Age, years
Classical barium stars with known periods										
16458	152	25	62.8	−41	21	−27	4311	−0.27	1.9	1.30×10^9
46407	121	−9	15.1	14	28	2	5077	−0.14	2.9	4.12×10^8
77247	349	122	25.5	23	−5	0	5069	+0.09	3.8	2.03×10^8
88562	319	88	38.7	24	−16	−10	4183	−0.16	1.0	1.34×10^{10}
101013	141	73	36.6	−10	−14	1	5007	+0.00	3.1	3.36×10^8
178717	344	2	18.4	10	31	−1	3940	−0.31	3.5	3.28×10^8
196673	362	−14	29.1	6	−12	0	4736	+0.27	3.9	1.80×10^8
199394	157	1	35.3	43	10	−4	5128	+0.02	2.7	5.18×10^8
199939	316	−2	44.6	33	−20	−8	4685	−0.34	3.1	3.22×10^8
204075	122	−45	11.1	9	25	9	5192	−0.04	4.6	1.23×10^8
205011	158	−27	15.5	5	28	1	4916	−0.03	2.9	3.87×10^8
Classical barium stars with no period										
65854	157	43	41.5	−10	−18	−6	5048	−0.20	1.6	2.19×10^9
104979	52	48	64.7	−44	12	−27	4855	−0.30	2.1	9.12×10^8
130386	292	116	37.2	16	−21	9	4725	+0.01	2.5	5.92×10^8
139409	181	46	72.0	47	−35	42	4835	−0.51	1.9	1.25×10^9
175190	82	−7	118.5	105	44	−56	4138	−0.13	1.2	6.48×10^9
183915	287	−8	45.7	−23	−15	8	4642	−0.43	3.2	3.17×10^8

are older and less massive (with masses below $2\,M_\odot$) than the other stars. An exception is HD 183915, with an age of about 3×10^8 yrs and a mass of about $3\,M_\odot$, like most stars in Table 6. Given the Galactic velocity relative to the velocity centroid for the nearest stars ($\sigma_u : \sigma_v : \sigma_w = 35 : 25 : 20$ km/s), on average, the problem stars have higher velocities than the other stars. In fact, HD 175190, which demonstrates the strongest deviation from the [Na/Fe]–$\log g$ relation, is distinguished by its high velocity (exceeding more than $2\sigma_{u,w}$); HD 104979 has U and V velocities between $1\sigma_{u,v}$ and $2\sigma_{u,v}$, and the velocities of HD 88562 and HD 183915 are within $1\sigma_{u,v}$.

We conclude from this analysis that the reduced [Na/Fe] abundances for HD 175190 and HD 104979 could be associated with higher ages, as well as an origin in Galactic regions with chemical compositions differing from the solar composition. Age is probably a factor for HD 88562, which is the oldest object in our sample and is likely a member of an earlier generation of stars. If this is correct, this indicates that some stars belonging to earlier generations have reduced [Na/Fe] abundances. Note also that the red giants of the young Hyades open cluster have higher [Na/Fe] abundances in their atmospheres [29]. Thus, Fig. 2a demonstrates a splitting of the [Na/Fe]–$\log g$ relation for stars of different generations. HD 183915 is an exception to our conclusions, and its reduced [Na/Fe] abundance appears to have other origins.

When studying red giants, it is important to remember that the atmospheric abundance of an element during this stage is a sum of the initial abundance (observed in dwarf stars; see, for instance, [30]) and products of nuclear reactions that took place in the star's interior during the main-sequence stage and were dredged up to the star's atmosphere by convection during the star's evolution towards the red-giant branch. As we noted above, these could be products of hydrogen burning via the CNO, NeNa, and MgAl cycles, with the contribution of each cycle depending on many parameters. The last two cycles are closely connected via the reaction transforming

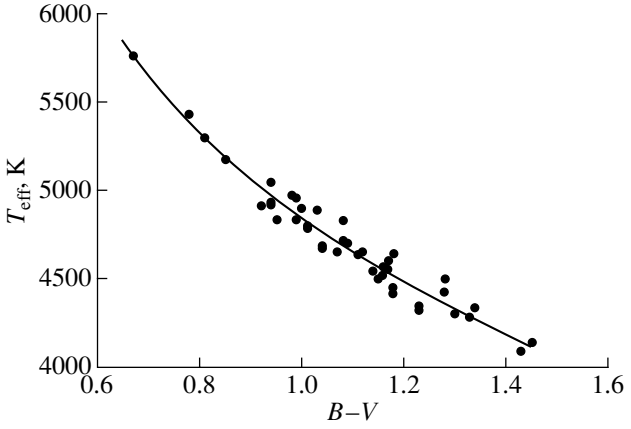

Fig. 5. The $T_{\rm eff}$–$(B-V)$ calibration relation for red giants.

Na to Mg; there is also a transformation of Mg to Si in the MgAl cycle. Due to these leakage reactions, certain atoms are excluded from the cycle (cf. [34], for example). According to [34], the rates of the leakage reactions depend strongly on the temperature, and the last cycle may even cease to operate at very high temperatures. For this reason, it is not currently possible to accurately estimate the addition to an element's original abundance. Thus, if we find, for example, a reduced [Na/Fe] abundance in a star, then, due to the many free parameters involved, we cannot be certain that the other elements involved in the relevant cycles will also have reduced abundances. As a result, the positions of stars in the plots of the relations among the overabundances of Mg, Al, and Si in Figs. 2b, 2c, 2d do not qualitatively repeat their positions in Fig. 2a. Therefore, we only note the existence of these relations, but do not analyze them in detail.

The discovery of stars with reduced [Na/Fe] abundances is interesting. However, given the small number of such stars in our sample, these results should be considered preliminary. Additional observations are needed to enable similar analyses with a larger volume of statistical data.

4. CONCLUSIONS

(1) We have analyzed the atmospheric abundances of four barium stars. Our results agree with those for the barium stars studied by us earlier [2–4]: the overabundances of Na, Mg, Al, and Si satisfy the dependences on $\log g$ derived earlier, and the overabundances of s-process elements satisfy the dependence on metallicity.

(2) We argue that the barium star HD 104979 (o Vir) may be a component of a very-long-period binary system.

(3) Of the more than 40 stars studied by us using a single set of techniques, four stars exhibit reduced [Na/Fe] abundances compared to those expected from the general relation between [Na/Fe] and $\log g$ for disk stars. Our analysis indicates that the reduced [Na/Fe] abundances for these stars are real.

(4) We conclude that the stars with reduced [Na/Fe] abundances may belong to an earlier generation of stars, or may have been formed from matter whose chemical composition differed from that of the material in the solar neighborhood; evidence for this is provided by the facts that (i) their ages are, on average, higher than those for the other stars, and (ii) their spatial velocities are, on average, higher than those for the velocity centroid of the nearest stars.

ACKNOWLEDGMENTS

This study was partially supported by the Russian Foundation for Basic Research (project no. 03-02-17336), the Program of Support for Leading Scientific Schools of Russia (grant no. NSh-162.2003.02), the program "Unstable Processes in Astronomy" of the Presidium of the Russian Academy of Sciences, and the Federal Science and Technology Program "Astronomy" (section no. 1102). The authors are grateful to A.S. Rastorguev for advice concerning the kinematics of the Galaxy.

APPENDIX

DETERMINING STELLAR EFFECTIVE TEMPERATURES USING THE CALIBRATION RELATION BETWEEN $T_{\rm eff}$ AND $B-V$

We noted at the beginning of this paper that we derived the stellar atmospheric parameters from an analysis of lines of iron-group elements in the spectra, using model stellar atmospheres. These parameters are "formal" and depend on the model grid used. It was shown earlier that the resulting parameters describe the stellar spectra well, but demonstrate slight systematic deviations from the values determined using nonspectroscopic techniques [35].

To analyze the positions of the studied stars in the temperature–luminosity diagram (to determine their masses, ages, and evolution stages), it is necessary to know their effective temperatures, $T_{\rm eff}$. Here, values derived from photometric measurements should be preferred.

We determined the effective temperatures using our calibration relation between $T_{\rm eff}$ and the $B-V$ color index. To derive this calibration, a number of reference stars are needed, whose effective temperatures

Table 7. Coefficients in the approximation of the $(B-V)$–temperature relation using the IRFM data [37]

A_0	A_1	A_2	A_3
10633	−11573	7767.5	−1990.7

have the best possible accuracy and whose photometric parameters are known. One of the most accurate methods when many observations are available is the IRFM technique described in [36]. A catalog of stars with IRFM temperatures is presented in [37], together with other stellar characteristics, gravities, and metallicities. Allowance should also be made for the fact that stars with the same effective temperature but different luminosities and metallicities can have different color indices. We accordingly selected 42 stars from [37] with characteristics close to those of our program stars ($4000 < T_{\rm eff} < 6000$, $1.5 < \log g < 3.0$; the mean metallicity for the selected stars is $[{\rm M/H}] = -0.07 \pm 0.17$). The resulting $T_{\rm eff}$–$(B-V)$ relation is shown in Fig. 5. We approximated the relation using a third-power polynomial; Table 7 presents the approximation coefficients, which can be used to calculate a star's effective temperature from its known $B-V$ color index: $T_{\rm eff} = \sum_{k=0}^{n} A_k c^k$. The $T_{\rm eff}$ values for all the studied stars derived from this calibration are presented in Table 6.

REFERENCES

1. A. A. Boyarchuk, L. I. Antipova, M. E. Boyarchuk, and I. S. Savanov, Astron. Zh. **78**, 349 (2001) [Astron. Rep. **45**, 301 (2001)].
2. A. A. Boyarchuk, Yu. V. Pakhomov, L. I. Antipova, and M. E. Boyarchuk, Astron. Zh. **79**, 909 (2002) [Astron. Rep. **46**, 819 (2002)].
3. L. I. Antipova, A. A. Boyarchuk, Yu. V. Pakhomov, and V. E. Panchuk, Astron. Zh. **80**, 704 (2003) [Astron. Rep. **47**, 648 (2003)].
4. L. I. Antipova, A. A. Boyarchuk, Yu. V. Pakhomov, and V. E. Panchuk, Astron. Zh. **81**, 658 (2004) [Astron. Rep. **48**, 597 (2004)].
5. B. Warner, Mon. Not. R. Astron. Soc. **129**, 263 (1965).
6. S. Udry, M. Mayor, S. Van Eck, *et al.*, Astron. Astrophys., Suppl. Ser. **131**, 43 (1998).
7. D. Hoffleit and M. Saladyga, *Supplement to the Bright Star Catalogue*, 4th ed. (Yale University Observatory, New Haven, 1997).
8. P. K. Lu, Astron. J. **101**, 2229 (1991).
9. J. R. de Medeiros and M. Mayor, Astron. Astrophys., Suppl. Ser. **139**, 433 (1999).
10. R. L. Kurucz, Rev. Mex. Astron. Astrofis. **23**, 181 (1992).
11. C. Sneden, C. A. Pilachowski, and D. L. Lambert, Astrophys. J. **247**, 1052 (1981).
12. A. A. Boyarchuk and L. S. Lyubimkov, Izv. Krymsk. Astrofiz. Obs. **66**, 130 (1983).
13. P. A. Denisenkov and V. V. Ivanov, Pis'ma Astron. Zh. **13**, 520 (1987) [Sov. Astron. Lett. **13**, 214 (1987)].
14. V. E. Panchuk, V. G. Klochkova, and I. D. Naidenov, Preprint No. 135, SAO (Special Astrophysical Observatory, Nizhniĭ Arkhyz, 1999).
15. V. E. Panchuk, M. V. Yushkin, and I. D. Naidenov, Preprint No. 179, SAO (Special Astrophysical Observatory, Nizhniĭ Arkhyz, 2003).
16. V. E. Panchuk, N. E. Piskunov, and V. G. Klochkova, Preprint No. 169, SAO (Special Astrophysical Observatory, Nizhniĭ Arkhyz, 2002).
17. M. V. Yushkin and V. G. Klochkova, Preprint No. 206, SAO (Special Astrophysical Observatory, Nizhniĭ Arkhyz, 2004).
18. A. A. Boyarchuk and L. S. Lyubimkov, Izv. Krymsk. Astrofiz. Obs. **64**, 3 (1981).
19. L. S. Lyubimkov and A. A. Boyarchuk, Astrofiz. **18**, 596 (1982).
20. A. A. Boyarchuk, I. Gubeny, I. Kubat, *et al.*, Astrofiz. **28**, 343 (1988) [Astrophys. **28**, 202 (1988)].
21. T. V. Mishenina and S. A. Korotin, Astron. Zh. **66**, 866 (1989) [Sov. Astron. **33**, 449 (1989)].
22. L. I. Mashonkina, V. V. Shimanskii, and N. A. Sakhibullin, Astron. Zh. **77**, 893 (2000) [Astron. Rep. **44**, 790 (2000)].
23. V. V. Smith, Astron. Astrophys. **132**, 326 (1984).
24. M. J. Harris, D. L. Lambert, and V. V. Smith, Astrophys. J. **292**, 620 (1985).
25. J. Tomkin and D. L. Lambert, Astrophys. J. **311**, 819 (1986).
26. A. McWilliam, Astrophys. J., Suppl. Ser. **74**, 1075 (1990).
27. R. E. Luck, Astrophys. J., Suppl. Ser. **75**, 579 (1991).
28. S. V. Mallik, Astron. Astrophys. **338**, 623 (1998).
29. A. A. Boyarchuk, L. I. Antipova, M. E. Boyarchuk, and I. S. Savanov, Astron. Zh. **77**, 96 (2000) [Astron. Rep. **44**, 76 (2000)].
30. P. E. Nissen and W. J. Schuster, Astron. Astrophys. **326**, 751 (1997).
31. *The Hipparcos and Tycho Catalogues*, ESA SP-1200 (1997).
32. G. Schaller, D. Schaerer, G. Meynet, and A. Maeder, Astron. Astrophys., Suppl. Ser. **96**, 269 (1992).
33. D. Schaerer, G. Meynet, A. Maeder, and G. Schaller, Astron. Astrophys., Suppl. Ser. **98**, 523 (1993).
34. M. Arnould, S. Goriely, and A. Jorissen, Astron. Astrophys. **347**, 572 (1999).
35. A. A. Boyarchuk, L. I. Antipova, M. E. Boyarchuk, and I. S. Savanov, Astron. Zh. **75**, 586 (1998) [Astron. Rep. **42**, 517 (1998)].
36. D. E. Blackwell and M. J. Shallis, Mon. Not. R. Astron. Soc. **180**, 177 (1977).
37. M. L. Houdashelt, R. A. Bell, and A. V. Sweigart, Astron. J. **119**, 1448 (2000).

Translated by N. Samus'

Astronomy Reports, Vol. 49, No. 7, 2005, pp. 548–558. Translated from Astronomicheskiĭ Zhurnal, Vol. 82, No. 7, 2005, pp. 616–627.

The Origin of the Rotational and Spatial Velocities of Radio Pulsars

A. V. Tutukov

Institute of Astronomy, Russian Academy of Sciences, ul. Pyatnitskaya 48, Moscow, 109017 Russia

Received January 15, 2005; in final form, February 17, 2005

Abstract—We analyze possible origins of the observed high rotational and spatial velocities of radio pulsars. In particular, these can be understood if all radio pulsars originate in close binary systems with orbital periods of 0.1–100 days, with the neutron star being formed by a type Ib,c supernova. The high spatial velocities of pulsars (v_p up to 1000 km/s) reflect the high Keplerian velocities of the components of these binaries, while their short periods of rotation ($P_p < 4$ s) are due to the rapid rotation of the presupernova helium-star components with masses of $2.5–10\,M_\odot$, which is synchronous with their orbital rotation. Single massive stars or components in wide binaries are likely to produce only slowly rotating ($P_p > 4$ s) neutron stars or black holes, which cannot be radio pulsars. As a result, the rate of formation of radio pulsars should be a factor of a few lower than the rate of type II and type Ib,c supernovae estimated from observations. This scenario for the formation of radio pulsars is supported by (i) the bimodal spatial velocity distribution of radio pulsars; (ii) the coincidence of the observed spatial velocities of radio pulsars with the orbital velocities of the components of close binaries with nondegenerate helium presupernovae; (iii) the correlation between the orbital and rotational periods for 22 observed radio pulsars in binaries with elliptical orbits; and (iv) the similarity of the observed rate of formation of radio pulsars and the rate of type Ib,c supernovae. © *2005 Pleiades Publishing, Inc.*

1. INTRODUCTION

Neutron stars were predicted theoretically on microphysical grounds as far back as the 1930s; later, Baade and Zwicky [1] suggested that they may originate in the course of supernova outbursts. In 1967, the first radio pulsar was detected [2], and proved to be a young neutron star (NS) [2]. This discovery led to studies of three fundamental theoretical problems: explaining the extremely high magnetic fields ($\sim 10^{12}$ G), high spatial velocities (v_p to 1000 km/s), and rapid rotation ($P_p \sim 1$ s) of radio pulsars. The high magnetic fields were explained by suggesting that the initial stellar field was frozen into the collapsing core of the supernova [3]. The rapid rotation was understood as a consequence of the conservation of some fraction of the core angular momentum. The very high spatial velocities were more difficult to interpret. Shklovskii [4] suggested that a young neutron star acquires a several-hundred km/s "kick" velocity due to the asymmetry of the supernova explosion (or its neutrino radiation), which may come about due to the regular magnetic field and/or large-scale turbulence generated during the explosion.

Neutrino radiation that is directional and asymmetric relative to the center of the star carries away an energy $\sim 0.1\,M_{NS}c^2 \sim 2 \times 10^{52}$ erg, and can therefore efficiently speed up both the rotational and spatial motions of a young neutron star [5, 6]. In the case of a one-sided ejection of neutrinos, the spatial velocity of the young neutron star should be ~20 000 km/s, and the rotational period ~0.001 s, as follows from the conservation of angular momentum, assuming that the neutrinos are radiated instantaneously from a point on the equator of NS. In reality, young radio pulsars move with velocities that are lower by a factor of ~100, and their rotational periods are a factor of 100–1000 longer. One possible reason for the low efficiency of the neutrino kick may be the rotation of the young neutron star. The direction of the radiation will vary during the rotation, decreasing the efficiency of the acceleration. Assuming that the duration of the neutrino burst in a supernova explosion is 1 s [7, 8], the spatial velocity of a young neutron star will be related to its rotational velocity as $v_p = 20\,000\,P_p$ km/s. Note that a reasonable velocity $v_p = 300$ km/s [9] follows if the energy of the pulsar's rotation and of its spatial motion are equal when $P_p = 0.2$ s. However, it remains unclear whether the magnetic field of a young neutron star is strong enough to yield a sufficient neutrino kick and if its configuration can accelerate the rotation. At the same time, it is clear that the presence of a regular magnetic field can facilitate deviations of a supernova explosion from axisymmetry, resulting in both a high velocity and rapid rotation for the young neutron star.

Here, we consider a scenario in which both the spatial and rotational velocities of radio pulsars are

1063-7729/05/4907-0548$26.00

a result of their formation during SN Ib,c explosions in close binaries in which the rotation of the helium supernova progenitor is synchronous with the orbital motion. The assumption that the binary components retain some of their high orbital velocities can explain the resulting high spatial velocities ($v_p \sim$ to 1000 km/s). The rotation velocities of observed pulsars are specified by two factors. The rapid ($P_p \sim$ 0.01–1 s) initial rotation of the collapsing degenerate helium core of the supernova, which rotates synchronously with its orbital motion before the explosion, is due to the conservation of angular momentum. The most likely reason for the acceleration of the rotation of the most rapid neutron stars, which form from the primary components of massive binaries, is the accretion of some fraction of the common envelope that originates during the evolution of their massive companions.

A special group of pulsars contains single and binary millisecond pulsars with $P_p \sim 0.001$–0.01 s. There is little doubt that the rotation of these pulsars has been accelerated during an extended stage of disk accretion of matter from a solar-mass companion in a semi-detached binary [10–12]. The donors of millisecond pulsars have either been totally evaporated by the pulsar's X-ray radiation or remain in the form of, most likely, degenerate helium dwarfs that are gravitationally bound to the pulsars [12]. The large number of such pulsars in globular clusters with low escape velocities (<50 km/s) suggests that a substantial fraction of young neutron stars receive only a small kick velocity when they are born.

2. CORRELATION BETWEEN OBSERVED SPATIAL AND ROTATIONAL VELOCITIES OF SINGLE RADIO PULSARS

Observed single radio pulsars rotate with periods of 0.1–4 s [13, 14], usually explained by the partial conservation of the angular momentum of the presupernova or asymmetry of the neutrino radiation of the supernova [5, 6]. The observed distribution of the distances of radio pulsars from the Galactic plane and studies of their proper motions revealed high spatial velocities [15–18]. When these velocities were analyzed in detail, taking observational selection effects into account, two populations of pulsars were suspected: slow pulsars with $v_p < 100$ km/s and fast pulsars with $v_p \sim 200$–400 km/s [19]. The birth rates of both populations appeared to be similar. This bimodality of the distribution of initial spatial velocities of radio pulsars was recently confirmed on the basis of extended observational material [20]. The numbers of objects in each group appeared to be similar, although these estimates remain uncertain (at least, within a factor of two), since reconstruction of the initial distribution involves several parameters that are not well known. The presence of slow pulsars is supported, for example, by the simple fact that the average velocity of 21 pulsars located within ~500 pc of the Sun is ~100 km/s [17, Table 4]. In addition, the presence of binary pulsars with $P_{\rm orb} \sim 100$ days requires that a substantial fraction of pulsars acquired kick velocities of less than 100 km/s [21].

We used the catalog [17] to analyze v_p and P_p, which can be used to derive the distribution of the tangential components of the spatial velocities of radio pulsars v_t based on their proper motions and P_p. The observed P_p values lie between 0.01 and 4 s, while v_t lies between 6 and 1000 km/s. It is clear that v_t provides a lower bound for v_p, while P_p provides an upper bound, since the rotation of pulsars decelerates with time. Unfortunately, additional uncertainty in the estimates of the pulsar velocities is introduced by uncertainty in the distance scale.

Let us consider possible origins for the observed rotational velocities and fast spatial motions of radio pulsars. The massive stars that are neutron-star progenitors rotate with equatorial velocities ~300 km/s, or periods $P \sim 1$ day [22]. If we assume that the core of a massive star evolves into a neutron star conserving its angular momentum, then $P_p \sim \rho^{-2/3}$, where ρ is the average density, and the rotational period of a young neutron star should be $\sim 10^{-4}$ s. It is obvious that the loss of angular momentum from the core of the massive star during its evolution must be taken into account when estimating P_p. The fact that the angular momenta of stellar cores can be efficiently transferred to their envelopes is confirmed by observations of Be stars, in which this transfer keeps the surface rotation critical during almost the entire period of hydrogen burning in their cores [23–25]. There are some additional arguments suggesting that rigid-body rotation is maintained in stars, at least on the main sequence [26]. It is possible, for example, that the magnetic field may decelerate the core rotation of massive stars by almost a factor of 50 in the course of their evolution [22]. For radio pulsars, this would mean that their characteristic initial rotational period should be around 0.01 s. However, the catalog [17] indicates that virtually no radio pulsars with such short periods exist.

It is certainly possible that the magnetic field inside a star is sufficient to keep the rotation of the star close to rigid-body rotation over the entire period of its evolution [27]. This possibility is supported by the recently detected strong magnetic fields in sdB and sdO stars [28], which are essentially the naked helium cores of components of close binaries with initial masses 2.5–25 $M_\odot$ [29]. Strong magnetic

fields (10 000–200 000 G) have also been found in degenerate dwarfs. These are, to some extent, analogous to the degenerate cores of the presupernovae that result in the formation of neutron stars [30, 31]. Assuming conservation of their angular momentum, the observed equatorial velocities of 0.6 km/s for white dwarfs [32] imply equatorial velocities for their main-sequence progenitors of ∼6 m/s, almost a factor of 700 lower than even the equatorial velocity of the slowly-rotating Sun. Some degenerate dwarfs (GD 356) display higher velocities, ∼2–6 km/s [33, 34]. However, even these are not sufficient to reproduce the observed rotational velocity of the Sun. These facts support the possibility that there is an efficient transfer of angular momentum from the stellar cores to the envelopes. If we assume that a single massive star maintains its rigid-body rotation up until the supernova, when it has a radius of $\sim 1000\,R_\odot$ and an average presupernova core density of $\sim 5 \times 10^7$ g/cm^3, the young neutron star will rotate with a period of ∼6 h, which is four orders of magnitude higher than the characteristic observed rotational periods of radio pulsars. It is obvious that the typical rotational periods of pulsars (∼0.3–1 s) are far from these limits—0.0001 s and 6 h, and that they correspond to a loss of ∼0.9999 of the initial specific angular momentum of a massive star's core. The reason why the cores of single stars—provided they are, indeed, the progenitors of observed radio pulsars—lose so much angular momentum remains unknown.

There are basically two scenarios for the acceleration of the spatial motion of a young neutron star. The first suggests that the supernova explosion that gives birth to the pulsar is asymmetrical [4]. Supernova envelopes are generally asymmetrical; a ten-percent asymmetry is sufficient to produce observed several-hundred-km/s velocity for the young neutron star [8]. However, this velocity is model-dependent, and cannot currently be reliably derived even using two- or three-dimensional gas-dynamical models. The other scenario suggests asymmetry of the supernova's neutrino radiation. If the neutrino ejection is one-sided, this simple mechanism is able to accelerate the neutron star to ∼20 000 km/s. However, such velocities are not observed, implying that the efficiency of the mechanism is much lower. A young neutron star is sometimes assumed to undergo rotational breakup, with the evaporation of the less massive component [35]; this model requires near critical rotation for all young neutron stars, which has not been observed.

Let us consider how the rotation of a young neutron star decreases its spatial velocity in the presence of one-sided neutrino emission. In this case, the neutron star moves along an unwinding spiral, with its spatial velocity being specified by the impulse obtained from the neutrinos over approximately half its rotational period. If the duration of the neutrino burst is ∼2 s [8, 22], we will obtain $v_p < 10\,000\,P_p$ km/s. Formally, all observed single radio pulsars [17] meet this condition. However, this mechanism implies the existence of slowly rotating pulsars with periods of 0.14 to 4 s and spatial velocities of 1000 to 30 000 km/s, which have not been observed. If we assume that the fraction of directed neutrinos is small (∼0.03), this difficulty will be removed. However, the reasons for this efficiency and for the observed bimodality of the observed v_p distribution for radio pulsars [19, 20] remain unclear.

Previously, we suggested [19, 29] that both the spatial velocities and the bimodality of the spatial-velocity distribution for radio pulsars could be understood if radio pulsars formed in massive close binaries, which, as a rule, are disrupted after the explosion of the secondary. Modeling using a scenario program for the v_p distribution [36–38], which can describe the evolution of any type of binary, enabled us to derive in general terms the observed spatial velocity distribution for radio pulsars. In particular, two roughly equal populations of young neutron stars were obtained, with characteristic velocities $v_p \sim 20$ km/s and $v_p \sim 200$ km/s; in addition, the estimated maximum spatial velocity of the radio pulsars coincided with the observed value (∼1000 km/s). In the following section, we will present arguments suggesting that both the spatial velocities and the initial rotational velocities of radio pulsars are associated with their formation in massive close binaries. This becomes possible if a sdB or sdO helium subdwarf presupernova is a component of a close binary containing a presupernova and rotates synchronously with the orbital motion of the system.

If both the spatial velocity and rotation of a radio pulsar are determined by the orbital motion of binary components, and the rotation of their helium progenitors is synchronized with their orbital motion, the orbital velocity of the components and the rotational velocity of the pulsar should be related. Let us suppose that the mass of a presupernova component is M, while the mass of its companion in a circular orbit is m. Then, for a young pulsar, v_p and P_p will be related by the simple expression

$$P_p = 10^{-6}\frac{2\pi G m^3}{v_p^3 (m+M)^2}, \qquad (1)$$

where G is the gravitational constant, or

$$P_p = 8.4 \times 10^5 \frac{m^3}{v_p^3 (m+M)^2} \quad \text{s}, \qquad (2)$$

where v_p is given in km/s and the masses of the components are in solar units. We will take P_p to be a factor of 10^6 shorter than the orbital period of the presupernova, since the radius of the supernova's core decreases by a factor of almost 1000 during its collapse to a neutron star (see Section 3).

If we adopt $m = 1.3\,M_\odot$ and $M = 3.9\,M_\odot$ as characteristic values, it follows from the last equation that young neutron stars forming in such systems should have $v_p = 40$–200 km/s and $P_p = 0.03$–2 s. A presupernova in a massive close binary is a helium star with a radius close to that of a main-sequence helium star: $R_{\rm He} = 0.2(M_{\rm He}/M_\odot)^{0.6}$ [39]. This constrains the minimum semimajor axis, and hence the maximum spatial velocity and minimum P_p that can be reached in this way. For $M = 3.9\,M_\odot$ and $m = 1.3\,M_\odot$, the maximum velocity is $\sim$250 km/s, and the minimum rotational period is $P_p \sim 0.004$ s. Increasing the mass of the supernova companion to $10\,M_\odot$ (a black hole) may increase the spatial velocity of the young pulsar to some extent; however, black holes are rare. Note that (1) specifies the minimum velocity, since it coincides with the velocity gained by the center of mass of the system when the minimum condition for its disruption is fulfilled: $M - M_{NS} = M_{NS} + m$. Since the components acquire parabolic orbits in this case, their relative velocities at infinity are equal to zero. Naturally, the spatial velocities of the components are then equal and coincide with the velocity of the center of mass of the system after the supernova explosion and the formation of the neutron star [see (1)].

The catalog [17] also demonstrates the existence of about ten pulsars with $P_p \sim 0.2$–0.4 s and velocities $v_t \sim 10$ km/s, appreciably smaller than is obtained from (2). Indeed, there exists abundant information on slow pulsars in close binaries. Such systems are formed when a close binary with a high initial mass ratio is disrupted during the first supernova explosion in the system. In this case, (2) can be rewritten

$$v_p\,[\mathrm{km/s}] = 94\frac{m}{M_\odot}\left(\frac{M}{M_\odot}+\frac{m}{M_\odot}\right)^{-2/3} P_p^{-1/3}. \quad (3)$$

This formula clearly indicates that, for a specified P_p, a small v_p will be obtained if the masses of the companion and the helium supernova itself are small. Naturally, the simple condition $M > 2\,M_{NS} + m$ must still be fulfilled for the disruption of a system with circular orbits. With $M = 10\,M_\odot$ and $m = 0.3\,M_\odot$, formula (3) yields $v_p \sim 10$ km/s for $P_p \sim 0.3$ s. This scenario can explain the existence of the pulsars with the smallest observed spatial velocities ($\sim$10 km/s). To estimate the fraction of such pulsars, we will assume, following [39], that the star-formation function in our Galaxy is $dN/dM_1 \sim (M_\odot/M_1)^{-2.5}$/yr, and that $dN/dq = 1$ for close binaries (q is the initial component-mass ratio in the system of two main-sequence stars). The rate of occurrence of binaries with $10 < M_1/M_\odot < 25$ whose primaries produce neutron stars after SN Ib,c explosions will be $\sim$0.0157/yr. The disruption of a system requires that $M_{\rm He} = 0.1(M_1/M_\odot)^{1.4} > 2N_{NS} + m$, or $m/M_\odot < 0.1(M_1/M_\odot)^{1.4} - 2(M_{NS}/M_\odot)$. The latter condition can be translated into a simple restriction on the initial component-mass ratio in the system if we assume that, given the high component-mass ratios in such systems, we can neglect the accretion of common-envelope material onto the low-mass secondary in the common-envelope phase:

$$q < 0.1(M_1/M_\odot)^{0.4} - 2\,M_{NS}/M_1. \quad (4)$$

We can see that the initial component-mass ratio q varies from zero for $M_1 = 10\,M_\odot$ to $\sim$0.26 for $M_1 = 25\,M_\odot$. Integrating the above initial mass distribution for the primaries yields a rate of formation of systems in our Galaxy that are disrupted in their first explosion of $\sim$0.0035/yr, or about 10% of all neutron-star-producing binaries. This estimate is confirmed by modeling [36]. Thus, the disruption of a massive close binary with a high initial component-mass ratio during the explosion of the primary is fairly common, and can explain the existence of single radio pulsars with $v_p \sim 10$ km/s.

It follows from (1) that, when the system is disrupted by the second supernova explosion, the velocities of the young neutron stars that form during these supernovae will be 40–200 km/s. This coincides with the values observed for slow radio pulsars [19, 20]. The velocities of the fastest pulsars remain outside the range of those estimated for neutron stars produced by second supernova explosions. However, it is clear that, when a system is disrupted after the second explosion, the neutron star that was initially formed from the primary should acquire velocities a factor of three to seven higher, depending on the component-mass ratio at that time. That provides a mechanism for the formation of "fast" radio pulsars with velocities 100–1000 km/s [37, Fig. 10].

One can ask, however, whether the neutron stars produced from the primaries can rotate rapidly enough to become radio pulsars. The example of neutron stars in close binaries with Be stars provides evidence that the rotation of these neutron stars can be decelerated to $P_p \sim 4$–1000 s due to their motion in the Be-star wind [40, 41]. It seems possible that the rotation of these neutron stars can be accelerated to the required velocities of $P_p <$

4 s [36] due to accretion in the common-envelope phase that is experienced by all old neutron stars in such systems. The duration of the common-envelope stage is close to the thermal timescale of the secondary, when it fills its Roche lobe—$\sim 3 \times 10^7 (M/M_\odot)^2 (R_\odot/R)(L_\odot/L)$ years. The luminosity of a massive star is proportional to the square of its mass: $L/L_\odot = 100(M/M_\odot)^2$. Restricting the accretion rate for a neutron star in the common-envelope stage to the Eddington limit, $\sim 10^{-8}\, M_\odot$/yr, we find that the rotational period for an "old" neutron star will be $P_p \sim 0.08 a/R_\odot$ s, and its spatial velocity after the disruption of the system $v_p = 440(M/M_\odot)(R_\odot/a)^{1/2}$ km/s, where a is the final semimajor axis of the system after the common-envelope stage in solar radius units. As a result, the rotational period P_p will be related to the spatial velocity v_p as

$$v_p = 130((M/M_\odot)/P_p)^{1/2}. \quad (5)$$

If $M = 4\, M_\odot$, we obtain $v_p = 260\, {P_p}^{-1/2}$ km/s. It is clear that, with $P_p \sim 0.06$–4 s, the velocities of "old" neutron stars can indeed completely overlap the interval of observed velocities (100–1000 km/s) for the fastest radio pulsars. Note, however, that estimates of the rotational velocities of "old" neutron stars after the common-envelope stage remain uncertain due to uncertainty in the accretion efficiency during this stage. It is important that the maximum v_p derived directly from the size of the helium presupernova can be reliably determined, and coincides with the observed value of $v_p \sim 1000$ km/s. This velocity is obtained, for example, for the disruption of a system in which $M_{\rm He} = 10\, M_\odot$, the radius of the helium star is $\sim 0.8\, R_\odot$, and the mass of the old neutron star is $\sim 1.3\, M_\odot$. The disruption of a system after the second supernova results in the formation of a young pulsar with $v_p = 40$–200 km/s and an old pulsar with $v_p = 150$–1000 km/s. Detailed studies of the apparent motions of radio pulsars have been used to find pairs of pulsars that may have been formed during the disruption of close binaries after their second supernova. One example is the pulsars B2020+28 and B2021+51, whose ages are both $\sim 2 \times 10^6$ yrs [42]. The existence of such objects provides evidence that the rotation of an old neutron star can be accelerated to a "plausible" velocity during the common-envelope stage. Another strong argument supporting such acceleration is provided by the existence of a binary radio pulsar with rotational periods for the old and young pulsar of $P_p \sim 2.77$ s and ~ 0.023 s for $p_{\rm orb} = 2.4$ h [43]. As we will show in the next section, the rotational period of the millisecond component is probably determined by the orbital rotation of the system, while the rotational period of the other component is determined by accretion during the previous evolutionary stage of the system. The above formulas can be used to estimate the orbital parameters of the system before its common-envelope stage, given the velocity of its spatial motion, ~ 100 km/s: the semimajor axis is $\sim 25\, R_\odot$, and the mass of the progenitor of the millisecond pulsar is $\sim 10\, M_\odot$.

Accretion in a common-envelope stage is important in another interesting case of the evolution of close binaries. It has been estimated that a carbon–oxygen (oxygen–neon) degenerate dwarf whose initial mass is close to the Chandrasekhar limit can reach this limit due to hydrogen and helium burning in layer sources in the common-envelope stage. This will result in an unusual supernova explosion, which—like SN Ia explosions, which are due to the same mechanism—will not leave any remnant in the case of a carbon–oxygen dwarf. However, the spectrum of the envelope of such a supernova should display hydrogen lines corresponding to the common envelope.

Thus, in the absence of a appreciable kick and supposing that all observed radio pulsars were formed in massive close binaries, there exist three groups of radio pulsars with different prior evolutions and characteristic spatial velocities. The slowest group ($v_p <$ 30 km/s) includes around 10% of all radio pulsars, and originates due to the disruption of massive close binaries with high initial component-mass ratios [44]. The "need" for this group is demonstrated by the presence of numerous millisecond pulsars in globular clusters. For example, about 30 such radio pulsars have already been found in 47 Tuc [45, 46]. The second group, with intermediate spatial velocities (40–200 km/s), includes the products of the explosions of the secondaries in neutron-star (degenerate dwarf) + sdB, sdO systems. Finally, the fastest pulsars, with velocities of 100–1000 km/s, which comprise half of all pulsars, are produced by the evolution of the primaries in massive close binaries. Their rotation has probably been accelerated in a common-envelope stage preceding the explosion. Unfortunately, estimates of the rotational velocities of these neutron stars remain uncertain.

There may exist another group of slow radio pulsars that are produced by Thorne–Zhytkov objects, i.e., supergiants with neutron cores [44]. However, uncertainty in the intensity of the stellar wind, which specifies their lifetime, and, hence, in the efficiency of the accumulation of matter and the acceleration (deceleration?) of the rotation of the neutron cores of these stars, hinder quantitative studies of this scenario.

3. CORRELATION BETWEEN OBSERVED ROTATIONAL AND ORBITAL VELOCITIES OF RADIO PULSARS IN CLOSE BINARIES WITH $e > 0.05$

There exist two types of pulsars, i.e., rotating neutron stars, for which the hypothesis that their rotational velocities are associated with their orbital motion in a binary can be directly verified from observations. These are radio pulsars in close binaries with elliptical orbits and invisible compact companions and accreting neutron stars in close binaries with Be stars [40]. The correlation between the rotational and orbital periods of these pulsars can be analyzed. A high orbital eccentricity provides evidence that there was a supernova in the system, and, in the absence of a kick, is a measure of the mass lost by the system in the explosion: $e = \delta M/M_R$, where δM is the mass lost by the supernova and M_R is the total mass of the remaining components. This makes it possible to estimate the orbital period and semimajor axis $a_0 = a(1-e)$ of the binary at the moment of the supernova explosion (and the formation of the neutron star). Thus, the initial orbital periods of the systems can be reconstructed.

To estimate the rotational period of a pulsar P_p theoretically, we assume that the radius of the presupernova core that collapses into the neutron star is $\sim 10^9$ cm, while the radius of the neutron star is 10^6 cm. This core radius corresponds to the size when carbon has been exhausted in the core [22, Table 2]; after this stage, the angular momentum of the collapsed core essentially does not vary up to the formation of the neutron star [22, Table 1]. In addition, we assume that the rotation of the helium presupernova when the carbon in its core is depleted was synchronous with its orbital motion. The conservation of angular momentum then yields:

$$P_p = 10^{-6}\, P_{\rm orb}. \qquad (6)$$

All the presently known 24 radio pulsars in close binaries with high orbital eccentricities ($e > 0.05$) and invisible companions [43, 47–57] were used to estimate the orbital periods of the systems at the moment of their supernovae. As a rule, the masses of the companions of the observed radio pulsars in close binaries are unknown; however, knowledge of the orbital eccentricity is sufficient for determining the initial orbital period P_0 [58]. We obtain

$$P_0 = P_f(1-e)^{1.5}(1+e)^{-0.5}, \qquad (7)$$

where P_f is the observed orbital period of the system. The mass of the helium progenitor of the neutron star is ~ 2.5–$10\, M_\odot$ [59]. For $P_p \sim 0.003$–1 s, the 24 systems with radio pulsars display an obvious correlation between the initial orbital period and the current rotational periods of pulsars in systems with elliptical orbits, first noted for a smaller number of stars [58]. For the median $P_p \sim 0.04$ s, the median $P_0 \sim 0.63$ d essentially coincides with the value predicted by (6). The remaining dispersion of this correlation within a factor of three could be due to the dispersions of the masses and the magnetic-field intensities of the collapsed cores of supernovae, and hence of the subsequent decelerations of the rotations of the young neutron stars that are formed.

The correlation between the orbital motions and rotations of neutron stars in systems containing Be stars and accreting pulsars [40, 41, 60, 61] is also of considerable interest. All Be stars in such systems belong to the narrow range of spectral types 09.5 to B2V, which corresponds to main-sequence stars with masses of 12–$15\, M_\odot$. Most of these stars display appreciable orbital eccentricities, 0.12–0.9 [40]. In the absence of a kick and with a circular initial orbit, such eccentricities correspond to a substantial mass loss in the supernova: 1–$10\, M_\odot$. That is precisely what is expected for the formation of neutron stars in massive close binaries [62]. The values of P_p, $P_{\rm orb}$, and e have been determined for 25 Be + NS systems in the Galaxy [40]. The periods P_p lie in the range 0.1–1000 s, while $P_{\rm orb}$ lies between 1 and 250 days. For systems with known orbital eccentricities, we can derive the orbital periods at the moment of the supernova in these binaries using (7).

Relation (6) is also obeyed by Be + NS systems, and represents a lower bound for the range of P_p for these pulsars. The only system that may not agree with this relation is A0538-7, with $P_{\rm orb} = 16.7$ d and $P_p = 0.069$ d, which has a high ($e > 0.5$) but unknown eccentricity, hindering reliable estimation of P_0 for this system. Analysis of the Be + NS systems indicates that virtually all the pulsars in these systems rotate more slowly than is predicted by (6) relating the rotational and orbital periods. The reason for the slow rotation of the neutron stars in these systems is their deceleration in the stellar wind of the Be stars [60, 63, 64]. The characteristic time scale for this deceleration ($\sim 10^6$ yrs) is shorter than the lifetime of the Be components on the main sequence ($\sim 10^7$ yrs). Therefore, the rotation of these neutron stars can be appreciably slowed during the lifetime of their Be companions. However, what is important for us here is the fact that the lower bound for the range of rotational periods of pulsars in Be + NS systems essentially coincides with the condition $P_p = 10^{-6}\, P_{\rm orb}$, suggesting an orbital origin for the initial rotational periods of these pulsars as well. Note that the orbital periods of all systems with radio pulsars before NS formation are shorter than ~ 100 days, which may

be necessary for synchronicity of the orbital and rotational motions of the helium presupernovae, and, hence, for high initial rotational velocities for these neutron stars.

Modeling of the evolution of close binaries [44] does not rule out the existence of even wider Be + NS systems. One possible explanation for the absence of pulsars in systems wider than the observed systems may be that the kick received by the young neutron star exceeds the escape velocities of such binaries. We can easily estimate that the disruption of a Be + NS system with $P_{\rm orb} > 100$ days and a mass for the Be star of $12-15\,M_\odot$ [65] requires a kick exceeding $\sim$100 km/s. Note, however, that a "universal" kick with this value would result in higher orbital eccentricities for Be + NS systems, which would increase with their orbital periods. No correlation of this type is seen, and the observed orbital eccentricities in Be + NS systems [40] can be explained by spherically symmetrical supernovae, at least in systems with known component masses and orbital eccentricities, such as the high-eccentricity Be + NS systems 4U 0115+63 ($e = 0.34$, $M_{\rm Be} = 17\,M_\odot$ [40], $\delta M = 6.2\,M_\odot$), EXO 2030+34 ($e = 0.41$, $M_{\rm Be} = 18\,M_\odot$ [40], $\delta M = 8\,M_\odot$), and GRO J1008-57 ($e = 0.66$, $M_{\rm Be} = 18\,M_\odot$ [40], $\delta M = 12\,M_\odot$). Such masses for the helium neutron-star progenitor correspond to main-sequence stars with $\sim 25-30\,M_\odot$, which coincides with the estimated maximum initial mass for stars that can produce neutron stars [59]. Be + NS systems with lower orbital eccentricities ($\sim$0.1) would lose $\sim 1.5\,M_\odot$ in their supernova explosions, which corresponds to a mass for their helium progenitors of $\sim 2.8\,M_\odot$, or an initial mass for the main sequence stars of $\sim 10-12\,M_\odot$. This value coincides with the limiting mass between stars producing neutron stars and degenerate dwarfs. Therefore, the observed orbital eccentricities of Be + NS systems can be explained with ordinary spherically symmetrical SN Ib,c explosions, without a appreciable kick.

The orbital periods of known Be + NS systems [40, 41] exceed $\sim$2 days. It is clear that they are limited by the sizes of the Be stars, which exceed the sizes of ordinary main-sequence stars by a factor of two to three due to their rapid rotation [64]. The maximum orbital period of these systems is $\sim$100 days. This is close to the maximum orbital periods of radio pulsars in binaries with eccentric orbits. Scenario modeling of the evolution of massive binaries does not rule out even wider Be + NS or NS + NS-type systems (with the companion possibly also being a black hole or degenerate star) [44]. However, synchronization of the rotation and orbital motion of the helium presupernova is probably not possible in these systems. As a result, the young neutron stars they produce rotate too slowly to become radio pulsars in NS + NS systems. In the case of Be + NS systems, the accretion rates in such wide systems are too small to form a bright X-ray pulsar.

Summarizing our analysis of the observed correlation between the rotational and orbital periods of neutron stars in close binaries, we conclude that the orbital rotations of the helium presupernovae probably play the dominant role in determining the initial rotational velocities of young neutron stars. These two motions can be synchronized only in systems with $P_{\rm orb} = 0.1-100$ days. The rarity of binary radio pulsars (so far, only one is known) could be due to several factors: the companion of the radio pulsar may be a degenerate dwarf, black hole, or neutron star that was not sufficiently spun up in the common-envelope stage, or the rotational axes of the two radio pulsars may not coincide.

4. CONCLUSION

Most supernovae result in the formation of a neutron star. Rare exceptions are SN Ia explosions, which leave no remnant and have a relative rate of occurrence of $\sim$0.1, and explosions of stars with initial masses exceeding $\sim 25-30\,M_\odot$, which have the same relative rate of occurrence and result in the formation of black holes [66]. It is important, however, that there is no unambiguous relation between supernova remnants and radio pulsars. In their analysis of 17 young radio pulsars with ages less than 20 000 years, Kaspi and Helfand [67] found that 10 were associated with supernova remnants. In addition, as a rule, supernova remnants are not associated with radio pulsars, in spite of the long lifetime of the latter. Only 10 radio pulsars were found in 200 remnants [68]. This is partially due to the narrowness of the radio beams and high velocities of radio pulsars; however, the main factor is that common (as a rule type II) supernovae are unlikely to produce radio pulsars.

Evidence for this is directly provided by empirical estimates for the rates of supernovae and of the formation of radio pulsars. In the Galaxy, the formation rate of pulsars is 0.001–0.006/yr [20, 69, 70], while the rate of type II supernovae, which produce neutron stars, is 0.015 to 0.03/yr [36, 69–72]. The observed rate of SN Ib,c, which give rise to rapidly rotating neutron stars/radio pulsars in close binaries, is $\sim$0.006/yr [73–75]. This rate is only $\sim$20% of the rate of type II supernovae in spiral galaxies with active star formation, but it is close to the observed formation rate of radio pulsars [20, 69, 70]. This provides an additional argument that radio pulsars mainly form during the evolution of close binaries with initial component masses of $10-25\,M_\odot$ and periods of $0.1 <$

$P_{\rm orb} < 100$ days. In the case of Keplerian orbits, this interval of orbital periods corresponds to semimajor axes a of $\delta \log a/R_\odot \sim 2$. Assuming that the transformation of the semimajor axes in the common-envelope stage is linear [29] and that the initial distribution of the semimajor axes in binaries is $dN = 0.2d \log a/R_\odot$ in the interval $1 < \log a/R_\odot < 6$ [29], we find that the formation rate of radio pulsars is ~40% of the SN II rate. This estimate is close to the observed SN Ib,c rate relative to the SN II rate [36, 69, 71–75].

Let us imagine what the immediate progenitor of a typical radio pulsar may be like. There are two possibilities. The first is a helium star with a mass of 2.5–10 $M_\odot$ that is an sdB(sdO) component in a close binary with an orbital period of 1 h to 100 days. The second is a neutron-star companion of such a helium presupernova whose rotational period has been sped up to $P_p = 0.3$–3 s in a common-envelope stage. Observationally, most sdB and sdO stars are in close binaries with orbital periods of 0.1–100 days [76–78]. Of course, most observed sdB,sdO stars have masses smaller than a solar mass, and they do not have the intense stellar winds that are typical of Wolf–Rayet stars with masses exceeding 10 $M_\odot$ [66]. The winds of Wolf–Rayet stars are probably maintained by pulsations [79]. Pulsations with small amplitudes have been detected in some sdB stars, but their mass-loss rates do not exceed 10^{-14}–10^{-12} $M_\odot$/yr [80, 81]. This weak wind is not able to slow the rotation of a neutron-star companion (future rapid radio pulsar) or to remove the remaining hydrogen in the sdB or sdO stars observed in SN Ib,c by the time of the supernova explosion [82].

Some systems will remain gravitationally bound after the supernova of an sdB or sdO subdwarf and the formation of a neutron star without a large kick. Let us estimate the fraction of binary radio pulsars based on our scenario for the evolution of massive binaries. According to the model [36], only ~0.034 of neutron stars are in NS + NS, COd + NS, ONed + NS, and BH + NS systems. Here, COd and ONed denote carbon–oxygen and oxygen–neon degenerate dwarfs and BH a black hole. Precisely such systems should display substantial orbital eccentricities, $e > 0.1$, due to rapid mass loss during the supernova. However, about 0.01 of observed pulsars are binary, taking into account only systems with $e > 0.1$ [69]. The difference between these values may be due to residual uncertainties in these two estimates. Binarity of radio pulsars may be difficult to detect, for example, due to observational selection effects. The theoretical estimate based on our scenario likewise contains some uncertainty. In particular, the scenario predicts the existence of single neutron stars that have gone through a stage as a Thorne–Zhytkov object [36]. However, it remains unclear whether they will be able to accumulate a sufficient amount of matter to accelerate their rotation to $P_p < 4$ s in this stage.

The condition for a binary with a circular orbit to be disrupted by a supernova in the system is $\delta M > 2\,M_{NS} + M_2$, where δM is the mass lost in the explosion and M_2 is the mass of the companion. The observed masses of young neutron stars are ~1.3 $M_\odot$ [43, 83, 84]. Therefore, the disruption of an NS + NS system requires that the mass of the supernova precursor at the moment of the explosion exceed ~3.9 $M_\odot$. The current estimate for the minimum mass of a helium star that can produce a neutron star is 2.5–3 $M_\odot$ [39]. However, taking rotation into account increases the mass of the helium core of the star, and, hence, the mass of the presupernova. This will lead to a decrease in the fraction of neutron stars that are binary. There is no need for all systems to be disrupted; the observed total fraction of binary radio pulsars is currently ~0.2 [86], primarily due to the effect of long-lived pulsars that are "rejuvenated" by accretion [10–12], and this fraction is increasing with time.

Our analysis of possible origins of the high spatial and rotational velocities of radio pulsars has yielded a list of advantages and disadvantages for the two basic explanations for these phenomena: asymmetry of supernova explosions and the disruption of close binaries. The latter is consistent with the observed excess of the SN II rate over the rate of formation of radio pulsars, with the latter being close to the SN Ib,c rate. It can also explain the bimodality of the observed spatial velocity distribution for radio pulsars; the maximum spatial velocity of radio pulsars, ~1000 km/s; and the observed correlation, $P_p \sim 10^{-6}\,P_{\rm orb}$, for 24 systems with orbital eccentricities exceeding 0.05. The main problem with the hypothesis that this is the sole mechanism giving rise to the high spatial velocities and rapid rotation of radio pulsars is the relatively high theoretical estimate of the fraction of radio pulsars that should be binary, which exceeds the observed value. However, this comparison is unclear due to uncertainties in both the theoretical and observed values.

The asymmetry of neutrino radiation during supernovae, which would give the formed pulsar a "kick," provides the fundamental possibility for pulsars to acquire velocities of ~400–500 km/s [88]. However, this scenario cannot explain the restriction of the maximum observed kick velocity to ~1000 km/s, the lack of a correlation between the magnetic-field strength and the kick velocity [89], the discrepancy between the rate of SN II and the rate of formation of radio pulsars, the origin of the

observed rotational velocities of radio pulsars, the origin of the correlation between P_p and $P_{\rm orb}$ for binary radio pulsars with eccentric orbits, or the observed bimodality of the kick velocities. Overall, the disruption of close binaries currently seems more plausible as the main origin for the rapid rotation and high spatial velocities of radio pulsars. However, there is no reason to think that the initial kick velocity is equal to zero, or that a real supernova should be perfectly symmetrical. Naturally, a supernova will not be perfectly symmetrical, and the magnetic field in the supernova core and large-scale turbulence will certainly impart some spatial velocity and rotation to the young neutron star that is formed. The task of both theory and observations is to estimate these factors [90]. It is obvious, for example, that a kick velocity of $\sim$100 km/s would lead to the disruption of all wide binaries.

The role of close binaries in accelerating the spatial motions of neutron stars, black holes, and main-sequence stars is not confined to the examples we have considered, which are ultimately based on the mechanism suggested by Blaaw [91]. It follows from the conditions required for the formation of supermassive black holes in the cores of globular clusters and galaxies that the cores of merging galaxies may form binary supermassive black holes. Before merging, their orbital velocities can become comparable to the velocity of light. Neutron stars and stellar black holes surrounding such a binary supermassive black hole will be ejected with velocities of the order of the orbital velocities of the components ($\sim$100 000 km/s) [92]. In other words, this mechanism for the formation of rapid pulsars can explain much higher spatial velocities than are observed. Certainly, the number of such neutron stars should be very small. Note that the densities of supermassive black holes ($M_{BH} > 10^8\,M_\odot$) are so low that these objects can also accelerate solar-type dwarfs, and even planets, to relativistic velocities without disrupting them. The detection of such stars is very difficult due to their extremely small number.

As indicated above, young neutron stars, formed from single stars or from components of broad binaries, must slowly rotate with an axial period of some hours. One cannot exclude that periodic radio bursts from the transient GCRT J1745-3009 radio source, discovered in 2002 and having period of 1.27 h [93], belong to a young, slowly rotating neutron star of such a type. And, probably, in accordance with the above scenario of classical radio pulsar formation, such objects represent a basic part of a family of young neutron stars.

ACKNOWLEDGMENTS

The author thanks Prof. S. Woosley and Prof. G.S. Bisnovatyĭ-Kogan for useful discussions on the rotation of presupernova cores. This work was supported by the program of Support for Leading Scientific Schools of the Russian Federation (project no. NSh-162.2003.2), the Russian Foundation for Basic Research (project no. 03-02-16254), and the State Science and Technology Project "Astronomy" (project no. 1102).

REFERENCES

1. W. Baade and F. Zwicky, Proc. Natl. Acad. Sci. USA **20**, 254 (1934).
2. A. Hewish, S. Bell, J. Pickington, *et al.*, Nature **217**, 709 (1967).
3. V. Ginzburg, Dokl. Akad. Nauk SSSR **156**, 43 (1964) [Sov. Phys. Dokl. **9**, 329 (1964)].
4. I. S. Shklovskii, *Supernovae* (Nauka, Moscow, 1976; Wiley, London, 1968).
5. H. Spruit and E. Phinney, Nature **393**, 139 (1998).
6. D. Lai, D. Cheroff, and J. Cordes, Astrophys. J. **549**, 1111 (2001).
7. R. Shirato and G. Fuller, astro-ph/0205390 (2002).
8. H. Janka, astro-ph/0402200 (2004).
9. C. Thompson, Astrophys. J. **534**, 915 (2000).
10. G. S. Bisnovatyi-Kogan and B. A. Komberg, Astron. Zh. **51**, 373 (1974) [Sov. Astron. **18**, 217 (1974)].
11. G. S. Bisnovatyi-Kogan and B. A. Komberg, Pis'ma Astron. Zh. **2**, 338 (1976) [Sov. Astron. Lett. **2**, 130 (1976)].
12. A. V. Tutukov and A. V. Fedorova, Astron. Zh. **80**, 652 (2003) [Astron. Rep. **47**, 600 (2003)].
13. R. Manchester, A. Lyne, J. Taylor, *et al.*, Mon. Not. R. Astron. Soc. **185**, 409 (1978).
14. R. Manchester, A. Lyne, N. D'Amico, *et al.*, Mon. Not. R. Astron. Soc. **279**, 1235 (1996).
15. J. Gunn and J. Ostriker, Astrophys. J. **160**, 979 (1970).
16. A. Lyne and D. Lorimer, Nature **369**, 127 (1994).
17. P. Harrison, A. Lyne, and B. Anderson, Mon. Not. R. Astron. Soc. **261**, 113 (1993).
18. O. Guseinov, E. Yazdan, S. Ozkan, *et al.*, astro-ph/0205540 (2002).
19. A. V. Tutukov, N. N. Chugai, and L. R. Yungel'son, Pis'ma Astron. Zh. **10**, 586 (1984) [Sov. Astron. Lett. **10**, 244 (1984)].
20. Z. Arzoumanian, D. Chernov, and J. Cordes, Astrophys. J. **568**, 289 (2002).
21. E. Pfahl, S. Rappaport, H. Spruit, *et al.*, Astrophys. J. **574**, 364 (2002).
22. A. Heger, S. Woosley, and H. Spruit, astro-ph/0409422 (2004).
23. A. V. Tutukov, Nauchnyi Inform. Astron. Sovet Akad. Nauk SSSR **11**, 62 (1969).
24. A. V. Tutukov and A. V. Fedorova, Astron. Zh. **80**, 652 (2003) [Astron. Rep. **47**, 600 (2003)].

25. G. Meynet and A. Maeder, astro-ph/0409722 (2004).
26. H. Abt, Astrophys. J. **582**, 420 (2003).
27. R. Arlt, R. Hollenbach, and G. Ruediger, Astron. Astrophys. **401**, 1087 (2003).
28. D. O'Toole, S. Jordan, S. Friedrich, *et al.*, astro-ph/0410042 (2004).
29. I. Iben and A. Tutukov, Astrophys. J., Suppl. Ser. **58**, 661 (1985).
30. U. Heber, R. Napiwotzki, and I. Reid, Astron. Astrophys. **323**, 819 (1997).
31. D. Koester, S. Dreizler, V. Weidemann, *et al.*, Astron. Astrophys. **338**, 612 (1998).
32. S. Kawalier, astro-ph/0301539 (2003).
33. C. Brinkworth, M. Burleigh, G. Wynn, *et al.*, Mon. Not. R. Astron. Soc. **348**, L33 (2004).
34. S. N. Fabrika, G. Valyavin, and T. Burlakova, Pis'ma Astron. Zh. **29**, 830 (2003) [Astron. Lett. **29**, 737 (2003)].
35. M. Colpi and I. Wasserman, Astrophys. J. **581**, 1271 (2002).
36. G. S. Bisnovatyi-Kogan, Astrofiz. **31**, 567 (1989).
37. I. Iben and A. Tutukov, Astrophys. J. **456**, 738 (1996).
38. I. Iben and A. Tutukov, Astrophys. J. **501**, 263 (1998).
39. A. V. Tutukov and L. Yungel'son, Nauchnyi Inform. Astron. Sovet Akad. Nauk SSSR **27**, 3 (1973).
40. J. Ziolkowski, Mem. Soc. Astron. Ital. **73**, 1038 (2002).
41. P. Schmidtke, A. Cowley, L. Levenson, *et al.*, Astron. J. **127**, 3388 (2004).
42. W. Vlemings, J. Corder, and S. Chatterjee, Astrophys. J. **610**, 402 (2004).
43. A. Lyne, M. Burgay, M. Kramer, *et al.*, astro-ph/0401086 (2004).
44. A. V. Tutukov and L. Yungel'son, Astron. Zh. **79**, 738 (2002) [Astron. Rep. **46**, 667 (2002)].
45. F. Camilo, B. Lorimer, P. Freire, *et al.*, Astrophys. J. **535**, 975 (2000).
46. D. McConnel, A. Deshpande, and T. Conmer, astro-ph/0312107 (2003).
47. S. Johnstone, A. Lyne, R. Manchester, *et al.*, Mon. Not. R. Astron. Soc. **255**, 401 (1992).
48. M. Kerkwijk and S. Kulkarni, astro-ph/9901149 (1999).
49. D. Champion, D. Lorimer, and M. McLaughlin, Mon. Not. R. Astron. Soc. **350**, L61 (2004).
50. P. Freire, Astrophys. J. **606**, L53 (2004).
51. V. Kaspi, A. Lyne, R. Manchester, *et al.*, Astrophys. J. **543**, 321 (2000).
52. I. Stair, R. Manchester, A. Lyne, *et al.*, Mon. Not. R. Astron. Soc. **325**, 979 (2000).
53. P. Kaaret, G. Cusumano, and B. Socco, Astrophys. J. **542**, L41 (2000).
54. R. Mignani, Astron. Astrophys. **358**, 53 (2000).
55. D. Nice, R. Sayer, and J. Taylor, Astrophys. J. **466**, 87 (1996).
56. N. D'Amico, M. Bailes, A. Lyne, *et al.*, Mon. Not. R. Astron. Soc. **260**, L7 (1993).
57. M. McLaughlin, A. Lyne, D. Lorimer, *et al.*, astro-ph/0408297 (2004).
58. I. Iben, A. Tutukov, and L. Yungelson, Astrophys. J., Suppl. Ser. **100**, 233 (1995).
59. A. Tutukov and A. Cherepashchuk, Astron. Zh. **80**, 419 (2003) [Astron. Rep. **47**, 386 (2003)].
60. L. Bildstein, D. Chakrabarty, J. Chiu, *et al.*, Astrophys. J., Suppl. Ser. **113**, 367 (1997).
61. H. Janka, L. Scheck, K. Kifonidis, *et al.*, astro-ph/0408439 (2004).
62. A. Masevich and A. Tutukov, *Stellar Evolution: Theory and Observations* (Nauka, Moscow, 1988) [in Russian].
63. K. Davidson and J. Ostriker, Astrophys. J. **160**, 979 (1970).
64. A. Doniciano, astro-ph/0306277 (2003).
65. C. W. Allen, *Astrophysical Quantities* (Athlone, London, 1973; Mir, Moscow, 1973).
66. A. Tutukov and A. Cherepashchuk, Astron. Zh. **81**, 43 (2004) [Astron. Rep. **48**, 39 (2004)].
67. V. Kaspi and D. Helfand, Astron. Soc. Pac. Conf. Ser. **271**, 3 (2002).
68. F. Camilo, Astron. Soc. Pac. Conf. Ser. **302**, 145 (2003).
69. A. Ankay, O. Guseinov, and S. Tagieva, astro-ph/0305490 (2003).
70. G. Fan, K. Cheng, and R. Manchester, Astrophys. J. **557**, 297 (2001).
71. E. Cappellaro, R. Evans, and M. Turatto, Astron. Astrophys. **351**, 297 (2001).
72. E. Cappellaro, M. Turatto, and D. Tsvetkov, Astron. Astrophys. **322**, 431 (1997).
73. E. Cappellaro, R. Barbon, and M. Turatto, astro-ph/0310859 (2003).
74. C. Crimani, Astron. Astrophys. **418**, 649 (2004).
75. A. Bressan, M. Della-Valle, and P. Mazziani, Mon. Not. R. Astron. Soc. **331**, L25 (2002).
76. T. Williams, J. McGraw, P. Mason, *et al.*, Publ. Astron. Soc. Pac. **113**, 944 (2001).
77. L. Morales-Rueda, P. Maxted, and T. Marsh, astro-ph/0209472 (2002).
78. L. Morales-Rueda, P. Maxted, T. Marsh, *et al.*, Mon. Not. R. Astron. Soc. **338**, 752 (2003).
79. W. Glatzel and H. Kaltschmidt, Mon. Not. R. Astron. Soc. **337**, 743 (2003).
80. S. O'Toole, T. Bedding, H. Kjeldsen, *et al.*, Mon. Not. R. Astron. Soc. **340**, 865 (2003).
81. H. Edelman, U. Heber, H. Hagen, *et al.*, Astron. Astrophys. **400**, 939 (2003).
82. D. Branch, in *IAU Symposium No. 212: A Massive Star Odyssey: From Main Sequence to Supernova,* Ed. by K. van der Hucht, A. Herrero, and E. Cesar (Astron. Soc. Pac., San Francisco, 2003) **212**, 346 (2003).
83. A. Bogomazov, M. Abubekirov, and V. Lipunov, Astron. Zh. (in press) [Astron. Rep. (in press)].
84. M. Abubekirov, E. Antokhina, and A. Cherepashchuk, Astron. Zh. **81**, 108 (2004) [Astron. Rep. **48**, 89 (2004)].
85. Ph. Podsiadlowski, N. Langer, A. Pelerends, *et al.*, Astrophys. J. **612**, 1044 (2004).

86. A. Faulkner, I. Stair, M. Kramer, *et al.*, astro-ph/0301349 (2003).
87. N. Brandt and Ph. Podsiadlowski, Mon. Not. R. Astron. Soc. **274**, 461 (1995).
88. Ch. Freger, A. Burrows, and W. Benz, Astrophys. J. **496**, 333 (1998).
89. A. Despande, R. Ramachandran, and V. Radhakrishnan, Astron. Astrophys. **351**, 195 (1999).
90. G. S. Bisnovatyi-Kogan, Astron. Astrophys. Trans. **3**, 287 (1993).
91. A. Blaaw, Bull. Astron. Inst. Netherlands **14**, 265 (1961).
92. A. Tutukov, Astron. Zh. **82**, 17 (2005) [Astron. Rep. **49**, 13 (2005)].
93. S. Hyman, T. Lazio, N. Kassim, *et al.,* astro-ph/0503052.

Translated by K. Maslennikov

Astronomy Reports, Vol. 49, No. 7, 2005, pp. 559–566. Translated from Astronomicheskiĭ Zhurnal, Vol. 82, No. 7, 2005, pp. 628–636.

Stokes-Meter Observations of the Solar Mean Magnetic Field: Probable Manifestations of Strong Small-Scale Magnetic Fields

M. L. Demidov, V. M. Grigor'ev, and V. S. Peshcherov

Institute of Solar–Terrestrial Physics, Siberian Division, Russian Academy of Sciences, ul. Lermontova 126, P.O. Box 4026, Irkutsk, 664033 Russia

Received January 25, 2005; in final form, February 17, 2005

Abstract—For many years, information on the solar mean magnetic field (SMMF) of the Sun—an important heliophysical and astrophysical parameter—was restricted to magnetographic measurements in only one spectral line, FeI λ525.02 nm. More informative observations of the Stokes-meter parameters of the SMMF were first initiated on a regular basis at the Sayan Solar Observatory. The availability of I and V data obtained simultaneously in several spectral lines has made it possible to study fundamentally new physical problems. In this paper, based on a comparison of SMMF observations in several spectral lines, we find high correlations in the data and important systematic differences in the magnetic-field strength B, which we interpret as a manifestation of kilogauss magnetic fields in fine-structure magnetic elements. Results of theoretical modeling of the SMMF strength ratios for the FeI λ525.02 nm–FeI λ524.70 nm and FeI λ630.15 nm–FeI λ630.25 nm lines are presented. The asymmetries of the V profiles of four lines near the FeI λ525.02 nm line are examined; these lines are important diagnostics for studies of small-scale dynamical processes. The Sayan Solar Observatory SMMF measurements are in good consistency with the Wilcox Solar Observatory data for 2003: for a comparison of $N = 137$ pairs of points in the two data sets, the correlation coefficient ρ is 0.92 for the linear regression between the datasets $B_{\mathrm{WSO}} = 0.03(\pm0.05) + 0.93(\pm0.03)B_{\mathrm{SSO}}$. © *2005 Pleiades Publishing, Inc.*

1. INTRODUCTION

Until recently, measurements of Stokes-meter parameters were limited to irregular observations with fairly high spatial (angular) resolution and to regions of the solar surface with fairly strong magnetic fields. Regular observations covering the entire solar disk, albeit with moderate (Kitt Peak and Mt. Wilson observatories) or even low (Wilcox Solar Observatory, WSO) spatial resolution, remain of considerable interest. Observations of the solar mean magnetic field (SMMF) of the Sun, which are currently being carried out at Crimean Astrophysical Observatory (CrAO), Sayan Solar Observatory (SSO), and the WSO, likewise remain important. One drawback of the CrAO and WSO observations (compared to opportunities provided by fully modernized systems) is that they are performed in a magnetographic mode, which limits the information carried by the data. Regular measurements of the Stokes-meter I and V profiles have been carried out at the SSO since 1998 using the Solar Telescope for Operative Predictions (STOP) [1, 2]. Observations are obtained simultaneously in several lines (in a spectral bandwidth of $\approx$1 nm) in two modes: (1) observations of the distribution of the large-scale magnetic fields over the solar disk with a resolution of 100″, and (2) observations of the SMMF of the Sun.

The first SMMF observations were carried out in 1968 at the CrAO [3], and were continued on a regular basis over several years [4–6]. Fairly regular SMMF measurements were carried out from 1970 to 1982 at the Mt. Wilson Observatory [7–9], and the most regular data series from 1975 [10] until the present is likewise provided by the WSO. Fairly regular SMMF observations are being obtained at the SSO [11, 12]. After a long interruption, such measurements have now been resumed at the CrAO as well [13, 14].

Interest in the SMMF is associated with the importance of analyzing the integrated parameters of the Sun. For instance, these parameters can be used to judge the Sun as a magneto-variable star, which has important consequences for astrophysics. One example is the attempt of Hejna and Wohl [15] to use SMMF observations to analyze the solar differential rotation (potentially also of interest for stars). The relatively short time required for a single SMMF record (usually several tens of minutes) makes it possible to obtain a long-term, fairly regular data series (especially combining observations from different observatories). This data series, which currently extends over more than 35 years, provides unique opportunities to study both long-term (due to cyclic activity [5]) and shorter period (associated with the

1063-7729/05/4907-0559$26.00

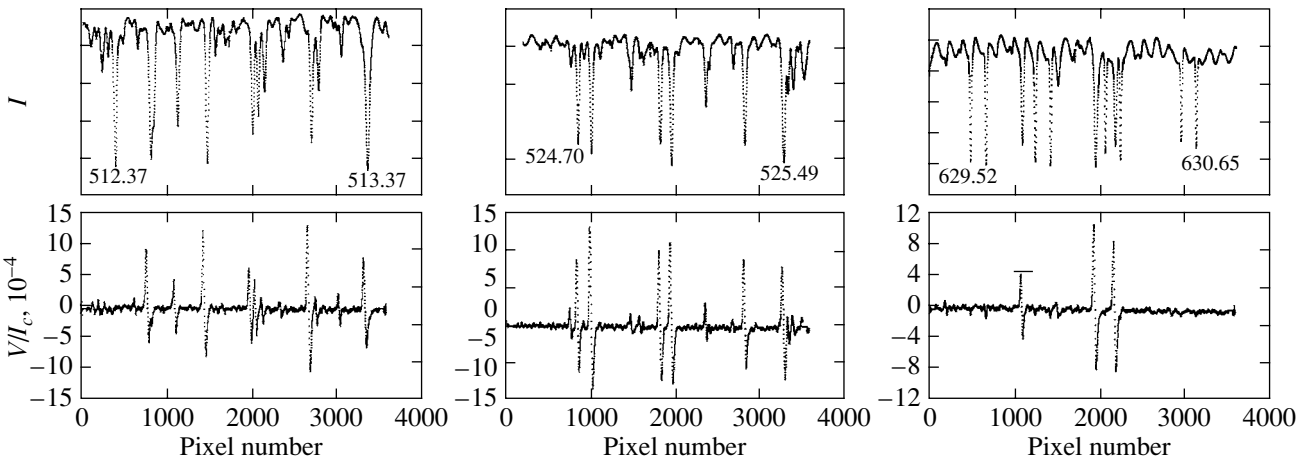

Fig. 1. Example of quasi-simultaneous SMMF measurements at different wavelengths. The upper plots show Stokes-meter I and the lower plots Stokes-meter V. Shown are observations near the nonmagnetic FeI λ512.37 nm line (left), near the FeI λ525.02 nm line (middle), and near the red FeI λ630.15 nm and FeI λ630.25 nm lines (right).

solar rotation [5, 6, 9, 13, 16–21]) time variations of the SMMF. The high correlation of the SMMF with the sectoral pattern of the interplanetary magnetic field [5, 10, 22, 23] makes SMMF observations important from the viewpoint of the intensely developing Space Weather Program as well. The studies [24, 25], in which a correlation between short-timescale variations of the SMMF and coronal mass ejections was found [26], are promising. Recent searches for manifestations of global solar oscillations in fast SMMF variations [27, 28] are likewise of considerable interest. The importance of SMMF observations in connection with deriving the mean parameters of fine-structure magnetic elements statistically averaged over the solar disk will be demonstrated by the results presented here.

2. INSTRUMENTATION AND OBSERVING TECHNIQUE

The photodetector for the STOP Stokes-meter measuring device was a Toshiba TCD-1301D CCD array. The length of the CCD is 29 mm, and it has 3614 working pixels (some pixels are used for service purposes), with each pixel being 200.0×8.0 μm in size (height×width). The signal was digitized by a 12-digit converter. The polarization analyzer consists of a DKDR electro-optical chip and polarization prism. A square-wave control voltage whose amplitude depends on the temperature [29] (in practice over a ± 25°C interval) is fed to the crystal. To optimize the use of the CCD dynamic range, the rate at which the polarization analyzer was operated was more than an order of magnitude higher than the rates of previous magnetographic measurements, and the polarization analyzer dwell-time in each state is 70–80 ms. The rms noise in the continuum for a total integration time of 15 min is $V/I_c = 2 \times 10^{-5}$, which corresponds to a magnetic field of $B \approx 0.05$ G (for the FeI λ525.02 nm line). With longer integration times (which are frequently obtained if the weather allows), an even higher accuracy can be achieved.

The observations are usually carried out near the FeI λ525.02 nm line, but occasionally in other spectral ranges. Figure 1 shows an example of quasi-simultaneous SMMF measurements in three spectral ranges, obtained on January 20, 2002 with the minimum time difference between the observations (corresponding to the time needed to retune the spectrograph). Note the complete absence of circular polarization in the nonmagnetic FeI λ512.37 nm line (lower left graph) and the telluric lines near the red FeI λ630.15 nm and FeI λ630.25 nm lines (lower right graph). The difference in the amplitudes of the Stokes-meter V profiles in different spectral lines is appreciable; we will show below that, in addition to the obvious explanation in terms of differences in the magnetic sensitivities of the lines (the Landé factors, g), this has a deeper physical meaning.

Figure 2 presents an example of the V profiles of the FeI λ525.02 nm line for four consecutive days of SMMF observations. The V profiles have different amplitudes, signs, and shapes on different days, due to the solar rotation and/or the evolution of the magnetic fields on its surface. The second graph, where the V profile does not resemble a "classical" V profile at all, and is more similar to a Q profile, is striking. This is most likely associated with the rotation of magnetic fields of opposite polarities.

When finding the effective SMMF strength shown in Fig. 2 for each day, we simulated the operation

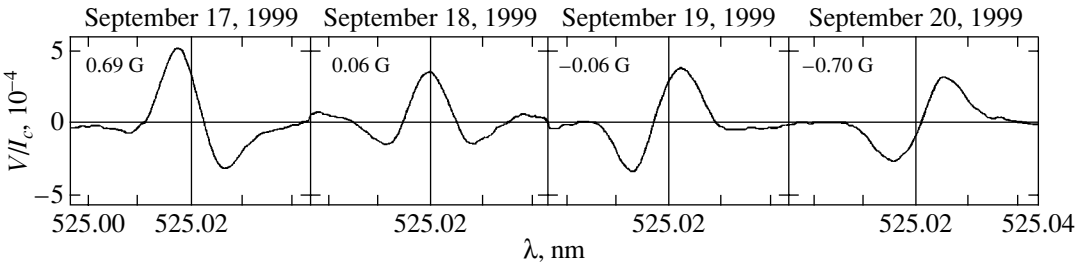

Fig. 2. Example of the Stokes-meter V profiles for the FeI λ525.02 nm line for four consecutive days of SMMF observations. The vertical lines show the positions of the line center. The plots in the upper left-hand corner of each graph are the corresponding magnetic-field strengths.

of a magnetograph whose exit-slit parameters corresponded to previous STOP magnetographic measurements. The resulting magnetic-field strength ensures continuity in the STOP observations, which we will make use of below.

The data on the Stokes-meter parameters enable us to address in a new way the problem of which solar-disk zones make the greatest contribution to the SMMF signal. By definition (and, of course, determined by the observational technique), the SMMF corresponds to contributions from the entire visible solar disk. However, the contributions from different zones (the weighting functions) are not the same for various reasons (limb darkening, rotation, instrumental effects, etc.). Strictly speaking, only at CrAO is the Sun indeed observed as a star, using a parallel beam. All other observatories use additional optics (to increase the luminous flux), which has some effect on the measurements.

Some problems associated with the effect of the optics on the SMMF measurements in connection with the STOP telescope are discussed in [11, 12, 30]. A dedicated study of the zones responsible for the SMMF signal based on Mt. Wilson observations is presented in [7, 31].

On the STOP, we obtain observations of the Stokes-meter parameters for both the SMMF and large-scale magnetic fields with a small time difference; therefore, the contributions from different zones can be determined by comparing the integrated V profile (SMMF observations) with the V profiles obtained by averaging the large-scale magnetic-field Stokes-meter maps over different concentric zones. We carried out a detailed quantitative comparison of the "integrated" and "zonal" V profiles for several tens of days using various criteria. It turned out that the radii of the effective zone vary from $r_z = 0.3\,R_o$ to $r_z = 0.7\,R_o$ on different days; using different criteria sometimes also yields somewhat different values of r_z. In most cases, the main contribution to the SMMF signal is made by solar-disk zones with a radius of about $0.5\,R_o$. In addition, as in [7], we carried out a correlation analysis of the SMMF strengths and strengths calculated from the large-scale magnetic-field observations for solar-disk zones with different diameters for 30 days of observations. Figure 3 shows the results. We can see that, in such a statistical sense, as well, the SMMF strength correlates best with the magnetic fields of the central zone of the solar disk with radius $r_z \leq 0.8\,R_o$, and the effect of the outermost limb zones can be neglected.

3. RESULTS OF THE OBSERVATIONS

We obtain most of our SMMF observations in spectral lines near the traditionally used FeI λ525.02 nm line. However, additional measurements are sometimes carried out in other spectral ranges. Table 1 lists basic information about the parameters of four spectral lines near the FeI λ525.02 nm line and two red iron lines. Of course, as far as diagnostics of the magnetic-field strength are concerned, the simplest interpretation will be provided by measurements in lines of a single multiplet with similar atomic parameters but different Landé factors g. In our case, these are the FeI λ524.70 ($g = 2.0$) and FeI λ525.02 ($g = 3$)

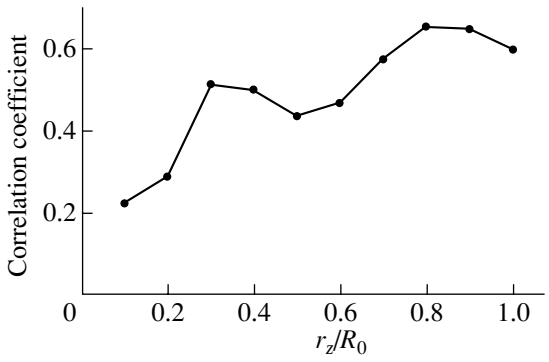

Fig. 3. Correlation between the measured SMMF strengths and the strengths calculated from the observations of large-scale magnetic fields for solar-disk zones with various diameters. The data for 30 days of observations were used.

Table 1. Spectral lines used

λ, nm	Element	Excitation potential, eV		J		Multiplet number	Transition	g_{eff}	Equivalent width, pm
		lower	upper						
524.705	FeI	0.09	2.44	2	3	1	$a^5D-z^7D^0$	2.0	5.9
524.756	CrI	0.96	3.31	0	1	18	$a^5D-a^5P^0$	2.5	7.6
525.021	FeI	0.12	2.47	0	1	1	$a^5D-z^7D^0$	3.0	6.2
525.065	FeI	2.19	4.64	2	3	66	$a^5P-y^5P^0$	1.5	9.9
630.150	FeI	3.64	6.60	2	2	816	$z^5P^2-e^5D^2$	1.667	12.8
630.249	FeI	3.69	5.63	1	0	816	$z^5P^1-e^5D^0$	2.5	8.3

lines—the magnetic-ratio lines proposed and used effectively in [32]. However, for more detailed diagnostics of the magnetohydrodynamic conditions giving rise to the polarized emission, comparisons of observations using other combinations of spectral lines are also useful.

We calculated the regression relationships and correlation coefficients for all combinations of the four spectral lines near the FeI λ525.02 nm line in Table 1, as well as for the red lines. By way of illustration, Fig. 4 shows the regression relationships for the FeI λ525.02 nm–FeI λ524.70 nm and FeI λ630.15 nm–FeI λ630.25 nm line combinations. Table 2 lists the quantitative results of our statistical analysis for all combinations of the four lines near the FeI λ525.02 nm line.

One important result of our analysis is the very high correlation of the data, which testifies to the high accuracy of the measurements. One important factor in this regard is certainly the simultaneity of the measurements in the different lines (in contrast to magnetograph observations). The presence of systematic differences in different lines is quite natural, and contains useful information that requires a physical explanation.

Table 2. Results of the correlation and regression analysis of 370 days of SMMF Stokes-meter observations in various lines. $A(\pm\Delta A)$, $K(\pm\Delta K)$ are the parameters of the linear regression equations $B_{\text{line}Y} = A(\pm\Delta A) + K(\pm\Delta K) \times B_{\text{line}X}$ found using the reduced major-axis method, and ρ is the correlation coefficient

$\lambda(X)$	$\lambda(Y)$	K	ΔK	A	ΔA	ρ
524.705	524.756	0.82	0.03	0.04	0.02	0.77
	525.021	0.92	0.01	0.01	0.00	0.98
	525.066	1.86	0.02	−0.01	0.01	0.97
524.756	525.021	0.67	0.02	−0.01	0.02	0.78
	525.066	1.37	0.04	−0.06	0.04	0.77
525.021	525.066	2.02	0.02	−0.03	0.01	0.98

V profiles with "classical" forms that match theoretical calculations based on uniform models are only rarely displayed in observations of either the SMMF or the large-scale magnetic fields. The most common and conspicuous feature of the V profiles is their asymmetry. As a rule, the blue component is stronger than the red component in terms of both its amplitude and area. There are also (sometimes substantial) shifts of the V relative to the I profiles (predominantly redward). Frequently, the V profiles display a strong, anomalous asymmetry or several intersections of the zero level. Different shapes are sometimes observed for different lines. In these cases, it is not appropriate to think in terms of some definite magnetic-field strength. As in the case of analogous observations of local magnetic fields, we must invoke more complicated, and occasionally fairly exotic, models [33–35]. Naturally, such anomalous profiles must be separated out if we wish to reliably estimate the parameters of the asymmetry. We eliminated profiles from further analysis if, after approximation with a fifth-order polynomial, they did not satisfy two criteria: (a) there was only one intersection of the zero level, and (b) the amplitudes of none of the components were less than $V/I_c = 2 \times 10^{-5}$. Note that applying these criteria to different lines observed on the same day frequently yielded different results.

We described the asymmetry quantitatively (see, e.g., [36]) using the amplitude asymmetry $\delta a = (a_b - a_r)/(a_b + a_r)$ and the area asymmetry $\delta A = (A_b - A_r)/(A_b + A_r)$, where a_b and A_b are the amplitude and area of the blue (short-wavelength) component of the V profile and a_r and A_r are the corresponding quantities for the red component. The relative shift of the V profiles is the wavelength difference (usually expressed in terms of the Doppler velocity) between

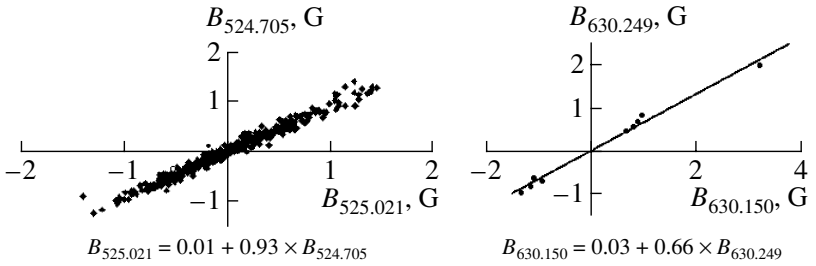

Fig. 4. Comparison of SMMF measurements for the FeI λ524.70 nm and FeI λ525.02 nm lines (left) and FeI λ630.15 nm and FeI λ630.25 nm lines (right).

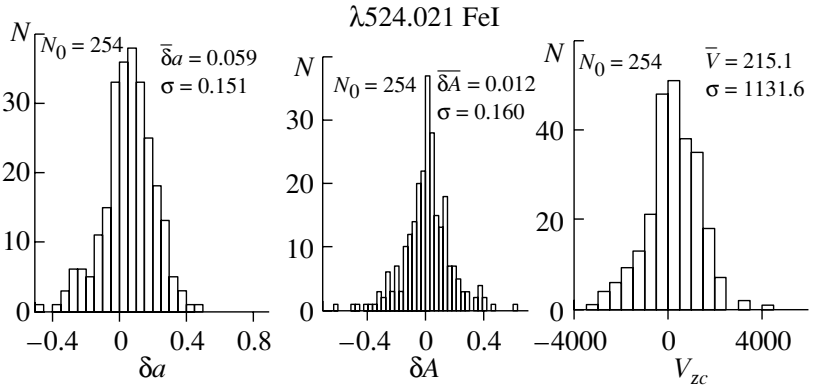

Fig. 5. Histograms of the amplitude asymmetry δa, area asymmetry δA, and relative shifts V_{zc} of the I and V profiles derived from observations of the magnetic field of the Sun as a star in the FeI λ525.02 nm line. The average value and standard deviation are given for each parameter.

the center of the I profile and the point of intersection of the V profile with the zero level. This is accordingly called the "zero-crossing shift," V_{ZC}. In our case, the center of the I profile corresponds to the middle of the interval between the exit slits, which, by analogy with the radial-velocity compensator in a magnetograph, are adjusted to equalize the luminous fluxes in each slit.

Many studies (see the references in [36]) have been dedicated to analyses of the asymmetry parameters and V_{ZC} in different lines and in different observing modes. Theoretical interpretations of the observed values of these parameters usually suppose the existence of considerable gradients of the magnetic field and radial velocity in and near fine-structure magnetic elements.

The results of our analysis of δa, δA, and V_{ZC} for SMMF observations in four lines near the FeI λ525.02 nm line are listed in Table 3. Figure 5 shows histograms of all three asymmetry parameters for the FeI λ525.02 nm line. Our analysis shows that a wide range of values is typical for all lines and all parameters; however, the mean values are different for different lines and differ significantly from zero. One somewhat unexpected result is that the values of δa, δA and V_{ZC} differ appreciably for the "twin lines"—the magnetic-ratio lines, FeI λ524.70 nm line and FeI λ525.02 nm.

4. DISCUSSION

These observational results require an appropriate theoretical interpretation—a question that is not at all trivial and, in many respects, remains unresolved. We plan a dedicated paper devoted to some aspects of this problem. However, some conclusions can already be drawn now.

The question of which scales of magnetic fields are responsible for the SMMF signal remains open: strong fields concentrated in small-scale elements or, on the contrary, weak fields occupying the bulk of the solar surface (the possibility of neglecting the effect of sunspots is shown in [37]). One effective way to address this question (which has long been successfully applied for magnetic-field diagnostics with fairly high spatial resolution [32, 38]) is the method of strength ratios, which compares measurements in lines with different magnetic sensitivities. This method was applied to the SMMF using magnetographic observations in [39]. We have carried out a much more effective analysis using our new, Stokes-meter measurements.

Table 3. Main asymmetry parameters of the V profiles for the SMMF observations. N is the number of observing days, AV are the average values, and RMS are the rms deviations (errors are given in parentheses)

Element λ, nm	N	δa		δA		V_{ZC}, m/s	
		AV	RMS	AV	RMS	AV	RMS
FeI 524.705	233	0.084	0.177	0.014	0.160	−36	1591
		(0.012)	(0.008)	(0.011)	(0.007)	(104)	(74)
CrI 524.756	271	0.097	0.150	0.031	0.147	−113	1625
		(0.009)	(0.006)	(0.009)	(0.006)	(99)	(70)
FeI 525.021	254	0.059	0.151	0.012	0.160	215	1131
		(0.010)	(0.007)	(0.010)	(0.007)	(71)	(50)
FeI 525.065	262	0.128	0.142	0.032	0.172	394	1220
		(0.009)	(0.006)	(0.011)	(0.008)	(75)	(53)

It is clear that the above data on the systematic differences of the SMMF strengths for different spectral lines and the statistically significant asymmetry of the Stokes-meter V profiles cannot be explained in models with a uniform magnetic field with moderate strength. In this case, the V profiles of all spectral lines would be symmetric, their amplitudes would differ precisely in proportion to their Landé factors, and the magnetic-field strengths would be identical. In strong magnetic fields (of the order of 1 kG), the linear dependence between the V amplitude and the field strength breaks down (at different field strengths for different lines, depending on their magnetic sensitivities). We can then estimate the "true" field from the ratio of the measured strengths, of course, taking into account instrumental factors (the width and opening of the slits, etc.). In practice, we must use complex modeling procedures to determine the parameters of the solar atmosphere that can best reproduce the observational data. In general, we must solve the equations of transfer for polarized radiation in a complex, structured medium with various magnetic-field and thermodynamic parameters.

However, applying simplifying assumptions, we can obtain an approximate estimate of the magnetic-field strength that fits the observations, especially by comparing lines within the same multiplet. Figure 6 shows calculated SMMF strength ratios for the FeI λ525.02 nm and FeI λ524.70 nm lines (left) and the FeI λ630.15 nm and FeI λ630.25 nm lines (right) for the facular (dashed curve) and network (solid curve) fine-structure magnetic elements models of [40]. The vertical lines show the observed ratios, and horizontal lines are drawn through the points of intersection of the vertical lines with the theoretical curves. The best agreement between the theoretical and observational values occurs for a strength of 850–1100 G. Of course, this should be treated as only an approximate value.

An interesting result obtained earlier in analyses of δa, δA and V_{ZC} [2, 41, 42] for observations with higher spatial resolution was the sharp increase in the amplitudes of these parameters with decreasing magnetic-field strength at the observed site on the Sun. Despite the considerable noise level, our SMMF data confirm this result. This is illustrated in Fig. 7, which shows δA as a function of B for the FeI λ525.02 nm line. The question naturally arises of whether this distribution is simply due to the increasing errors in δA with decreasing field strength. It is shown in [41] via a comparison of data obtained in two lines with different magnetic sensitivities that this is not the case. In our case, we calculated the distribution as a function of the standard errors in the mean values of δA. These errors (multiplied by 10 to make them visible on the scale of the graph) are shown by the dashed line in Fig. 7. Thus, we are clearly dealing with a real physical, and not a statistical, effect.

It is of interest to see how our new Stokes-meter SMMF measurements agree with the WSO data, which are currently the most uniform and regular data available. Figure 8 shows such a comparison for 2003 (our data correspond to observations in the FeI λ525.02 nm line, and the WSO data have been retrieved from the WSO site). The linear-regression equation,

$$B_{\mathrm{WSO}} = 0.03(\pm 0.05) + 0.93(\pm 0.03) B_{\mathrm{SSO}},$$

has a correlation coefficient of $\rho = 0.92$ (number of pairs of points $N = 137$). This testifies to the very good agreement between the two observational data series.

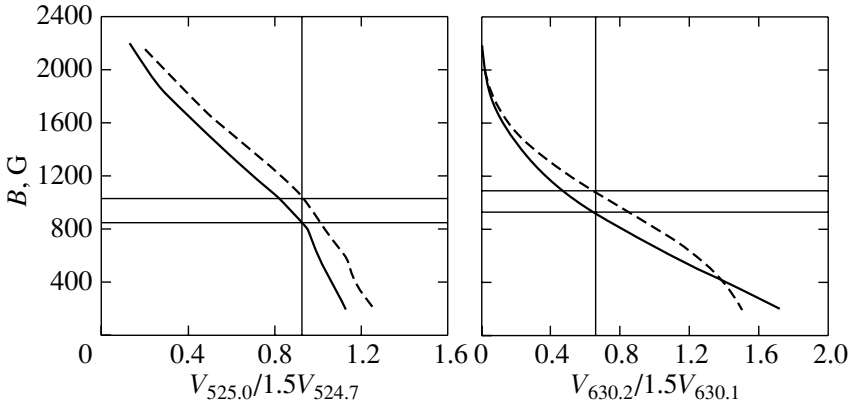

Fig. 6. Comparison of the theoretical and observational SMMF strength ratios in two combinations of spectral lines (the latter shown by vertical lines). The results of calculations for the facular (dashed curves) and network (solid curves) models for the fine-structure magnetic elements of [40] are shown. Horizontal lines are drawn through the points of intersection of the vertical lines with the theoretical curves.

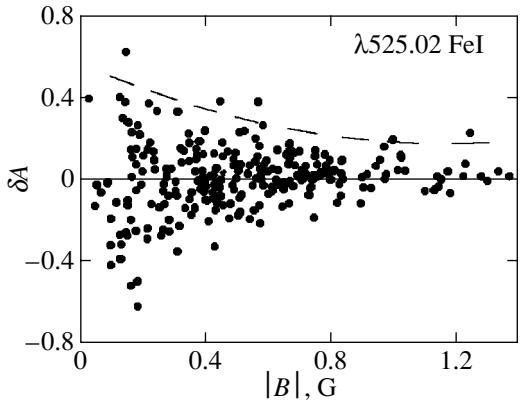

Fig. 7. Comparison of the area asymmetry δA and the SMMF strengths. The dashed curve shows the distribution of the standard errors of the mean δA values, multiplied by 10 to make them visible on the scale of the figure (see text).

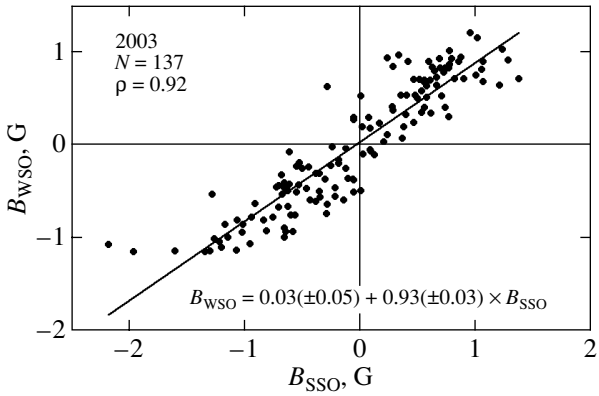

Fig. 8. Comparison of the SMMF measurements carried out in 2003 at the Wilcox Solar Observatory (B_{WSO}) and Sayan Solar Observatory (B_{SSO}; observations in the FeI λ525.02 nm line). N is the number of points, and ρ the correlation coefficient. The regression line, whose equation is given at the bottom of the figure, is shown.

ACKNOWLEDGMENTS

The authors are grateful to the late B.F. Osak for technical support of the STOP telescope, V.V. Zhigalov for software development, T.A. Latushko for data processing, and G.S. Vasil'eva for obtaining the observational data. The calculations for Fig. 6 were carried out by R.M. Veretskiĭ. We also thank V.A. Kotov (CrAO, Ukraine), J.O. Stenflo (Institute of Astronomy, Zürich, Switzerland), and V.N. Obridko (Institute of Terrestrial Magnetism, Ionosphere, and Radiowave Propagation, Russian Academy of Sciences, Moscow) for fruitful discussions of some problems connected with studies of the magnetic field of the Sun as a star. We thank an anonymous referee for comments that helped us to improve the presentation of the results. This work was supported by INTAS (grant no. 00-840), the Russian Foundation for Basic Research (project no. 02-02-16467), the Program of Support of Scientific Schools of the Russian Federation (NSh-733.2003.2), and the Federal Science and Technology Program in Astronomy (1105).

REFERENCES

1. V. S. Peshcherov, V. V. Zhigalov, M. L. Demidov, *et al.*, in *Proceedings of the VII Symposium on Solar–Terrestrial Physics of Russia and the Commonwealth of Independent States* (IZMIRAN, Troitsk, 1999), p. 280 [in Russian].
2. M. L. Demidov, V. S. Peshcherov, V. V. Zhigalov, and V. M. Grigoryev, in *Advanced Solar Polarimetry—Theory, Observation, and Instrumentation*, Ed. by M. Sigwarth (Astron. Soc. Pac., San Francisco, 2001); Astron. Soc. Pac. Conf. Ser. **236**, 471 (2001).

3. A. Severny, Nature **224**, 53 (1969).
4. P. H. Scherrer, J. M. Wilcox, V. A. Kotov, *et al.*, Sol. Phys. **52**, 3 (1977).
5. V. A. Kotov and M. L. Demidov, Izv. Krymsk. Astrofiz. Obs. **61**, 3 (1980).
6. V. A. Kotov and A. B. Severnyi, *General Magnetic Field of the Sun as a Star. Catalog 1968–1976*, Ed. by E. E. Dubov (Mezhvedomstvennyi Geofiz. Komitet Akad. Nauk SSSR, Moscow, 1983) [in Russian].
7. P. H. Scherrer, *A Study of the Mean Solar Magnetic Field*, PhD Thesis (Univ. of California, Berkeley, 1973); Report No. 554, SUIPR (Stanford Univ., Stanford, 1973).
8. V. A. Kotov, M. L. Demidov, V. M. Grigor'ev, *et al.*, Izv. Krymsk. Astrofiz. Obs. **84**, 163 (1992).
9. V. A. Kotov, P. H. Scherrer, R. F. Howard, *et al.*, Astrophys. J., Suppl. Ser. **116**, 103 (1999).
10. P. H. Scherrer, J. M. Wilcox, L. Svalgaard, *et al.*, Sol. Phys. **54**, 353 (1977).
11. V. M. Grigoryev and M. L. Demidov, Sol. Phys. **114**, 147 (1987).
12. M. L. Demidov and V. M. Grigoryev, in *Synoptic Solar Physics*, Ed. by K. S. Balasubramanian, J. Harvey, and D. Rabin (Astron. Soc. Pac., San Francisco, 1998); Astron. Soc. Pac. Conf. Ser. **140**, 271 (1998).
13. V. A. Kotov, V. I. Khaneichuk, and T. T. Tsap, Astron. Zh. **76**, 218 (1999) [Astron. Rep. **43**, 185 (1999)].
14. V. A. Kotov, Astron. Astrophys. **402**, 1145 (2003).
15. L. Hejna and H. Wohl, in *Solar Magnetic Fields*, Ed. by M. Schussler and W. Schmidt (Cambridge University Press, Cambridge, 1994), p. 65.
16. V. A. Kotov and L. S. Levitskii, Izv. Krymsk. Astrofiz. Obs. **66**, 110 (1983).
17. Yu. R. Rivin and V. N. Obridko, Astron. Zh. **69**, 1083 (1992) [Sov. Astron. **36**, 557 (1992)].
18. A. V. Mordvinov and L. A. Plusnina, Sol. Phys. **197**, 1 (2000).
19. V. I. Khaneichuk, Astron. Zh. **76**, 385 (1999) [Astron. Rep. **43**, 330 (1999)].
20. V. I. Khaneichuk, Izv. Krymsk. Astrofiz. Obs. **96**, 176 (2000).
21. V. I. Haneychuk, V. A. Kotov, and T. T. Tsap, Astron. Astrophys. **402**, 1115 (2003).
22. A. B. Severny, J. M. Wilcox, P. H. Scherrer, *et al.*, Sol. Phys. **15**, 3 (1970).
23. J. M. Wilcox, in *IAU Symposium No. 43: Solar Magnetic Fields*, Ed. by R. Howard (Reidel, Dordrecht, 1971), p. 744.
24. F. Boberg and H. Lundstedt, in *SOLSPA: The Second Solar Cycle and Space Weather Euroconference*, Ed. by H. Sawaya-Lacoste (ESA, Noordwijk, 2002), ESA SP-477, p. 79.
25. F. Boberg, H. Lundstedt, J. T. Hoeksema, *et al.*, J. Geophys. Res. A **107**, 10, SSH 15-1 (2002).
26. M. L. Demidov, Sol. Phys. **159**, 23 (1995).
27. R. A. Garcia, P. Bommier, J. Charra, *et al.*, Astron. Astrophys. **346**, 626 (1999).
28. W. J. Chaplin, A. M. Dumbill, Y. Elsworth, *et al.*, Mon. Not. R. Astron. Soc. **343**, 813 (2003).
29. M. L. Demidov, B. F. Osak, and V. N. Gorin, Kin. Fiz. Neb. Tel **11** (4), 78 (1995).
30. M. L. Demidov, Sol. Phys. **164**, 381 (1996).
31. P. H. Scherrer, J. M. Wilcox, and R. Howard, Sol. Phys. **22**, 418 (1972).
32. J. O. Stenflo, Sol. Phys. **32**, 41 (1973).
33. P. H. Bernasconi and S. K. Solanki, Sol. Phys. **164**, 277 (1996).
34. S. R. O. Ploner, M. Schussler, S. K. Solanki, *et al.*, in *Advanced Solar Polarimetry—Theory, Observation, and Instrumentation*, Ed. by M. Sigwarth (Astron. Soc. Pac., San Francisco, 2001); Astron. Soc. Pac. Conf. Ser. **236**, 371 (2001).
35. O. Steiner, in *Advanced Solar Polarimetry—Theory, Observation, and Instrumentation*, Ed. by M. Sigwarth (Astron. Soc. Pac., San Francisco, 2001); Astron. Soc. Pac. Conf. Ser. **236**, 587 (2001).
36. O. Steiner, in *Magnetic Fields and Oscillations*, Ed. by B. Schmieder, A. Hofman, and J. Staude (Astron. Soc. Pac., San Francisco, 1999); Astron. Soc. Pac. Conf. Ser. **184**, 38 (1999).
37. V. A. Kotov, N. N. Stepanyan, and Z. A. Shcherbakova, Izv. Krymsk. Astrofiz. Obs. **56**, 75 (1977).
38. R. Howard and J. O. Stenflo, Sol. Phys. **22**, 402 (1972).
39. M. L. Demidov, in *Synoptic Solar Physics*, Ed. by K. S. Balasubramanian, J. Harvey, and D. Rabin (Astron. Soc. Pac., San Francisco, 1998); Astron. Soc. Pac. Conf. Ser. **140**, 171 (1998).
40. S. K. Solanki, Astron. Astrophys. **168**, 311 (1986).
41. V. Grossmann-Doerth, C. U. Keller, and M. Schussler, Astron. Astrophys. **310**, 610 (1996).
42. M. Sigwarth, K. S. Balasubramaniam, M. Knolker, *et al.*, Astron. Astrophys. **349**, 941 (1999).

Translated by G. Rudnitskiĭ

Astronomy Reports, Vol. 49, No. 7, 2005, pp. 567–578. Translated from Astronomicheskiĭ Zhurnal, Vol. 82, No. 7, 2005, pp. 637–648.

Gamma-Ray Radiation with Energy 2.223 MeV and the Density Distribution in the Solar Atmosphere during Flares

B. M. Kuzhevskij[1], L. I. Miroshnichenko[2], and E. V. Troitskaia[1]

[1] *Skobel'tsyn Nuclear Physics Research Institute, Moscow State University, Moscow, Russia*

[2] *Pushkov Institute for Terrestrial Magnetism, the Ionosphere, and Radiowave Propagation, Troitsk, Russia*

Received December 25, 2004; in final form, February 17, 2005

Abstract—Interactions of particles accelerated in solar flares with matter in the solar atmosphere give rise to neutrons, which are efficiently captured on hydrogen nuclei as they are slowed to thermal velocities. This capture is accompanied by the emission of a gamma-ray with energy 2.223 MeV. Observational data for the temporal profiles of the gamma-ray fluxes in this line are used to study the plasma-density distribution in the solar atmosphere during the flares of December 16, 1988, March 22, 1991, and November 6, 1997. This analysis is based on comparisons between the observations and profiles computed taking into account a number of parameters describing the generation and transport of the flare neutrons in atmospheric layers of various densities. In three cases studied, the density of the material in the photosphere below the flare region is enhanced compared to the density in an unperturbed part of the solar atmosphere at the same height. In the case of the December 16, 1988 flare, we are able for the first time to relate the profile of the 2.223 MeV line with the shape of the accelerated particle (proton) spectrum. This opens new possibilities for studies of particle acceleration on the Sun based on observations of flare gamma-ray emission. © *2005 Pleiades Publishing, Inc.*

1. INTRODUCTION

Gamma-ray radiation in nuclear lines was first detected during a series of prominent proton events in August 1972 [1]. The first detection of flare neutrons was made nearly eight years later, during the flare of June 21, 1980 [2]. Soon, studies of solar gamma-rays and neutrons (neutral solar radiation) became a powerful means to investigate flares and the properties of the solar atmosphere. Data on this neutral radiation can provide information about the properties of accelerated particles and the parameters of the surrounding medium at the locations of nuclear reactions in the atmosphere. The extraction of this information requires preliminary model calculations of the spectra of the neutrons and gamma-rays as a function of various parameters of the flare process.

A prime illustration of the possibilities provided by observations of gamma-rays and neutrons from the Sun is the reconstruction of spectra and estimation of the total number of accelerated particles based on data on nuclear gamma-ray lines [3–6]. The time behavior of the flux of observed neutrons can be used to derive the spectrum of the neutrons generated during a flare. In turn, this makes it possible to reconstruct in an independent way the spectrum and estimate the total number of accelerated particles [3, 6]. Hua and Lingenfelter [7] proposed a method for determining the angular distribution of the accelerated ions based on the observed flux of flare gamma-rays.

Together with this, the possibility of determining the ^{3}He content in the photosphere from observations of gamma-ray lines was demonstrated [8, 9]. Gamma-ray data for flares were applied to the development of techniques for solar nuclear gamma-ray spectroscopy, which can be used to determine the elementary composition of particles in the places where nuclear reactions occur, as well as the composition of the accelerated particles taking part in these reactions [3, 10].

During the onset and development of a flare, and also in the post-flare stage, fluctuations of the plasma density and temperature should unavoidably appear in the solar atmosphere on various spatial and temporal scales [11–14]. Models with a layered flare region with variable density provide one example [12]. A number of theoretical works analyzing the response of the solar atmosphere to the primary energy release of a flare [11–14] indicate that the motion of a cool, dense condensation (or several such condensations) ahead of the shock wave propagating downward from the region of energy release (i.e., toward the photosphere) is possible. This picture is confirmed, for example, by the data for the white flares of June 4, 1980 and June 15, 1991 [15]. In the latter case, a radial velocity for the downward motion of the radiating mate-

rial of 20–23 km/s was obtained for a chromospheric condensation formed during the sudden heating of the upper chromosphere by the flux of heat from the corona. It is likely that the presence of downward-moving radiating material is a common feature of the impulsive phases of powerful flares [15]. On the other hand, we have the concept of a new magnetic field ascending in a previously existing region of "old" field. Such rising magnetic fields are considered to be sources of flares, as has been confirmed to some extent by observations [16].

The neutrons arising during interactions between accelerated particles and various nuclei are decelerated in the solar atmosphere and, when they reach thermal energies, begin to be efficiently captured by hydrogen nuclei ^{1}H, leading to the formation of deuterium ^{2}H (or d):

$$n + {}^1\mathrm{H} \rightarrow d + \gamma.$$

This reaction is a source of gamma-rays with energy $E_\gamma = 2.223$ MeV. However, the flux density of these gamma-rays depends strongly on the number density of ^{3}He nuclei in the solar atmosphere [17, 18]. The cross section for the radiationless capture of a neutron by a ^{3}He nucleus, with the formation of tritium ^{3}H,

$$n + {}^3\mathrm{He} \rightarrow {}^3\mathrm{H} + p$$

is nearly a factor of 1.7×10^4 higher than the cross section for neutron capture by hydrogen. Data on the density of ^{3}He in the Sun imply that the roles of these two reactions should be comparable [4]. Neutrons are not only efficiently captured by ^{3}He nuclei, but also decay over a mean lifetime of $\tau_d \approx 918$ s. In addition, neutrons can be scattered into large angles, with their subsequent escape into interplanetary space. All these factors decrease the number of neutrons that are captured by hydrogen, thereby decreasing the emergent flux of gamma-rays with $E_\gamma = 2.223$ MeV.

The demonstration that the time variations of the 2.223 MeV radiation contain information about the height variations of the plasma density in the solar atmosphere was of fundamental importance [19–21]. The model computations of [19] for the case of an instantaneous point source of neutrons identified the main factors influencing the distribution of depths at which neutrons of various energies are thermalized:

(1) the energy spectrum of the neutrons,

(2) the angular characteristics of the incident beam,

(3) the angular dependence for the elastic scattering of neutrons on hydrogen,

(4) the density profile with height in the solar atmosphere, and

(5) the kinematics of the nuclear reactions involved.

The computations of [21] for neutrons with an initial energy of 30 MeV and several model density distributions confirmed the expected differences in the time profiles for gamma-ray lines.

In this paper, we briefly describe the method we have used and our computational model (Section 2). In Section 3, the results of the model computations are used to analyze the time profiles of the gamma-rays observed for three flares: December 16, 1988 (SMM), March 22, 1991 (GRANAT), and November 6, 1997 (Yohkoh). Section 4 contains a discussion of the results. Our main result is the detection of a density enhancement in the photosphere during these three flares compared to the density expected for the unperturbed solar atmosphere.

2. METHOD AND COMPUTATIONAL MODEL

Studies of gamma-rays with energy 2.223 MeV from solar flares can be used to probe an extensive layer of solar plasma, beginning from the chromosphere and continuing to levels that are not currently accessible to observation using other (spectroscopic) methods. This became clear after the detailed model computations of [19–23]. First and foremost, these works analyzed the propagation of neutrons arising in nuclear reactions during solar flares and subsequently penetrating to deep layers of the Sun. In particular, Kuzhevskij and Kogan-Laskina [20] were the first to attempt to obtain analytical expressions that could be used to study the distribution of plasma in the solar atmosphere based on an analysis of gamma-ray radiation due to neutron absorption. The radiation of the 2.223 MeV gamma-ray line during the capture of neutrons by hydrogen nuclei and its subsequent absorption in the solar plasma were considered. On this basis, a method for deriving the density profile with height in the solar atmosphere during a flare using the observed time variations of the flux of gamma-rays with $E_\gamma = 2.223$ MeV was proposed. Computations were carried out for (monoenergetic) neutrons with energies in the range $E_n = 0.1$–100 MeV, which were the most efficient in producing gamma-rays with $E_\gamma = 2.223$ MeV. The isotropic emission of neutrons into a lower hemisphere from a level lying above the photosphere with a number density of no more than 5×10^{15} cm^{-3} was assumed, since only near this depth can neutrons with minimum initial energies of $E_n = 0,1$ MeV become thermalized (the zero depth corresponds to the level with number density 10^{12} cm^{-3}). Analogous computations were carried out for the case when the initial energy spectrum of the neutrons is a power law with index $s = 0$–3, $\sim E_n^{-s}$, for various density profiles with height in the solar atmosphere. The duration and time profile of the flux of emitted primary neutrons were also accurately

taken into account, as well as their radiationless absorption by ^{3}He nuclei. The dependence of the flux of gamma-rays with $E_\gamma = 2.223$ MeV on the central (heliocentric) angle of the flare was studied separately.

Density models. To allow for possible deviations of the density from the standard model for the unperturbed solar atmosphere (model 1; i.e., $m = 1$, with m also denoting the model number), Kuzhevskij and Troitskaia [19] constructed four additional models corresponding to both enhanced and lowered densities in layers at various depths (Fig. 1). In the basic model 1, the density grows smoothly from 1.5×10^{16} cm^{-3} at the top of the photosphere (where the optical depth to radiation at a wavelength of 5000 Å is $\tau = 0.005$) to 2.5×10^{17} cm^{-3} at a level 330 km lower, where $\tau = 1$; over the following 60 km in depth, the optical depth grows to $\tau = 10$. In model 2, the density increases to 8×10^{17} cm^{-3} at depths of ~500 km below the top of the photosphere, i.e., in deep subphotospheric layers; in model 3, the density grows smoothly below the photosphere, reaching 6×10^{17} cm^{-3} at the same depths. Model 4 represents the case of decreased density, with the reduction beginning above the photosphere, and the density taking the value 3×10^{15} cm^{-3} at the top of the photosphere and 2×10^{16} cm^{-3} 330 km below this level. Model 5 corresponds to the special case of an enhanced density equal to 2.5×10^{17} cm^{-3} over the entire thickness of the photosphere. The height dependences for the density and temperature of the solar atmosphere in the basic model (curve *1* in Fig. 1) correspond to the model for the lower chromosphere and photosphere of [24], which is in agreement with the model for the convective zone of [25].

The medium in [19] was taken to be pure hydrogen, and the computations of [19–23] were carried out for an instantaneous point source of neutrons and the five density models presented in Fig. 1. Other important aspects of the problem were subsequently studied [26–28]. For example, Kuzhevskij and Troitskaia [26] were the first to try to take into account (via simple estimates) the contribution of radiationless absorption of neutrons by ^{3}He nuclei. The computations of [26–28] included the duration and time profile for the injection of neutrons, which were taken into account using the method proposed earlier in [23]. The initial angular distribution of the neutrons was taken to be isotropic. This assumption is in agreement with the angular distribution of neutrons emitted in nuclear processes leading to the generation of neutrons in the energy interval indicated above. In fact, it proved to be sufficient to consider neutrons only in the lower hemisphere.

In the end, we showed that it is important to take into account the following processes if we wish to

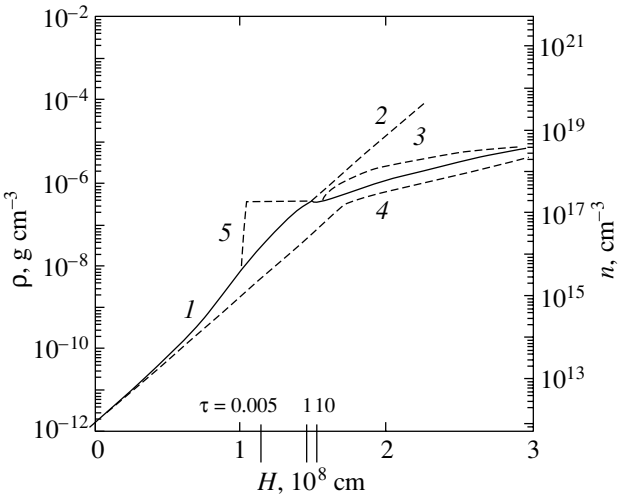

Fig. 1. Models describing the density of the solar atmosphere as a function of depth: (1) standard HSRA–Spruit model [24, 25] (solid), (2)–(5) the deformed models of [19] (their deviations from model 1 are shown by the dashed curves). τ is the optical depth to radiation with wavelength $\lambda = 500$ nm.

make effective use of data for 2.223 MeV gamma-ray radiation:

(1) the deceleration of neutrons in the solar atmosphere due to elastic scattering on hydrogen nuclei, taking into account the energy and angular dependences of the effective cross sections for *np* scattering,

(2) the possible escape of energetic neutrons with energies $E_n \geq 2$ keV from the solar atmosphere,

(3) the gravitational action of the Sun on neutrons with $E_n < 2$ keV,

(4) the thermal motions of decelerated neutrons,

(5) neutron decay,

(6) the capture of neutrons by hydrogen, with the formation of a deuteron and a gamma-ray with energy 2.223 MeV,

(7) the radiationless capture of neutrons by ^{3}He nuclei,

(8) the absorption of emergent gamma-rays as a function of the position of a flare on the Sun relative to the observer (the central angle of the flare),

(9) the time profile for the injection of neutrons under the assumption that it is proportional to the profile for the injection of the total flux of gamma-ray radiation with energies 4–7 MeV corresponding to the excitation of nuclei of ^{12}C and ^{16}O,

(10) the initial spectrum of the neutrons,

(11) the dependence of the density of the surrounding medium on height.

Our understanding of the pattern of emitted 2.223 MeV gamma-rays has recently been refined,

Table 1. Differences δ between the expected fluxes of 2.223 MeV gamma-rays calculated for various central flare angles [26, 27]

Model	t, s	Generation	Flare angle		
			0°	40°	80°
		δ, %			
		$s = 0$			
1–2	145	38	20	20	0
1–5	145	16	1	3	22
2–5	145	48	21	17	22
1–5	375	94	71	70	58
1–4	405	19	19	16	14
		$s = 3$			
1–4	15	15	13	14	15
1–5	15	15	13	14	15
4–5	15	62	63	64	68
1–5	365	69	69	68	57
1–4	405	8	8	9	8

enabling us to broaden the domain of applicability of data for this line. This became possible through studies of the dependence of the flux of gamma-rays on the central angle of the flare, more accurate account of the radiationless capture of neutrons by ^{3}He nuclei, and direct inclusion of the original spectra of the neutrons and accelerated particles in model computations. Since such studies clearly present more than purely methodical interest, we will consider these questions in somewhat more detail.

Dependence of the gamma-ray flux on the position of the flare. The main mechanism attenuating the flux of gamma-rays with energy 2.223 MeV is Compton scattering of the gamma-rays on electrons. The corresponding extinction coefficient per atom in hydrogen is $\mu = 0.139\sigma_{\rm H}$, with the mass extinction coefficient being $\mu/\rho = 0.08329$ cm^2/g. Assuming that the gamma-ray radiation is isotropic, according to the computations of [27], the flux of gamma-rays from a flare at heliolongitude $\theta = \pm 80°$ relative to the central meridian of the Sun will be appreciably lower than the fluxes from equivalent flares located at $\theta = 0°$ and $\theta = \pm 40°$. However, the time profiles of gamma-rays from flares at $\theta = 40°$ and $\theta = 80°$ proved to be similar to the profile computed for a central flare at $\theta = 0°$ [26]. Differences between the computed time profiles for the 2.223 MeV gamma-ray line for flares located at $\theta = 0°$ were discussed earlier in [22] in connection with the possibility of testing density models (Fig. 1) based on data that can be obtained with modern instruments. It was subsequently discovered [27] that, in some cases, there are appreciable differences between model profiles for flares at heliolongitudes of 40° and 80°. Computations were carried out for all five density models (Fig. 1) for an initial neutron energy of 30 MeV and various indices for the neutron spectrum $s = 0$–3. The differences between the computed 2.223 MeV gamma-ray fluxes δ (in %) for various central flare angles are presented in Table 1. From an observational point of view, this question reduces to a comparison of the sensitivities of various gamma-ray detectors. Kuzhevskij *et al.* [23] estimated relative instrumental 1σ errors for a level of 1 cm^{-2}/s for data obtained using three gamma-ray detectors based on crystal scintillators and averaged over 32 s—OSSE (Compton Gamma-Ray Obseratory) [29], GRS (SMM) [30], and SONG (CORONAS) [31]. The data in Table 1 testify that, in many cases, differences in the time profiles of the 2.223 MeV line due to properties of the density models for the solar atmosphere can be observed using these existing detectors. This is at least true for flares with heliocentric angles to ±80°. Note that the sensitivities of the OSSE and Yohkoh detectors are comparable when the gamma-ray energies involved are higher than several MeV [32].

Radiationless neutron capture. The need to include the radiationless capture of neutrons by ^{3}He nuclei was first noted in [33, 34]. For the case of an instantaneous source of neutrons, the constant decrease τ of the time profile in the absence of ^{3}He can be estimated using the formula

$$1/\tau = 1/\tau_{\rm H} + 1/\tau_d, \qquad (1)$$

where τ_d is the mean lifetime of the neutrons to decay and $\tau_{\rm H}$ is their mean lifetime to capture by hydrogen, with the subsequent generation of 2.223 MeV gamma-rays. In the presence of ^{3}He in the solar atmosphere, the resulting decay constant τ_1 is given by the relation [7]

$$1/\tau_1 = 1/\tau_{\rm H} + 1/\tau_d + 1/\tau_{\rm He} \qquad (2)$$

where $\tau_{\rm He}$ is the mean lifetime of the neutrons to capture by ^{3}He nuclei. The ratio of the numbers of neutrons captured by ^{3}He and hydrogen nuclei is given by the formula

$$\eta = n_{\rm He}\sigma_{\rm He}/n_{\rm H}\sigma_{\rm H}, \qquad (3)$$

where $n_{\rm He}/n_{\rm H} = 2.0 \times 10^{-5}$ is the ratio of the number densities of ^{3}He and hydrogen in the solar atmosphere [7] and $\sigma_{\rm He}/\sigma_{\rm H} = 1.61 \times 10^4$ is the ratio of the corresponding cross sections for neutron capture. It follows that $\eta = 0.322$, which was used in [26] to

Table 2. Relative content of ^{3}He in the photosphere based on data for the time profiles of the 2.223 MeV line for five solar flares [38]

Flare	$n_{\rm He}/n_{\rm H}, 10^{-5}$	Spacecraft and reference
June 3, 1982	≤ 3.8	SMM/GRS [35]
June 3, 1982	2.3 ± 1.2	SMM/GRS [7]
June 4, 1991	2.3	CGRO/OSSE [36]
June 11, 1991	2.0–5.0	GRANAT/PHEBUS [37]
November 6, 1997	2.3 ± 1.4	Yohkoh [38]

estimate the expected contribution of ^{3}He to the observed time profile of 2.223 MeV gamma-rays. With $\tau_d = 918$ s and $\tau_d \gg \tau_{\rm H}$, we obtain from (1)–(3) $\tau_1 = (3/4)\tau$.

This correction must be included in the computed time profiles for the 2.223 MeV gamma-rays. It can also be included in the time profiles for the decay constants τ when analyzing the observed profiles of the 2.223 MeV line, as was done in [26] in a comparison of computed and observed profiles for the flare of March 22, 1991 (see below). In view of the importance of radiationless neutron capture, we present a master list of estimates of the ratio $n_{\rm He}/n_{\rm H}$ obtained by various groups [7, 35–38] from data on profiles of the 2.223 MeV line for several flares (Table 2).

Monte Carlo simulations with statistical weights were applied to compute the radiationless capture of neutrons by ^{3}He in [26]. As earlier, the ratios of the cross sections for neutron capture without and with radiation and of the number densities of ^{3}He and H were taken to be $\sigma_{^3{\rm He}}/\sigma_{\rm H} = 1.61 \times 10^4$ and $n_{^3{\rm He}}/n_{\rm H} = 2 \times 10^{-5}$ [7]. The probability of a radiationless capture of a neutron by a ^{3}He nucleus is determined by the expression

$$p_{^3{\rm He}} = \frac{\omega_{^3{\rm He}}}{\omega_n} = \frac{\sigma_{^3{\rm He}} n_{^3{\rm He}}}{\sigma_{\rm H} n_{\rm H} + \sigma_{^3{\rm He}} n_{^3{\rm He}} + \sigma_{\rm el} n_{\rm H}}. \quad (4)$$

Here, ω_n is the statistical weight of the neutron before the collision, $\omega_{^3{\rm He}}$ is the fraction of the statistical weight corresponding to absorption by ^{3}He nuclei, $\sigma_{\rm H} = 7.32 \times 10^4/\nu_{n{\rm H}}$ barn, where $\nu_{n{\rm H}}$ is the relative velocity of the neutron and hydrogen nucleus (cm/s), and $\sigma_{\rm el}$ is the cross section for elastic np scattering. It follows from (3) that

$$\omega_{^3{\rm He}} = \frac{0.322\omega_n}{1.322 + \sigma_{\rm el}\nu_{n{\rm H}}/7.32 \times 10^4}. \quad (5)$$

Analogously, the fraction of the statistical weight corresponding to capture by hydrogen has the form

$$\omega_{\rm H} = \frac{\omega_n}{1.322 + \sigma_{\rm el}\nu_{n{\rm H}}/7.32 \times 10^4}. \quad (6)$$

Formulas (5), (6) were used in the analysis of each elastic collision. The computations assumed the isotropic injection of the initial neutrons into the lower photosphere. An exact treatment of the duration and time profile of the flux of emitted primary neutrons and of their radiationless absorption by ^{3}He was carried out in [26], and the results of those computations applied to the gamma-ray data for the flare of November 6, 1997 in [27]. It would be very important for our understanding of particle acceleration on the Sun to establish a direct connection between the time profile of the 2.223 MeV line and the shape of the spectrum of accelerated particles. This relation was first studied in [39] using data for the flare of December 16, 1988. The main results of the analysis for the three flares indicated above are described in more detail below.

Table 3. Comparison of model and observational results for the 2.223-MeV line decay constant for the flare of March 22, 1991 [26, 27]

^{3}He/H	m	s	Σ_w (with weights)	$N(\Sigma_w)$	Σ (without weights)	$N(\Sigma)$
0	1	0	34.03	5	1208	4
	2	0	0.87	1	401	2
	3	0	4.22	2	188	1
	4	0	27.11	4	1160	3
	5	3	14.55	3	1233	5
2×10^{-5}	1	1	52.3	8	1602	4
	2	1	7.40	2	290	1
	3	1	22.10	6	698	2
	4	1	40.6	7	1254	3
	5	0	12.64	5	810	8
	5	1	9.40	4	591	7
	5	2	7.71	3	4824	6
	5	3	7.11	1	4463	5

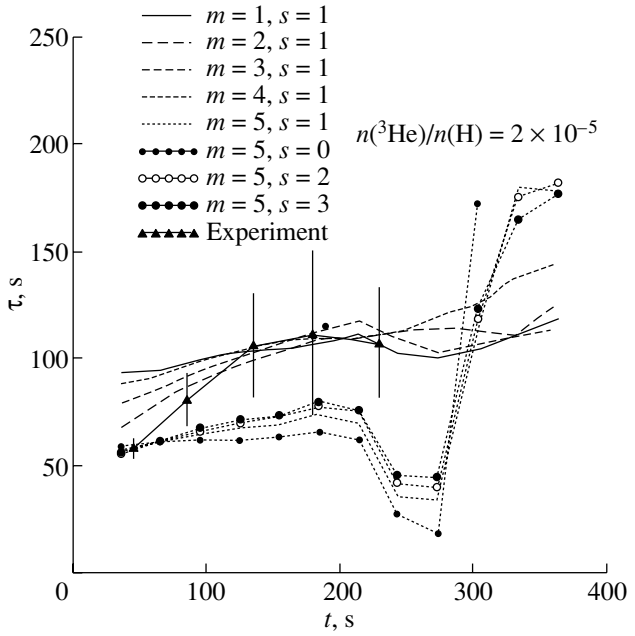

Fig. 2. Comparison of time profiles for the decay constants $\tau(t)$ (i) derived from the computed time profiles for the gamma-ray radiation [26] for a number of combinations of the model density in the solar atmosphere and the index of the initial neutron spectrum, and (ii) calculated using the five measurements of the gamma-ray flux obtained by the PHEBUS detector on the GRANAT observatory during the flare of March 22, 1991 [40].

3. RESULTS

There are relatively few detailed measurements of the 2.223-MeV line for flares, and not all the available data are suitable for analyses using the method described above. The first suitable gamma-ray event of this type was the flare of March 22, 1991 [40]. However, even in this case, we have only a small amount of information about the gamma-ray emission: there are no reliable measurements of the time variations of the 2.223 MeV line or of the lines at 4–7 MeV. Essentially, we have only the decay constants for the fluence of the 2.223 MeV line based on five temporal points. Nevertheless, these data were used for model computations [26], which yielded both time profiles and decay constants, which, in turn, enabled the first comparison of the model with the observations.

Flare of March 22, 1991. A burst of gamma-rays from the class 3B/X9.4 flare on March 22, 1991 (S26, E28) was detected at 22:42:51 UT by the PHEBUS instrument on the GRANAT observatory [40]. The source of neutrons in this impulsive event can be considered to be approximately instantaneous. Time profiles of the fluxes of gamma-rays and of the decay constants were computed for this case, for four spectral indices and all five models (Fig. 1) for the central angle of the flare, 37.5° [26]. The analysis used the results of computations of the decay constant [40] at the five measured points of the time profile of the 2.223 MeV gamma-ray line. The contribution of radiationless absorption of the neutrons by ^{3}He nuclei was taken into account via a simple estimate, and, in general, possible time variations of the neutron injection rate were not included (the injection of the primary neutrons was taken to be instantaneous). Figure 2 shows a comparison of the computed decay constants $\tau(t)$ and the observations. The best agreement with the observations for $^3\mathrm{He/H} = 2 \times 10^{-5}$ is given by $s = 3$ and $m = 5$ (an enhanced density in the photosphere). The least-squares results with and without statistical weights for two values of the ^{3}He/H ratio are presented in Table 3, where $\sum = \sum_{i=1}^{6}(\tau_{oi} - \tau_i)^2$ and $\sum_w = \sum_{i=1}^{6} \frac{1}{\sigma_{oi}^2}(\tau_{oi} - \tau_i)^2$ are the sums of the squared deviations obtained for the five points without and with the statistical weights and $i = 1$–5; and τ_{oi} and τ_i are the observational and model values of τ.

Flare of November 6, 1997. The burst of gamma-ray radiation detected by the Yohkoh satellite at 11:52 UT on November 6, 1997 [38] was associated with a class 2B/X9.4 solar flare (S18, W64). We used the data for the 2.223 MeV gamma-ray line and the instantaneous $^{12}\mathrm{C} + {}^{16}\mathrm{O}$ line "cleaned" by the authors of [38].

The time profile of the neutrons injected during the flare was taken to be similar ("proportional") to the profile of gamma-rays in the $^{12}\mathrm{C} + {}^{16}\mathrm{O}$ line. In the computations, the total time interval for the observations, 0–440 s, was divided into 23 subintervals, each with a separate source. The initial statistical weight of the neutrons was taken to be equal to the ratio of the area under the curve for the given interval and the total area under the curve.

Time profiles were computed for a central flare angle of 65°, spectral indices $s = 0$–3, and for four of the five density models ($m = 1, 2, 4, 5$). One case of reduced density and two cases of enhanced density are presented. Model 3 was not considered for this event, since the computed time profiles for the 2.223 MeV gamma-ray line for models 2 and 3 proved to be very similar for this flare, which was far from the center of the solar disk. Time profiles of the decay constants were calculated for the obtained gamma-ray-flux time profiles. Using a least-squares criterion (with and without statistical weights), the resulting curves were compared with the decay constants calculated in [28] at six points using the data of [38]. Figure 3 shows the time profiles of the fluxes and the decay constants for the case $s = 1$ as an example. Comparisons of the

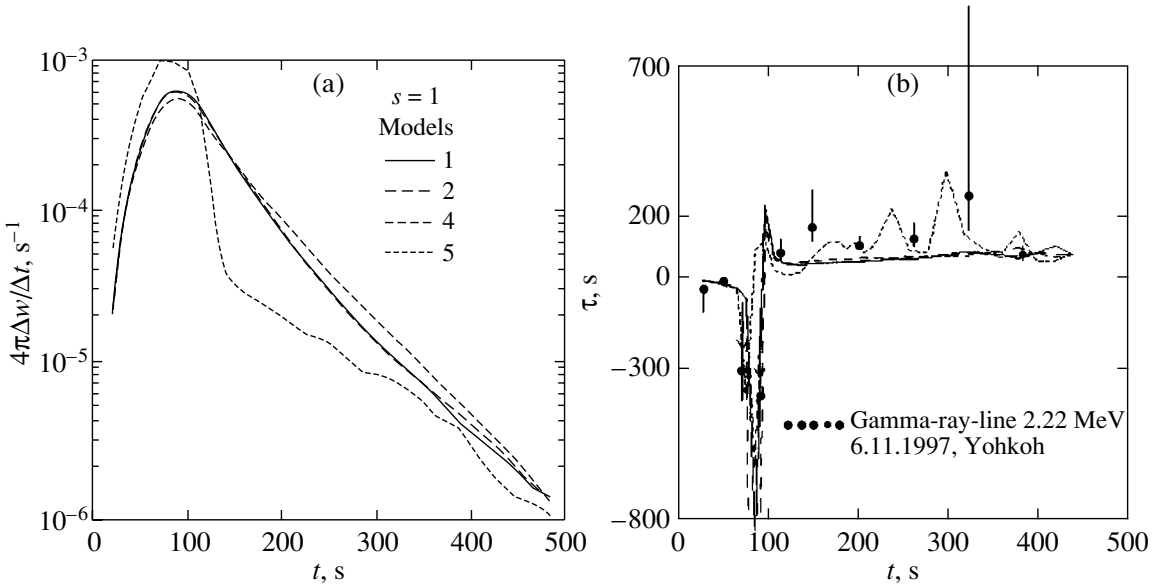

Fig. 3. (a) Time profiles of the flux of 2.223 MeV gamma-rays per neutron. The quantity $\Delta w/\Delta t$ denotes the number of gamma-rays escaping per unit time in a specified direction, $\Delta t = 10$ s, and $s = 1$. (b) Time profiles of the decay constants compared with the decay constants calculated using the observational data for the flare of November 6, 1997 for $s = 1$ [27, 28].

observational data and calculated values for two flares are presented in Tables 4 and 5.

Table 4 contains the sums of the squared deviations obtained for six points without and with allowance for the statistical weights, $\sum = \sum_{i=1}^{6}(\tau_{oi} - \tau_I)^2$ and $\sum = \sum_{i=1}^{6}\frac{1}{\sigma_{oi}^2}(\tau_{oi} - \tau_i)^2$, where τ_{oi} are the observational and τ_i the model values of τ. The asterisks mark cases for which the agreement between the observational and computed decay constants is best.

The results of determining the model densities for the flares of November 6, 1997 and March 22, 1991 for various forms of neutron-injection function (three cases in all) are presented in Table 5.

The method of [19–23] was first applied to the flare of March 22, 1991 in [26], but it was assumed that the neutrons were injected vertically downward, and capture by ^{3}He nuclei was taken into account only via a simplified estimate (see above). In all three cases considered, we were able to derive a model for the height dependence of the solar plasma density and the initial spectral index for the neutron spectrum, testifying to the capabilities of the method. Our main result is that, in all three cases and both with and without statistical weights, models with enhanced density in either the entire photosphere (model 5) or in subphotospheric layers (models 2 and 3) provided the best fit to the 2.223-MeV gamma-ray observations.

Flare of December 16, 1988. The entire set of programs for the computations and the analysis method were appreciably improved in 2002. Most importantly, the method used to take into account the form of the initial neutron spectrum was changed. We accordingly turned to the computed neutron spectra obtained in [7] under the assumption that the energy spectrum of the initial accelerated particles could be represented by a modified second-order Bessel function, K_2 (see, for example, [41]):

$$dN/dE \propto \beta K_2[2(3\beta/\alpha T)^{1/2}, \qquad (7)$$

where E is the energy of a particle with velocity v per nucleon, dN/dE is the differential intensity in units of particles/cm^2 s sr (MeV/nucleon), and $\beta = v/c$. The dimensionless parameter αT characterizes the shape of the energy spectrum of the charged particles under the assumption that they are stochastically accelerated with efficiency α (the acceleration rate) and that the time that they are contained in the acceleration volume is T.

Based on the results of [7], we considered two limiting cases for the angular distribution of the injected neutrons (isotropic and directed vertically downward). The computational results for the various spectra (i.e., various values of αT) and the five density models were then applied to the large flare of December 16, 1988 [39].

The class X4.7/2B flare of December 16, 1988 occurred at a heliocentric angle of 43° in the active region AR5278 (N27, E33). The SMM gamma-ray

Table 4. Comparison of observational and computational data for two flares [28]

s	m	November 6, 1997		March 22, 1991	
		Σ, 10^4	Σ_w	Σ, 10^6	Σ_w
0	1	10.88	78.7	9.882	21.74
	2	6.37	15.3	4.660	0.9182
	3	–	–	2.716	*
	4	6.60	15.5	*	4.621
	5	8.55	23.6	11.72	14.72
				55.33	6.870
1	1	5.98	12.8	64.72	119.0
	2	6.14	13.2	55.23	54.70
	3	–	–	57.41	79.70
	4	5.93	9.5	87.37	113.6
	5	3.95*	11.8	31.75	4.489
2	1	6.07	10.8	413.6	664.9
	2	5.65	10.4	441.8	605.5
	3	–	–	371.2	561.0
	4	5.23	7.5	593.6	753.4
	5	6.13	16.2	692.8	10.49
3	1	5.84	10.5	699.6	1244
	2	5.58	10.3	716.7	1173
	3	–	–	617.6	1076
	4	5.30	7.4	1126	1984
	5	4.81	6.8*	68.28	10.69

Note: The asterisks mark cases for which the agreement between the observational and computed decay constants is best.

Table 5. Plasma-density models and spectral indices for two flares [28]

Flare	Injection of neutrons	Without weights (Σ)		With weights (Σ_w)	
		s	m	s	m
March 22, 1991	Vertical	1	2	3	5
	Isotropic	0	3	0	2
November 6, 1997	Isotropic	1	5	3	5

spectrometer began to record the flare at 08:28:50 UT [42]. The time profile of the gamma-ray emission at 2.223 MeV had four peaks [43, 44]. Figure 4 presents the best approximation to the observed time profile of the 2.223 MeV line for the third (largest) peak (08:54:46–09:01:03 UT). In the corresponding model, the characteristic spectral parameter for the accelerated particles is $\alpha T = 0.03$ and the model density has $m = 5$, with an enhanced density throughout the photosphere. Figure 4 also shows the remaining four approximations.

The best fits for various cases are presented in Table 6 (in the column "All"). To study the possible evolution of αT during the acceleration phase of the flare, we carried out computations for three segments of the time profile for the 2.223 MeV gamma-ray emission, for all values of αT and all models, for the total time covered by the third peak and for three subintervals within this time. The best-fit approximation was determined using a least-squares criterion.

Figure 5 illustrates the best fits for two time intervals in the decay phase: $\alpha T = 0.005$ in the first interval (just after the flare maximum) and $\alpha T = 0.1$ in the second interval (both with density model 5).

It is interesting that, in the growth phase of the time profile (in the interval 24–136 s in Table 6), even the smallest sums of the squared residuals do not enable us to confidently identify an optimal density model (m) that could be unambiguously compared with a specific value of αT. Nevertheless, we can be sure that the growth phase is not fit by model 5, and that values of αT from 0.03 to 0.1 are more likely than the value 0.005. Thus, we conclude that there was no significant density enhancement in the photosphere in the initial phase of the third gamma-ray peak of the flare of December 16, 1988, but such an enhancement appeared approximately 140 s after the onset of the growth phase in the 2.223 MeV line. Table 7 summarizes the computational results for the 2.223 MeV line for all three large flares. We can see that we are not only able to add information about the main parameters of the neutron spectrum and the 2.223 MeV line to our overall picture of the flare, but also to analyze the dynamics of particle acceleration and the generation of gamma-ray emission on the Sun.

4. DISCUSSION AND CONCLUSION

First and foremost, the results presented above for the flares of December 16, 1988, March 22, 1991, and November 6, 1997 demonstrate the effectiveness of our method in determining the most probable density profile with height in the solar atmosphere based on observations of the 2.223 MeV gamma-ray line. The main result for all three cases considered is that the

plasma density in the photosphere above the flare region was enhanced compared to the corresponding density for the standard model of the unperturbed atmosphere. Moreover, in the flare of December 16, 1988, we infer a delay in the appearance of this density enhancement relative to the onset of the gamma-ray event. In addition, we are able to relate the time profile of the 2.223 MeV gamma-ray line to the initial spectrum of the charged particles and other characteristics of the acceleration process. This opens new and interesting possibilities for studies of particle acceleration on the Sun based on data for gamma-ray flares. In particular, our approach has enabled us to detect a tendency for the spectrum of accelerated particles to harden in the decay phase of the December 16, 1988 flare. This is consistent with results obtained earlier using other methods for this same flare [43, 44] and for the flares of April 24, 1984 and October 19, 1989 [44].

We emphasize that our method has enabled us for the first time to derive simultaneously the most probable vertical density profile for the solar plasma and the parameter αT for the spectrum of accelerated protons. This made it possible to trace the dynamics of both of these characteristics over the time covered by the gamma-ray flares. This is clearly visible in our results for the third peak of the gamma-ray flare of December 16, 1988.

(1) We detected a density enhancement throughout the photosphere, to values $\sim 10^{17}$ cm^{-3}. In contrast, the density in the quiescent photosphere grows smoothly from 10^{16} cm^{-3} at the top of the photosphere to 10^{17} cm^{-3} $\sim$ 350 km below this level.

(2) This density enhancement is not present during the growth phase of the gamma-ray emission, and

Table 6. Rms deviations of the computational results of [39] from the observational data for various time intervals during the December 16, 1988 flare

αT	m	All	24–136 s	136–264 s	280–408 s
0.005	1	2.0×10^2	4.0	38	3.1
	2	1.9×10^2	2.2	37	3.3
	3	2.0×10^2	2.1	42	3.2
	4	2.1×10^2	3.6	39	3.7
	5	8.8	3.0	3.3	1.1
0.03	1	68	1.5	15	1.8
	2	53	1.6	10	2.1
	3	64	1.4	14	2.0
	4	70	1.5	13	2.3
	5	8.5	3.1	3.7	0.40
0.01	1	52	1.4	11	1.6
	2	37	2.0	7.4	7.4
	3	47	1.6	10	1.8
	4	52	1.4	10	2.1
	4	9.0	3.1	3.1	0.34

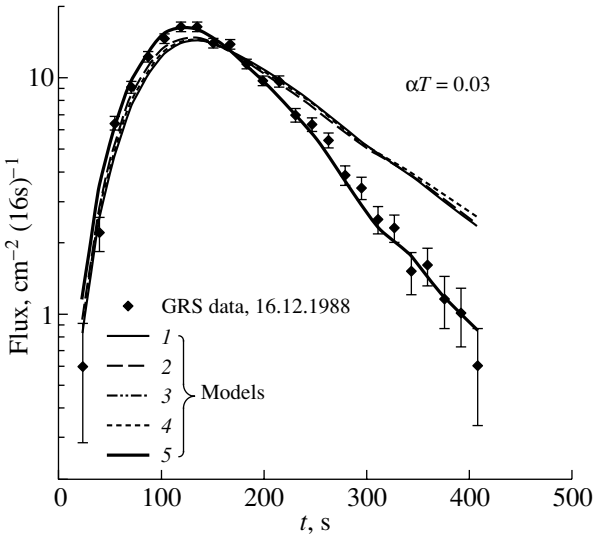

Fig. 4. Observed time profile of 2.223 MeV gamma-ray emission (diamonds) for the flare of December 16, 1988 [42] and the best approximation ($\alpha T = 0.03$, model 5; bold, solid curve) based on the entire time covered by the third peak in the gamma-ray flare [39]. The curves for models 1–4 are also presented. The initial time (08:26:23 UT) corresponds to 1704 s after the onset of the flare.

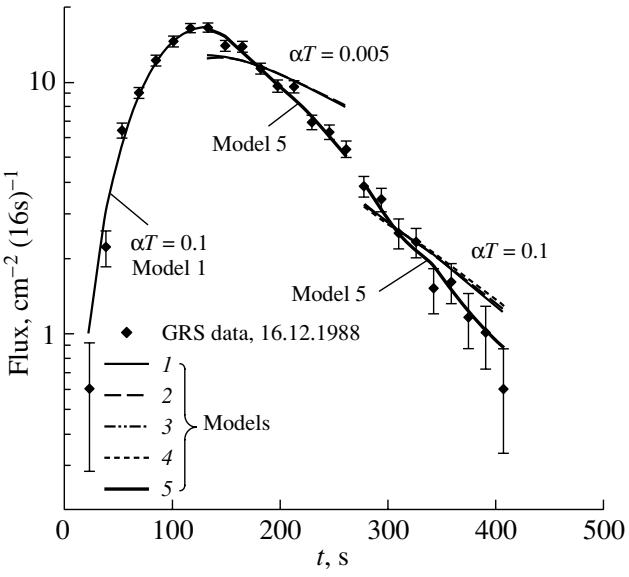

Fig. 5. Observed time profile of the 2.223 MeV line (diamonds) during the flare of December 16, 1988 [42] and the best-fit approximation [39] for the growth phase ($\alpha T = 0.1$, model 1; thin, solid curve) and in two segments of the decay phase ($\alpha T = 0.005$, model 5 and $\alpha T = 0.1$, model 5; bold solid curves).

Table 7. Plasma-density model and spectral indices for the three flares

Time of the flare	Coordinates, class (optical/X-ray)	Instrument, spacecraft, reference	Assumed distribution for emitted neutrons		Results			
			Time profile $I(t)$	Direction	Without weights		With weights	
Comparison method: comparing time profiles of decay constants								
Result: index of initial power-law neutron spectrum s and density model number m								
March 22, 1991 22:42:51 UT	S26, E28 3B/X9.4	PHEBUS, GRANAT [40]	instantaneous injection	vertical	$s = 1$	$m = 2$	$s = 3$	$m = 5$
				isotropic	$s = 0$	$m = 3$	$s = 0$	$m = 2$
November 6, 1997 11:52 UT	S18, W64 2B/X9.4	Gamma-ray spectrometer, Yohkoh [38]	$I(t)$ taken into account	isotropic	$s = 1$	$m = 5$	$s = 3$	$m = 5$
Comparison method: comparing time profiles								
Result: spectral index αT of charged particles and density model number m								
December 16, 1988 08:26 UT	N27, E23 1B/X4.7	GRS, SMM [42]	$I(t)$ taken into account	isotropic	$\alpha T = 0.03^*$	$m = 5^{**}$	–	–

* We also inferred a hardening of the proton spectrum in the decay phase of the gamma-ray flare: the index αT grows with time from 0.005 to 0.1.

** The appearance of the enhancement of the photospheric density (model 5) lags behind the onset of the gamma-ray flare by a time of the order of the duration of the growth phase (140 s).

arises during the decay phase, roughly 140 s after the onset of the flare.

(3) Assuming that the acceleration is stochastic, the proton-spectrum parameter αT is equal to 0.03 averaged over the entire time for the flare.

(4) In the decay phase of the gamma-ray emission, αT grows from 0.005 to 0.1; i.e., the spectrum hardens with time.

(5) The proton spectrum in the growth phase of the gamma-ray emission is harder than at the onset of the decay phase (αT is in the range 0.03–0.1).

The possibility that the spectrum of the accelerated particles varies during the course of a flare has been discussed in a number of earlier studies [36, 43–45], in connection with the possible realization of two or more acceleration mechanisms during the flare. In particular, this idea was put forth in [43] as an explanation of the properties of the gamma-ray emission of the December 16, 1988 flare. During the flare of June 11, 1991, for example, at least three separate episodes of gamma-ray injection were identified [43], based on the variations of the ion spectrum in the transitions between episodes [45].

Numerous attempts to use data on the 2.223 MeV gamma-ray line to derive new information about the properties of the gamma-ray source have now been undertaken. However, to bring about progress in this area, it is necessary to decrease the uncertainties associated with the most important factors influencing the formation of this line, in particular, the ^{3}He content and the contribution of dynamical deviations of the density from the density for the standard model. A third important characteristic is the accelerated-particle spectrum. The ^{3}He content and either the density model or the spectral index can be used to derive two of the free parameters. At the same time, the ability to use all three parameters is unlikely with current methods. This means that we require additional information about the ^{3}He, density variations in the photosphere, parameters of the accelerated-particle spectrum, and other associated parameters.

Thus, future perspectives for the method involve applying it to new data on gamma-ray flares for which data with high energy, time, and angular resolution have recently been obtained by instruments on the RHESSI (July 23, 2002 and October–November 2003), Integral, and CORONAS-F (October–November 2003) spacecraft. Data on other gamma-ray lines, such as those at 4–7 MeV, should also be used. It will also be useful to obtain independent measurements of the ^{3}He content, either using new methods of solar gamma-ray spectroscopy (see, for example, [46]) or by measuring the weak line at 20.58 MeV, due to the radiative capture of neutrons by ^{3}He nuclei in solar flares [47]. This last possibility was first suggested and discussed in [4]. Other possibilities for developing the method

include considering a power-law proton spectrum, as is formed during shock acceleration, and allowing for some distribution of the initial neutrons with depth.

ACKNOWLEDGMENTS

This work was partially supported by the Russian Foundation for Basic Research (project nos. 01-02-17994, 02-02-39032, 03-02-96026), the Federal Program in Science and Technology "Astronomy" (Section I, project 4), and a Grant of the President of the Russian Federation (project no. SS-1145.2003.2). The authors thank G.H. Share and R.J. Murphy (Naval Research Laboratory, USA), and also M.A. Lifshits (IZMIRAN) for stimulating discussions about a number of questions that are touched upon in this paper.

REFERENCES

1. E. L. Chupp, D. J. Forrest, P. R. Higbie, *et al.*, Nature **241**, 333 (1973).
2. E. L. Chupp, D. J. Forrest, J. M. Ryan, *et al.*, Astrophys. J. **263**, L95 (1982).
3. R. Ramaty, B. Kozlovsky, and R. E. Lingenfelter, Space Sci. Rev. **18**, 341 (1975).
4. B. M. Kuzhevskij, Usp. Fiz. Nauk **137**, 237 (1982) [Sov. Phys. Usp. **25**, 392 (1982)].
5. V. I. Abramov and Yu. D. Kotov, Pis'ma Astron. Zh. **13**, 142 (1987) [Sov. Astron. Lett. **13**, 58 (1987)].
6. R. J. Murphy and R. Ramaty, Adv. Space Res. **4** (7), 127 (1984).
7. X.-M. Hua and R. E. Lingenfelter, Astrophys. J. **323**, 779 (1987).
8. R. Ramaty and R. J. Murphy, Space Sci. Rev. **45**, 213 (1987).
9. X.-M. Hua and R. E. Lingenfelter, Astrophys. J. **319**, 555 (1987).
10. R. J. Murphy, R. Ramaty, B. Kozlovsky, and D. V. Reames, Astrophys. J. **371**, 793 (1991).
11. B. V. Somov, A. R. Spektor, and S. I. Syrovatskii, Tr. Fiz. Inst. im. P.N. Lebedeva, Ross. Akad. Nauk **110**, 73 (1979).
12. E. A. Baranovskii, in *Investigations of Solar Plasma*, Ed. by B. V. Somov (Ylym, Ashkhabad, 1989), p. 228 [in Russian].
13. W. Q. Gan, C. Fang, and H. Q. Zhang, Astron. Astrophys. **241**, 618 (1991).
14. A. Ya. Boiko and M. A. Livshits, Astron. Zh. **72**, 381 (1995) [Astron. Rep. **39**, 338 (1995)].
15. A. N. Babin and A. N. Koval', Kinematika Fiz. Nebesnykh Tel **15**, 51 (1999).
16. V. N. Ishkov, Izv. Ross. Akad. Nauk, Ser. Fiz. **62**, 1835 (1998).
17. R. E. Lingenfelter, Sol. Phys. **8**, 341 (1969).
18. H. T. Wang and R. Ramaty, Sol. Phys. **36**, 129 (1974).
19. B. M. Kuzhevskij and E. V. Troitskaia, Preprint No. 89-28/105, NIIYaF MGU (Inst. of Nuclear Phys., Moscow State Univ., Moscow, 1989).
20. B. M. Kuzhevskij and E. I. Kogan-Laskina, Astron. Zh. **67**, 1022 (1990) [Sov. Astron. **34**, 514 (1990)].
21. B. M. Kuzhevskij, E. I. Kogan-Laskina, and E. V. Troitskaia, Vestn. Mosk. Univ., Ser. 3: Fiz., Astron. **32**, 60 (1991).
22. B. M. Kuzhevskij, S. N. Kuznetsov, and E. V. Troitskaia, Izv. Ross. Akad. Nauk, Ser. Fiz. **60** (8), 196 (1996).
23. B. M. Kuzhevskij, S. N. Kuznetsov, and E. V. Troitskaia, Adv. Space Res. **22**, 1141 (1998).
24. O. Gingerich, R. W. Noyes, W. Kalkofen, and Y. Cuny, Sol. Phys. **18**, 347 (1971).
25. H. C. Spruit, Sol. Phys. **34**, 277 (1974).
26. B. M. Kuzhevskij and E. V. Troitskaia, Izv. Ross. Akad. Nauk, Ser. Fiz. **65**, 330 (2001).
27. B. M. Kuzhevskij, L. I. Miroshnichenko, and E. V. Troitskaia, in *Proceedings of 27th International Cosmic Ray Conference* (2001), p. 285.
28. B. M. Kuzhevskij, L. I. Miroshnichenko, and E. V. Troitskaia, Izv. Ross. Akad. Nauk, Ser. Fiz. **66**, 1673 (2002).
29. W. N. Johnson, R. L. Kinzer, J. D. Kurfess, *et al.*, Astrophys. J., Suppl. Ser. **86**, 693 (1993).
30. D. J. Forrest, E. L. Chupp, J. M. Ryan, *et al.*, Sol. Phys. **65**, 15 (1980).
31. A. V. Dmitriev, M. A. Kovalevskaya, S. N. Kuznetsov, *et al.*, in *Proceedings of 23rd International Cosmic Ray Conference* (1993), Vol. 3, p. 175.
32. R. J. Murphy, G. H. Share, and M. Yoshimori, in *High Energy Solar Physics Workshop—Anticipating HESSI,* Ed. by R. Ramaty and N. Mandzhavidze, Astron. Soc. Pac. Conf. Ser. **206**, 387 (2000).
33. G. E. Kocharov, in *Proceedings of VI Leningrad Seminar on Cosmophysics* (Fiz.-Tekh. Inst., Leningrad, 1974), p. 9.
34. R. Ramaty and R. E. Lingenfelter, in *Proceedings of VI Leningrad Seminar on Cosmophysics* (Fiz.-Tekh. Inst., Leningrad, 1974), p. 25.
35. T. A. Prince, D. J. Forrest, E. L. Chupp, *et al.*, in *Proceedings of 18th International Cosmic Ray Conference* (1983), Vol. 4, p. 79.
36. R. J. Murphy, C. D. Dermer, and R. Ramaty, Astrophys. J., Suppl. Ser. **63**, 721 (1987).
37. G. Trottet, N. Vilmer, C. Barat, *et al.*, Astron. Astrophys., Suppl. Ser. **97**, 337 (1993).
38. M. Yoshimori, A. Shiozawa, and K. Suga, in *Proceedings of 26th International Cosmic Ray Conference* (1999), Vol. 6, p. 5.
39. E. V. Troitskaia, W. Gan, B. M. Kuzhevskij, and L. I. Miroshnichenko, in *Proceedings of 28th International Cosmic Ray Conference* (2003), Vol. 6, p. 3219.
40. O. V. Terekhov, A. G. Kuz'min, R. A. Syunyaev, *et al.*, Pis'ma Astron. Zh. **22**, 163 (1996) [Astron. Lett. **22**, 143 (1996)].
41. R. Ramaty, in *Particle Acceleration Mechanisms in Astrophysics*, Ed. by J. Arons, C. Max, and C. McKee (Am. Inst. Phys., New York, 1979), Vol. 56, p. 135.

42. W. T. Vestrand, G. H. Share, R. J. Murphy, *et al.*, Astrophys. J., Suppl. Ser. **120** (2), 409 (1999).
43. E. Rieger, in *High Energy Solar Physics*, Ed. by R. Ramaty, N. Mandzhavidze, and X.-M. Xua (Am. Inst. Phys., New York, 1996); AIP Conf. Proc. **374**, 194 (1996).
44. W. Q. Gan, Astrophys. J. **496**, 992 (1998).
45. N. Mandzhavidze, R. Ramaty, D. Bertsch, and E. J. Schneid, in *High Energy Solar Physics*, Ed. by R. Ramaty, N. Mandzhavidze, and X.-M. Xua (Amer. Inst. Phys., New York, 1996); AIP Conf. Proc. **374**, 225 (1996).
46. G. H. Share and R. J. Murphy, in *High Energy Solar Physics: Anticipating HESSI*; Astron. Soc. Pac. Conf. Ser. **206**, 377 (2000).
47. V. P. Alfimenkov, S. B. Borzakov, Ya. Vezhbitski, *et al.*, Pis'ma Zh. Éksp. Teor. Fiz. **29**, 100 (1979) [JETP Lett. **29**, 91 (1979)].

Translated by D. Gabuzda

Astronomy Reports, Vol. 49, No. 7, 2005, pp. 579–586. Translated from Astronomicheskiĭ Zhurnal, Vol. 82, No. 7, 2005, pp. 649–656.

Quasi-Periodicity of MgXII X-ray Bursts Revealed by CORONAS-F SPIRIT Data for Solar Active Regions

L. A. Akimov[1], S. A. Beletskiĭ[1], I. L. Belkina[1], O. I. Bugaenko[2], Yu. I. Velikodskiĭ[1], I. A. Zhitnik[3], A. P. Ignat'ev[3], V. V. Korokhin[1], S. V. Kuzin[3], G. P. Marchenko[1], and A. A. Pertsov[3]

[1] *Scientific-Research Institute, Kharkov University, Kharkov, 310022 Ukraine*

[2] *Sternberg Astronomical Institute, Universitetskiĭ pr. 13, Moscow, 119899 Russia*

[3] *Lebedev Physics Institute, Leninskiĭ pr. 53, Moscow, 117924 Russia*

Received July 30, 2004; in final form, February 17, 2005

Abstract—A spectral analysis of a series of integrated MgXII 8.42 Å X-ray intensities recorded by the CORONAS-F SPIRIT spectroheliometer is presented. Statistically significant peaks for periods in the intervals 12–30 min and 40–200 min were found in the power spectra. The power spectrum for these periods changed after the emergence of new photospheric magnetic flux in the active region NOAA 9840.

1. INTRODUCTION

Intensive studies of the solar activity in the last several decades provide evidence for a variety of coronal oscillatory processes that display emission at almost all wavelengths—radio, optical, ultraviolet, and X-ray, up to the shortest observed [1]. The periods of these oscillations vary over a wide range, from tenths or hundredths of a second to several thousand seconds. Various physical mechanisms, most of which correspond to oscillatory MHD modes of coronal loops, have been invoked to explain these phenomena.

Comparatively short-period (several minutes) eigenmodes of loops (magnetic tubes) have been studied in detail theoretically. Formulas relating the oscillation periods to the lengths and magnetic fields of the loops and the plasma temperatures and densities inside the loops have been obtained for most regimes (see, for example, [2]). These periods can be used as diagnostics of the physical conditions in coronal loops, demonstrating the importance of such studies.

Observational data on oscillatory processes on the Sun have been obtained using various instruments, such as the Yohkoh SXT telescope [3], TRACE [4], and SOHO SUMER spectrograph [5, 6]. In the last two studies, oscillations with quasi-periods of 12–31 min and exponential damping on approximately the same time scale were observed only in high-temperature lines ($T > 6$ MK). The authors argued that these oscillations correspond to slow modes of standing waves that are impulsively excited in coronal loops by small flarelike phenomena.

Comparatively long-period (tens of minutes) oscillations were detected in the local radio sources of active regions by the Nobeyama radio telescope [7].

The purpose of our present study is to search for quasi-periodicity in MgXII 8.42 Å X-ray bursts occurring in individual solar active regions. The measurements used were obtained with the CORONAS-F SPIRIT Bragg MgXII spectroheliometer [8]. The solar images obtained in the MgXII 8.42 Å line indicate hot plasmas ($T_e > 5 \times 10^6$ K) in coronal structures [9]. One feature of the CORONAS-F orbit is that there are time intervals lasting up to twenty days and repeated every three months when the spacecraft is not shadowed by the Earth. During these intervals, solar X-ray images can be detected continuously with high time resolution.

The previous GOES-8 and GOES-10 studies of the periodicity of solar X-ray emission at similar wavelengths were carried out using a broad spectral band, and were relevant for the Sun as a star or for individual solar flares [10].

2. OBSERVATIONS AND PHOTOMETRIC DATA PROCESSING

We used the data obtained in the MgXII channel of the SPIRIT spectroheliograph from February 19–23,

1063-7729/05/4907-0579$26.00

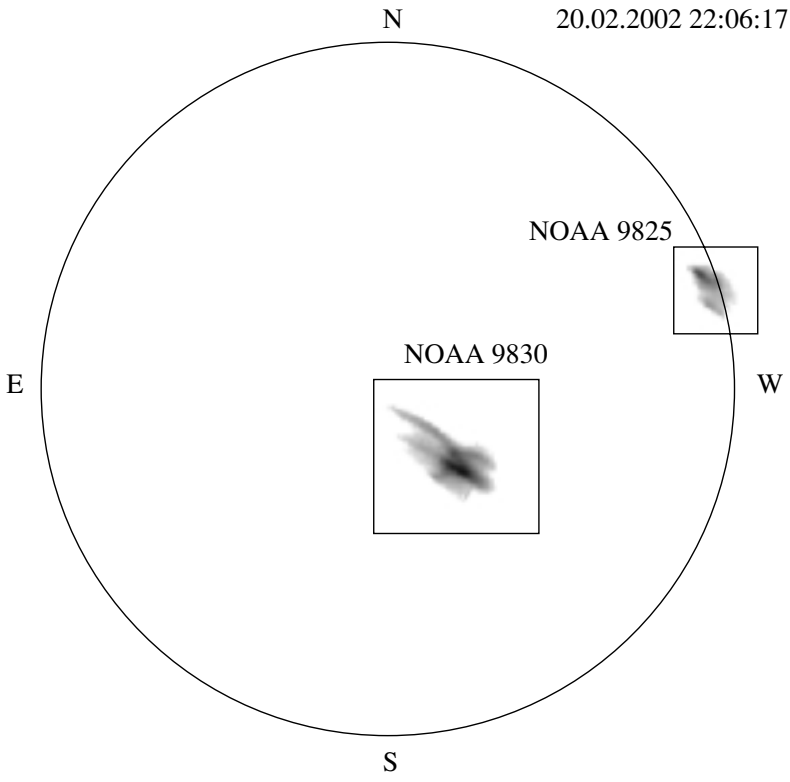

Fig. 1. Solar image in the MgXII 8.42 Å line obtained on February 20, 2002. The circle shows the location of the solar limb.

2002, when CORONAS-F was outside the shadow of the Earth. Solar images in the MgXII line were recorded every 1.75 min during this interval (every 0.6 min during some subintervals), to enable the analysis of rapid processes in high-temperature regions of the solar atmosphere. Figure 1 presents one of the images obtained in February 2002.

We selected five active regions for our study: NOAA 9825, 9830, 9835, 9837, and 9840. Other solar high-temperature formations observed during this time interval were short lived and not suitable for studies of periodic intensity variations. Active regions 9825 and 9830 were developed sunspot groups with complex $\beta\gamma$ and $\beta\gamma\delta$ magnetic configurations, respectively, in which a large number of Hα and X-ray flares were observed (Solar Geophysical Data). Active region 9835 displayed a β configuration, while 9830 evolved from a single sunspot to a β configuration. Active region 9840 was detected at the photospheric level at $09^{h}\ 25^{m}$ on February 21 (Solar Geophysical Data). Hot coronal plasma above the active region was observed in the MgXII 8.42 Å line starting from February 19. The brightness and area of 9840 increased considerably after the emergence of sunspots.

The photometric processing of the images included cleaning from cosmic-ray traces and occasional transmitter–receiver noise, removing nonuniformity in the background, and determining the integrated radiation flux of each active region as the difference between the fluxes in a rectangular area containing the entire active region and a background area of the same size located near the active region.

We processed 3530 images. The temporal profiles determined for each active region were interpolated for a uniform grid with a time step of 1.748 min. For active regions 9830, 9837, and 9840, the time series span was approximately 89 h (3044 points). The series for 9825 and 9835 were somewhat shorter, since these regions were located near the western limb and their heliocentric longitudes for February 23 were $>90°$.

Logarithmic radiation fluxes of each active region were used to search for periodicity, since the dynamic range of the X-ray bursts covers several orders of magnitude.

Figure 2 presents the time evolution of the integrated logarithmic radiation fluxes for the active regions. We can see that the variations of the integrated fluxes of the active regions are predominantly

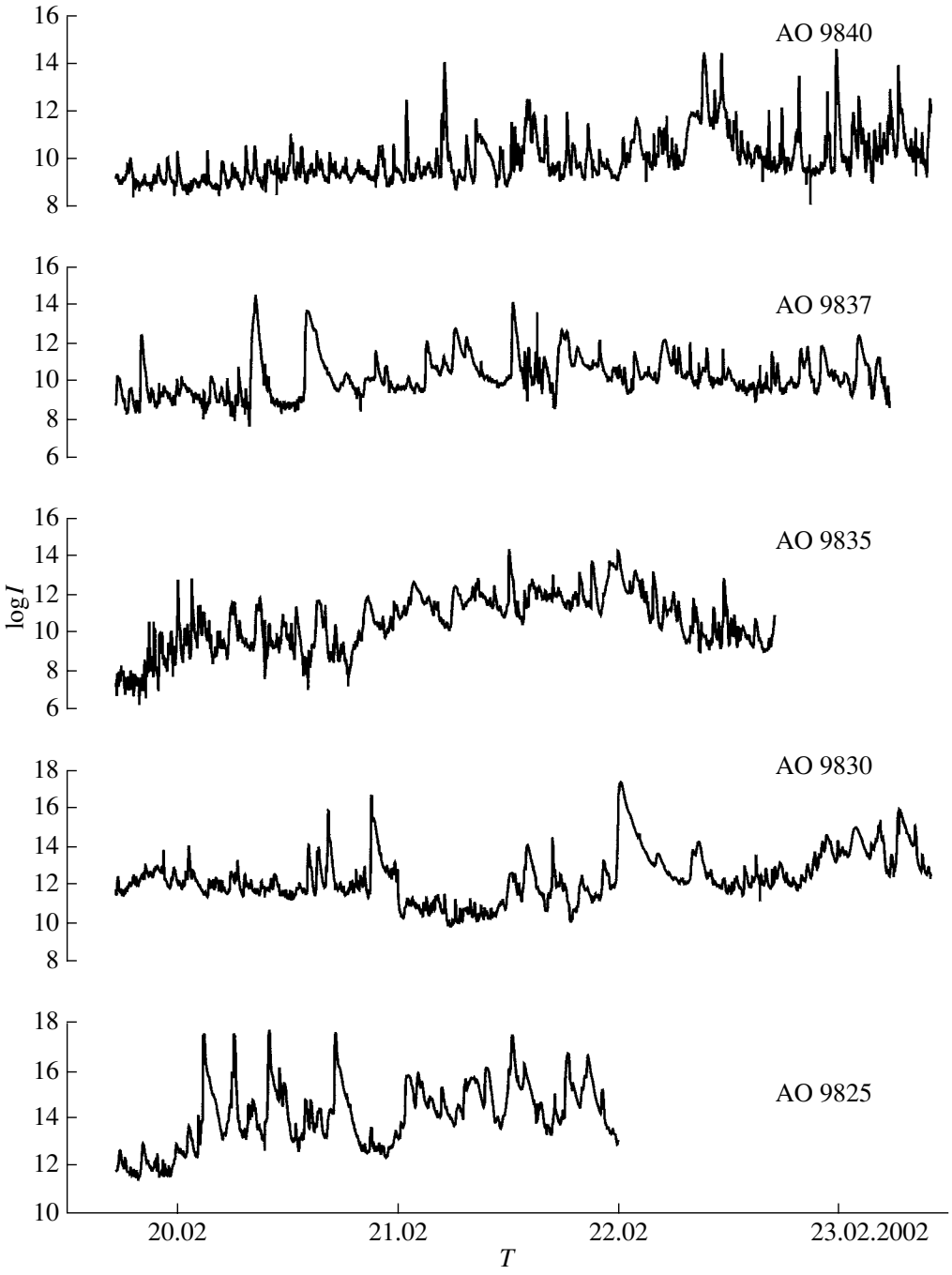

Fig. 2. Time evolution of the integrated radiation fluxes of the active regions for February 19–23, 2002. Intensities are shown on a logarithmic scale.

random but also contain regular components. The quasi-period of these variations can change even for a single active region; for example, the February 19–21 variations for active region 9840 differ appreciably from those for February 22–23.

Figure 3 compares the data we used with the time series obtained for the integrated GOES-10 X-ray flux at 1–8 Å. The upper curve shows the variations in the total SPIRIT MgXII 8.42 Å flux associated with the active regions on February 20, while the lower curve shows the GOES-10 data for the integrated

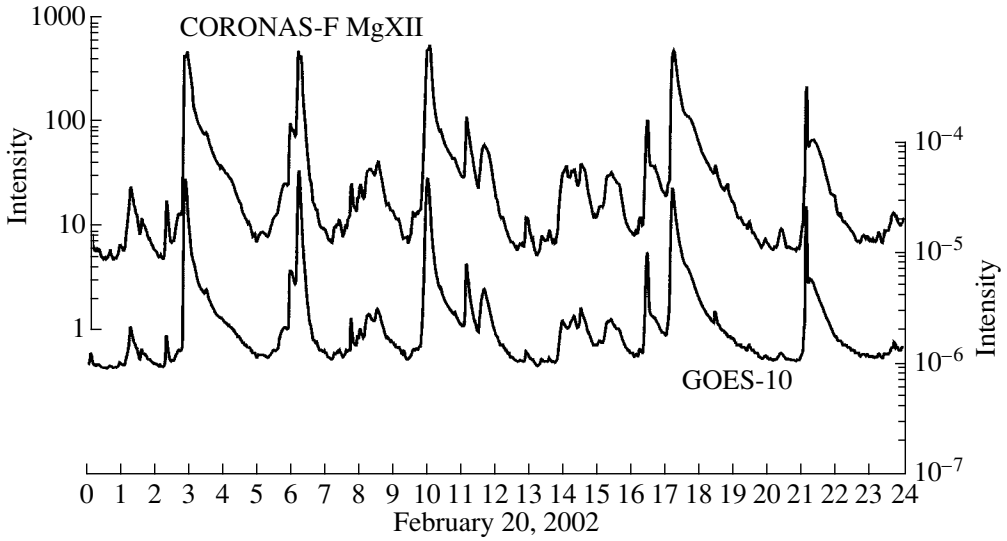

Fig. 3. Comparison of GOES-10 data at 1–8 Å with the variations of the total CORONAS-F MgXII 8.42 Å flux for all the active regions for February 20, 2002.

solar radiation at 1–8 Å. The small differences between these curves can be attributed to differences in the spectral responses of the SPIRIT and GOES instruments.

3. ANALYSIS OF THE QUASI-PERIODICITY OF BURSTS

To estimate the spectral power of the variations for the active regions studied, we performed a Fourier analysis of the autocorrelation functions of the logarithms of the integrated radiation fluxes. The autocorrelation functions were calculated using the formula

$$k(m) = \frac{1}{Ns^2} \sum_{n=1}^{N-m} [u(n) - s][u(n+m) - s],$$

where $u(n)$ is the logarithm of the integrated flux, s its mean value, and N the number of data points. This method for calculating the spectral density significantly reduces the effect of the sample size.

For small arguments, a typical autocorrelation function is similar to an exponential function, as is quite natural given a Poisson distribution for the times of the bursts, their random durations, and their jumplike growth. Consequently, the spectral power density at high frequencies should decrease as the inverse square of the frequency [10], as is observed overall. However, there are peaks related to processes occurring in each active region against the general decrease in the power with frequency. To identify statistically significant peaks at high frequencies, the spectra were averaged with a moving window. The data points were divided into intervals of 1027 points each (1795.2 min). The intervals were moved by half their width, and the power spectra obtained were averaged for all intervals. This window size enabled us to identify statistically significant peaks for periods of 4–40 min.

Figure 4 presents the averaged power spectra for periods of 4–30 min for all the active regions considered (the interval of 30–40 min does not contain statistically significant peaks). The horizontal axis plots not the frequencies, but the periods in order of their growth. We can see then that the power spectra for all the active regions contain peaks for quasi-periods of 12–30 min and no significant peaks for periods of 4–10 min. The powers of the peaks corresponding to these periods are approximately the same for different active regions, although the periods themselves do not completely coincide. For example, a significant peak for a quasi-period of 12.5 min is present in the spectrum for active region 9840 at the initial stage of its evolution, preceding the emergence of sunspots. This is shown in Fig. 5, which presents the averaged power spectra for 9840 before (19.74^{d}–21.25^{d}) and after (21.25^{d}–23.41^{d}) the emergence of sunspots on the photosphere.

At low frequencies (periods of 40–200 min), there are some maxima with amplitudes exceeding the average by factors of three to five (Fig. 6). Note that the low-frequency power spectra presented in Fig. 6 were obtained without averaging with a moving window.

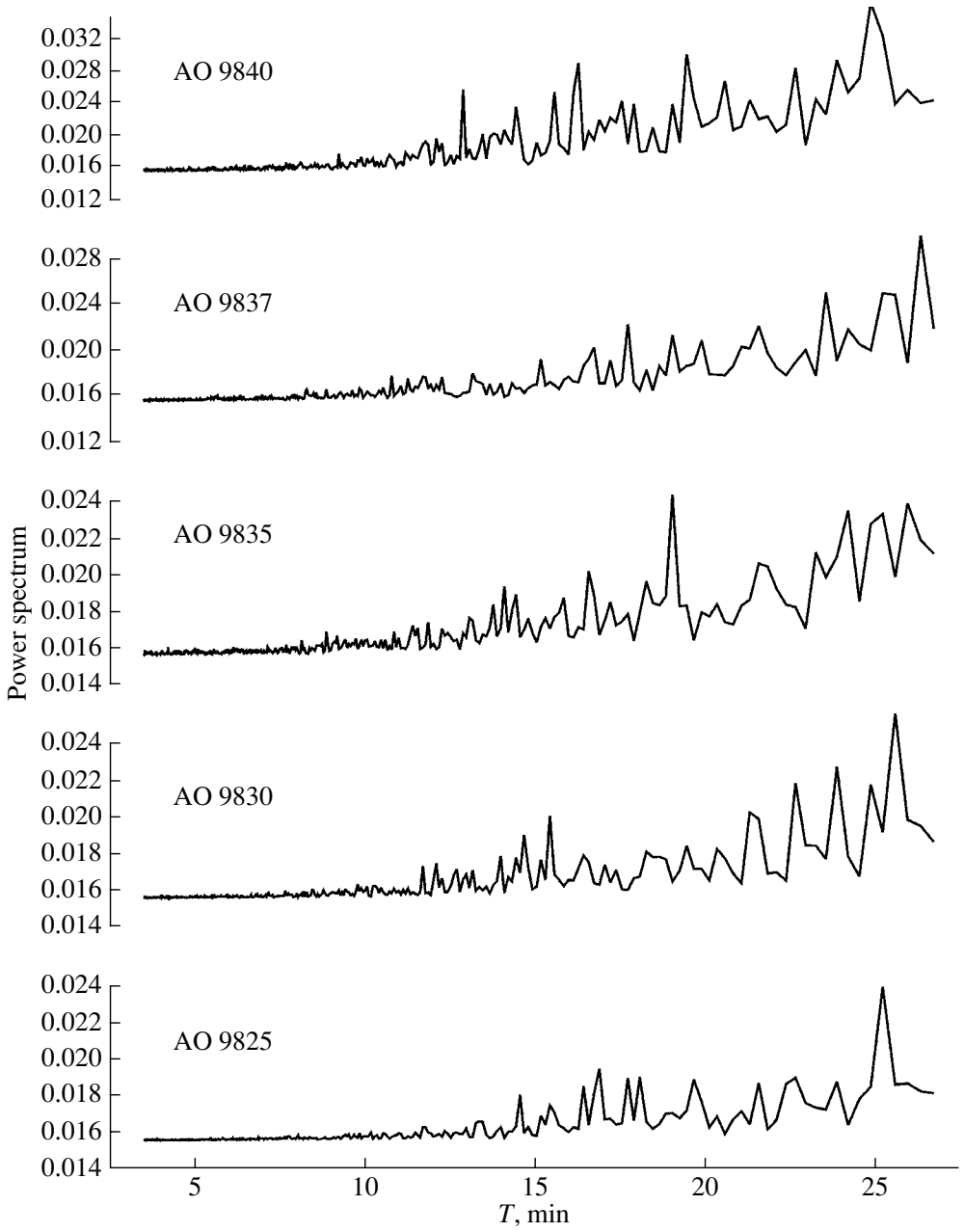

Fig. 4. Averaged power spectra for periods of 4–30 min observed in the active regions.

4. DISCUSSION

Our analysis of the variations of the integrated MgXII 8.42 Å X-ray fluxes for these five active regions indicates statistically significant quasi-periodic variations with periods of 12–30 min. It is probable that these variations correspond to periodic processes or waves in hot coronal loops. These periods may be associated with disturbances in the lower atmosphere or variations in the parameters of the coronal plasma, such as the densities, magnetic fields, and sizes of loops. Changes in the power spectrum of the active region after the emergence of sunspots suggest a connection between the quasi-periods and the physical parameters of coronal loops.

We find that the low-frequency peaks are different for different active regions. For example, the compact, evolving region 9840 displayed quasi-periods of 72 and 84 min (Fig. 6), while the flare active region 9825 had quasi-periods of about 138 and 160 min.

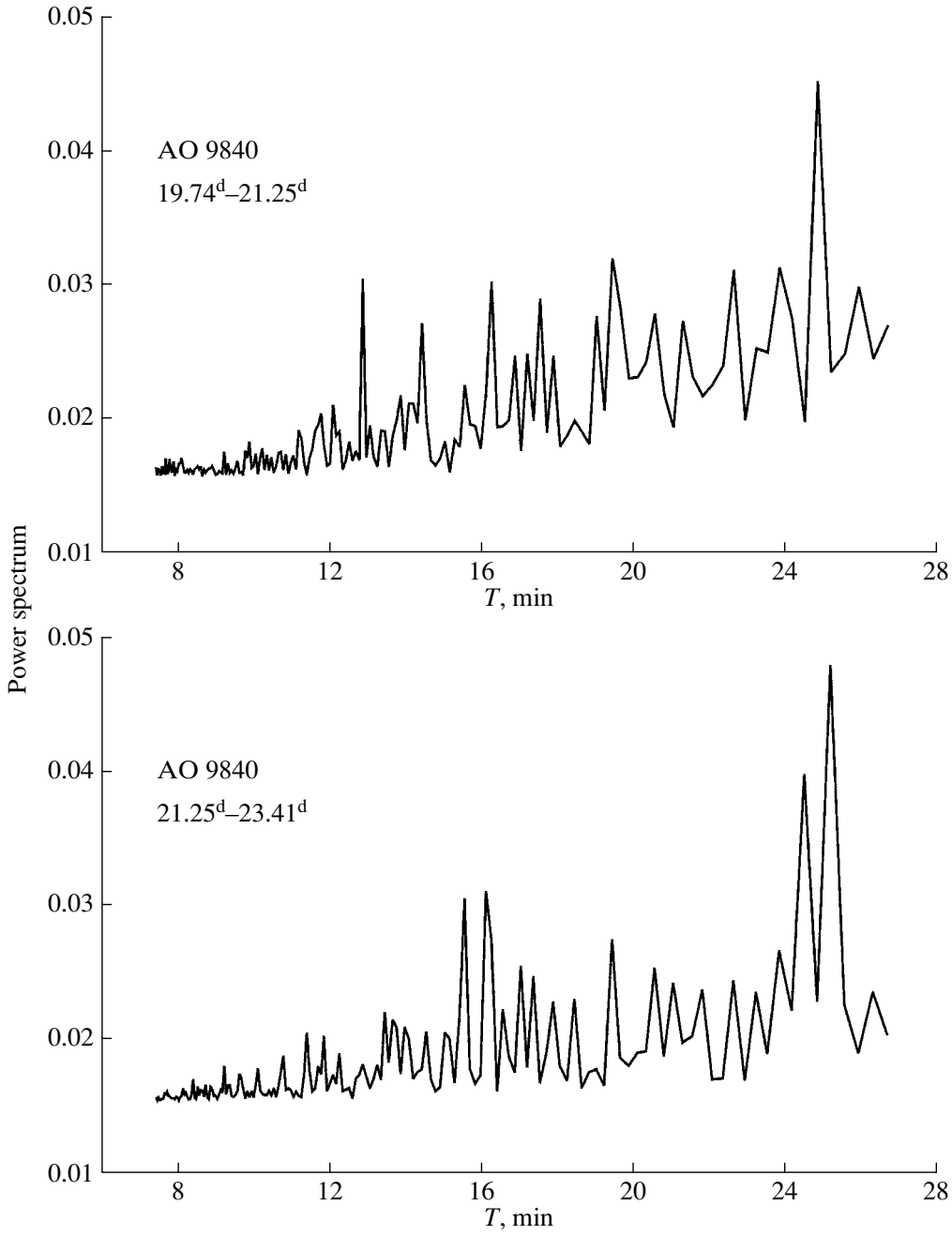

Fig. 5. Changes in the power spectrum related to the evolution of the sunspot group in the active region 9840.

Thus, differences in the low-frequency maxima due to the frequencies of large bursts in different active regions are probably associated with the structure and strength of magnetic fields in the active regions.

We did not detect any quasi-periodic changes in the integrated radiation fluxes that could correspond to 5-min oscillations. This can be explained by the fact that our analysis was applied to entire active regions containing numerous magnetic loops. This conclusion is supported in [11].

To obtain more definitive conclusions about the presence of 3–5 min oscillations in the radiation of high-temperature coronal loops observed at MgXII 8.42 Å, we plan to carry out detailed studies of individual structures in active regions using data with higher time resolution.

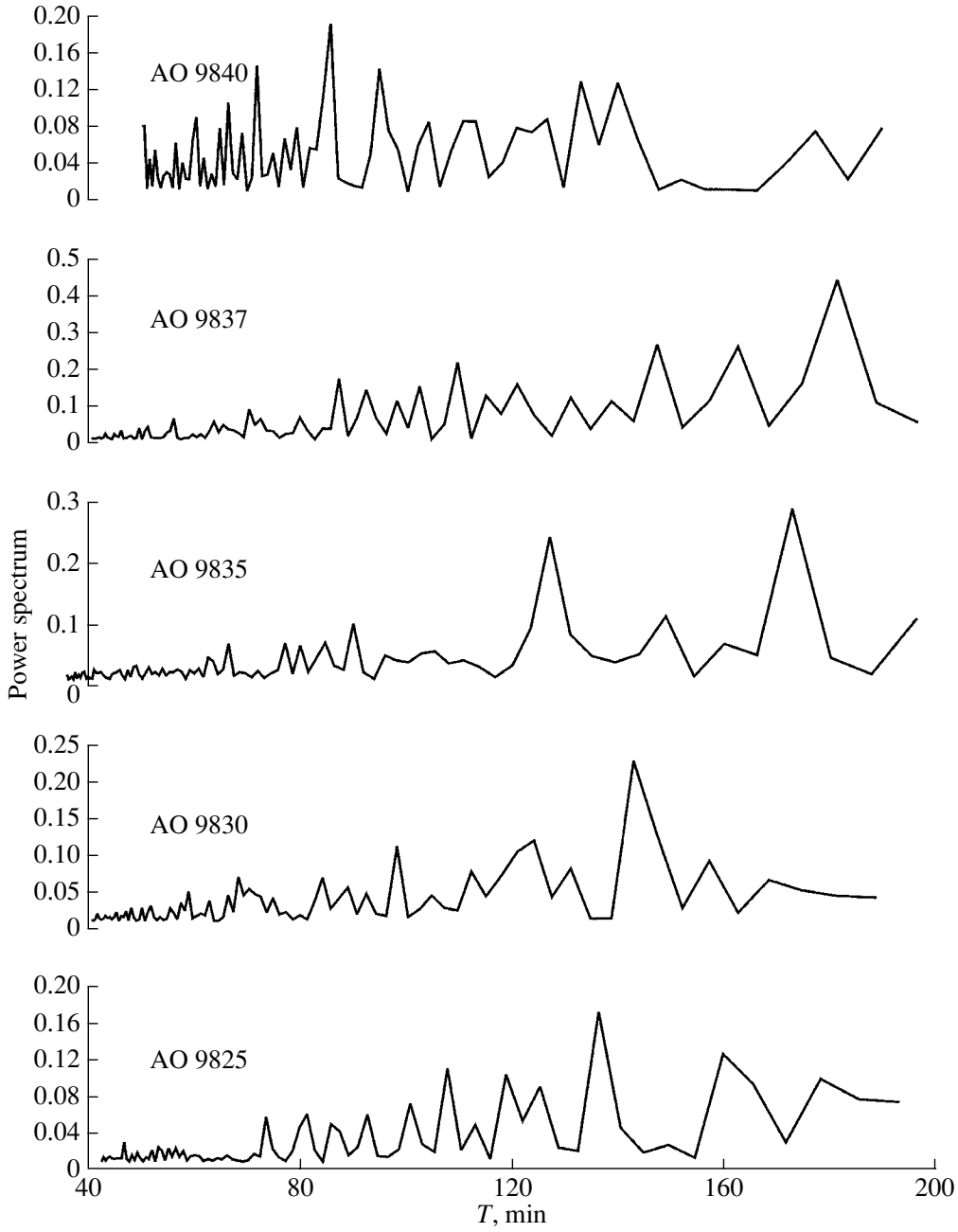

Fig. 6. Power spectra of active regions for periods of 40–200 min.

ACKNOWLEDGMENTS

The authors are grateful to V.V. Grechnev and S.A. Bogachev for fruitful discussions. This work was supported by the Russian Foundation for Basic Research (project no. 02-02-17272) and the program "Nonstationary Phenomena in Astronomy" of the Presidium of the Russian Academy of Sciences.

REFERENCES

1. M. J. Aschwanden, in *Turbulence, Waves, and Instabilities in the Solar Plasma, NATO Advanced Research Workshops, Budapest, Hungary, 2002* (2003).
2. B. Roberts, P. M. Edwin, and A. O. Benz, Astrophys. J. **279**, 857 (1984).

3. D. E. McKenzie and D. J. Mullan, Sol. Phys. **176**, 127 (1997).
4. M. J. Aschwanden, L. Fletcher, C. Schrijver, and D. Alexander, Astrophys. J. **520**, 880 (1999).
5. T. J. Wang, S. K. Solanki, W. Curdt, *et al.*, Astrophys. J. **574**, L101 (2002).
6. T. J. Wang, S. K. Solanki, W. Curdt, *et al.*, in *Magnetic Coupling of the Solar Atmosphere,* Ed. by H. Sawaya-Lacoste (ESA Publ. Division, Noordwijk, 2002), ESA SP-505, Vol. 188, p. 199.
7. G. B. Gel'freikh, Yu. A. Nagovitsin, and K. Shibasaki, in *The Sun in Epoch of Sign Changing* (St. Petersburg, 2001), p. 107.
8. V. N. Oraevskii and I. I. Sobel'man, Pis'ma Astron. Zh. **28**, 457 (2002) [Astron. Lett. **28**, 401 (2002)].
9. I. A. Zhitnik, O. I. Bugaenko, A. M. Urnov, *et al.*, Mon. Not. R. Astron. Soc. **338**, 67 (2003).
10. Yu. E. Charikov and P. B. Dmitriev, in *Modern Problems in the Physics of Solar and Stellar Activity* (Nizhni Novgorod, 2003), p. 292 [in Russian].
11. A. Nindos, C. E. Alissandrakis, G. B. Gelfreikh, *et al.*, Astron. Astrophys. **386**, 658 (2002).

Translated by V. Badin